

Contents

1 Thesis organization	1
I Theory introduction	3
2 Theoretical introduction	5
2.1 Standard model	5
2.2 Theory of pp collisions	5
2.3 Proton structure	5
3 Methodology of the measurement	7
3.1 Cross-Section methodology	7
3.1.1 Fiducial phase-space definition	8
3.1.2 Extrapolation to the 13 TeV fiducial phase-space	8
3.1.3 Combination of W^+ and W^- cross-sections	9
3.2 Ratios calculation	9
3.3 Combination of electron and muon cross-section measurements	10
3.4 PDF fits	11
II Experimental setup	13
4 The Large Hadron Collider (LHC) and the ATLAS experiment.	15
4.1 The LHC and accelerator complex	15
4.2 The ATLAS experiment	17
4.2.1 Coordinates and kinematic variables	18
4.2.2 Inner detector	18
4.2.3 Calorimeters	19
4.2.4 Muon spectrometer	23
4.2.5 Trigger system	23
4.3 Luminosity measurement	24
5 Event reconstruction	27
5.1 Tracks and vertexes	27
5.2 Electron reconstruction and identification	28
5.2.1 Central electrons reconstruction	28
5.2.2 Forward electrons reconstruction	28
5.2.3 Electron identification	29
5.3 Muon reconstruction and identification	29
5.4 Missing transverse energy reconstruction	30
5.4.1 Standard missing transverse energy reconstruction	30
5.4.2 Reconstruction of missing transverse energy from hadronic recoil	31

6 Monte-Carlo simulation	35
6.1 ATLAS chain of Monte-Carlo production	35
6.2 Event generators	36
6.3 Simulation in Geant4	38
7 Frozen Showers	39
7.1 Introduction	40
7.2 Generation and use in simulation	45
7.2.1 Libraries tuning	45
7.3 Machine learning based bin finding procedure	47
7.3.1 Machine learning introduction	47
7.3.2 Model description	49
7.3.3 Interpretation of results	51
7.3.4 Reconstructed electron energy	53
7.3.5 Plans for the future	54
7.4 Validation of the new libraries	57
8 Data and Monte-Carlo samples	59
8.1 Data sample	59
8.2 Monte-Carlo samples	60
III The Measurement	61
9 Selection	63
9.1 Data quality cuts	63
9.2 Lepton quality cuts	64
9.3 Boson selection	65
9.4 Cut flow	65
10 Monte-Carlo corrections	67
10.1 Lepton efficiency corrections	67
10.1.1 Muon Trigger SF	69
10.2 Electron energy scale and resolution	71
10.3 Muon momentum correction	72
11 Hadronic recoil calibration	75
11.1 Introduction	75
11.2 Hadronic recoil resolution correction	78
11.2.1 Event activity correction	78
11.2.2 Resolution corrections using Z events	84
11.3 Hadronic recoil bias correction	87
11.3.1 Bias determination from M_T^W distribution	88
11.3.2 Bias determination using u_{\parallel} distribution	90
11.3.3 Systematic uncertainty estimation	91
11.4 Summary on hadronic recoil systematics	91

12 Background estimation	93
12.1 QCD background estimation	94
12.1.1 Template selection	95
12.1.2 Methodology of the template sample normalization	95
12.1.3 Systematic uncertainty from the multi-jet background estimation	97
12.2 Background-subtracted W and Z candidate events	99
13 Control distributions	101
14 Uncertainties in the cross-section measurement	111
14.1 Methods of uncertainties propagation	111
14.2 Experimental systematic uncertainties	112
14.2.1 Electron energy scale and resolution	112
14.2.2 Muon energy scale and resolution	112
14.2.3 Muon and electron efficiency toy Monte-Carlo	113
14.2.4 Theoretical uncertainty	113
14.3 Theoretical uncertainty on $A_{W/Z}$ and $E_{W/Z}$ factors	115
14.4 Correlation between uncertainties	115
14.4.1 Treatment of partially correlated uncertainties	116
15 Results of the cross-section measurement	119
15.1 Cross-sections results	119
15.1.1 Lepton universality test	120
15.2 Combined results	121
15.2.1 Cross-sections ratios	121
15.3 Comparison with theoretical predictions	122
15.4 Effect on PDF distributions	122
16 Summary	125
Bibliography	127

1 Chapter 1

2 Thesis organization

3 This thesis presents the measurement of $W \rightarrow l\nu$ and $Z \rightarrow ll$ cross-sections in electron in muon
4 channels in 2.76 TeV data collected by ATLAS experiment.

5 The thesis is organized in a three parts. The theoretical input is described in part 1. The experi-
6 mental input and a software organization is explained in a part 2. The cross-section measurement
7 performed by the author is described in part 3. The results and its interpretation via parton density
8 functions is presented in a final part.

9 The work presented was performed within the ATLAS collaboration. All plots in the thesis were
10 produced by the author, unless it is referenced otherwise.

11 The theoretical input is presented in part 1 and chapters:

12 **Chapter 2 Theoretical introduction**, contains brief overview of the current status of Standard
13 Model and the proton structure

14 **Chapter 3 Methodology**, describes methods of cross-section and their ratios calculation and meth-
15 ods of determination of effect of this cross-section on a PDF distributions.

16 The experimental setup is described in the part 2 and following chapters:

17 **Chapter 4 The LHC and ATLAS experiment** gives an overview of the LHC accelerator complex
18 and its experiments and the ATLAS detector, used to collect data for this analysis

19 **Chapter 5 Event reconstruction** contains the detailed description of event reconstruction. The
20 study of missing transverse energy reconstruction algorithm was presented by author. It was
21 figured out, that for 2.76 TeV data the non-standard procedure is needed.

22 **Chapter 6 Monte-Carlo** provides an information of Monte-Carlo simulation steps and generators,
23 used in this analysis

24 **Chapter 7 Frozen showers** gives an description of Frozen Showers method for fast Monte-Carlo
25 simulation. The machine learning method for its optimization, made by author, is presented.

26 **Chapter 8 Data and Monte-Carlo samples** describes a data and Monte-Carlo samples, used in
27 the analysis.

28 The following chapters presents a work, done by author, unless other is specified:

29 **Chapter 9 Event selection** gives a set of selection criteria used to derive $W \rightarrow l\nu$ and $Z \rightarrow ll$ in
30 collected data

- 31 **Chapter 10 Monte-Carlo corrections** presents the correction, applied on Monte-Carlo in order
32 to gain better data vs Monte-Carlo agreement. The correction factors have been derived by
33 performance group, except for muon trigger scale factors, determined by the author.
- 34 **Chapter 11 Hadronic recoil calibration** describes a method of missing transverse energy calibration
35 in 2.76 GeV data and methods of the corresponding uncertainty determination.
- 36 **Chapter 12 Background estimation** provides a description of main backgrounds, that can pass
37 the selection criteria and techniques of their contribution estimation
- 38 **Chapter 13 Control distributions** shows the agreement between data and Monte-Carlo simulation
39 for all analyses and different distributions.
- 40 **Chapter 14 Uncertainties of the cross-section measurements** presents main sources of exper-
41 imental and theoretical uncertainties and gives a methods of their propagation to the final
42 cross-sections and their ratios.
- 43 **Chapter 15 Results of the cross-section measurements** presents the results of cross-section
44 measurement of $W \rightarrow l\nu$ and $Z \rightarrow ll$ in electron and muon channels separately, results of
45 combined cross-sections and their ratios and effect of this measurement on PDF distributions.

46

Part I

47

Theory introduction

48

Chapter 2

49 Theoretical introduction

50 2.1 Standard model

51 2.2 Theory of pp collisions

52 2.3 Proton structure

53 Chapter 3

54 **Methodology of the measurement**

55
56
57
58
59
60
61
62
63
64
65
66

3.1	Cross-Section methodology	7
3.1.1	Fiducial phase-space definition	8
3.1.2	Extrapolation to the 13 TeV fiducial phase-space	8
3.1.3	Combination of W^+ and W^- cross-sections	9
3.2	Ratios calculation	9
3.3	Combination of electron and muon cross-section measurements	10
3.4	PDF fits	11

67 **3.1 Cross-Section methodology**

The production cross-section of W and Z bosons in a fiducial region, corresponding to the geometrical acceptance of the detector and of the kinematic selection, measured using the equation:

$$\sigma_{W/Z}^{fid} = \frac{N^{W/Z} - B^{W/Z}}{C_{W/Z} L_{int}} = \frac{N_{sig}^{W/Z}}{C_{W/Z} L_{int}}, \quad (3.1)$$

68 where

- 69 • N is the number of candidates measured in a data
- 70 • B is the number of background events
- 71 • $N_{sig}^{W/Z} = N^{W/Z} - B^{W/Z}$ of the signal events
- 72 • L_{int} is the integrated luminosity corresponding to a run selections and trigger requirements
- 73 • $C_{W/Z}$ is a correction factor for an experimental selection and resolution effects.

The correction factors $C_{W/Z}$ is calculated from MC for each process and each decay channel separately and defined as :

$$C_{W/Z} = \frac{N_{MC,rec}}{N_{MC,gen,cut}}, \quad (3.2)$$

74 where $N_{MC,rec}$ are sums of weights of events after simulation, reconstruction and selection, $N_{MC,gen,cut}$
75 - are taken on the generator level after fiducial cuts. These correction factor are including efficiencies
76 for trigger, reconstruction and identification (see Sec.10.1).

In addition, this measurement could be extrapolated to the full phase-space using as:

$$\sigma_{W/Z}^{tot} = \frac{\sigma_{W/Z}^{fid}}{A_{W/Z}} = \frac{N_{sig}^{W/Z}}{A_{W/Z} C_{W/Z} L_{int}}, \quad (3.3)$$

77 where $\sigma_{W/Z}^{tot}$ are the total inclusive production cross-section of the W and Z bosons, and $A_{W/Z}$ is an
78 acceptance.

The $A_{W/Z}$ factor determined from Monte Carlo simulation as:

$$A_{W/Z} = \frac{N_{MC,gen,cut}}{N_{MC,gen,all}}, \quad (3.4)$$

79 where $N_{MC,gen,all}$ are the sum of weights of all generated MC events. Both $A_{W/Z}$ and $C_{W/Z}$ are defined
80 at the "born level", i.e. before the decay leptons emit photons via QED final state radiation.

81 3.1.1 Fiducial phase-space definition

82 The definition of fiducial volume for W bosons in both electron and muon channels is:

- 83 • $P_T^l > 20$ GeV
- 84 • $|\eta^l| < 2.5$
- 85 • $P_T^\nu > 25$ GeV
- 86 • $M_T^W > 40$ GeV

where P_T^l and P_T^ν are the charged lepton and neutrino transverse momentums respectively, η^l is a lepton pseudo-rapidity, and M_T^W is the transverse mass, defined as:

$$M_T^W = \sqrt{2P_T^l \cdot P_T^\nu [1 - \cos(\phi_l - \phi_\nu)]}, \quad (3.5)$$

87 where ϕ_l is an azimuthal angle of the charged lepton and ϕ_ν is an azimuthal angle of neutrino.

88 For the Z boson measurement fiducial phase-space is defined as:

- 89 • $P_T^l > 20$ GeV
- 90 • $|\eta^l| < 2.5$
- 91 • 66 GeV $< M_Z < 116$ GeV

92 where M_Z is an di-lepton invariant mass.

93 3.1.2 Extrapolation to the 13 TeV fiducial phase-space

Since the 13 TeV inclusive cross-section measurement uses another definition of the fiducial phase space, it is possible to extrapolate cross-section to a new fiducial phase-space as:

$$\sigma_{W/Z}^{fid,13} = \frac{\sigma_{W/Z}^{fid}}{E_{W/Z}}, \quad (3.6)$$

where $E_{W/Z}$ is an additional extrapolation factor:

$$E_{W/Z} = \frac{N_{MC,gen,cut}}{N_{MC,gen,cut^{new}}}, \quad (3.7)$$

where $N_{MC,gen,cut^{new}}$ is the sum of the weights of Monte-Carlo events after the new set of cuts on the generator level.

The 13 TeV fiducial phase-space is defined as:

• $P_T^l > 25$ GeV

• $|\eta^l| < 2.5$

• $P_T^\nu > 25$ GeV

• $M_T^W > 50$ GeV

for the W decays and

• $P_T^l > 25$ GeV

• $|\eta^l| < 2.5$

• 66 GeV $< m_Z < 116$ GeV

for the Z measurements.

3.1.3 Combination of W^+ and W^- cross-sections

In this analysis cross-section of W boson is calculated indirectly by combining W^+ and W^- cross-sections the following way:

$$\sigma_W = \sigma_{W^+} + \sigma_{W^-} = \frac{1}{L_{int}} \cdot \left(\frac{N_{sig}^{W^+}}{A_{W^+} C_{W^+}} + \frac{N_{sig}^{W^-}}{A_{W^-} C_{W^-}} \right), \quad (3.8)$$

The absolute uncertainty of this measurement is calculated from uncertainties of W^+ and W^- cross-sections as:

$$(\delta X_W)^2 = (\delta X_{W^+})^2 + (\delta X_{W^-})^2 + 2 \cdot \rho_{W^+W^-}^X \delta X_{W^+} \delta X_{W^-}, \quad (3.9)$$

where δX is a systematic component on the cross-section and $\rho_{W^+W^-}^X$ is a correlation between W^+ and W^- for this component, which will be estimated in Chap. 14.

3.2 Ratios calculation

The ratio for two cross-section measurements σ_i and σ_j is calculated as:

$$R_{i,j} = \frac{\sigma_i}{\sigma_j} = \frac{\frac{N_{sig}^i}{A_{W/Z}^i C_{W/Z}^i L_{int}}}{\frac{N_{sig}^j}{A_{W/Z}^j C_{W/Z}^j L_{int}}} = \frac{N_{sig}^i}{N_{sig}^j} \cdot \frac{A_{W/Z}^j}{A_{W/Z}^i} \cdot \frac{C_{W/Z}^i}{C_{W/Z}^j} = \frac{N_{sig}^i}{N_{sig}^j} \cdot A_{i/j} C_{i/j}, \quad (3.10)$$

The relative uncertainty is therefore can be obtained, taking into account correlation between two measurements as:

$$\left(\frac{\delta R}{R}\right)^2 = \left(\frac{\delta N_{sig}^i}{N_{sig}^i}\right)^2 + \left(\frac{\delta N_{sig}^j}{N_{sig}^j}\right)^2 + \left(\frac{\delta A_{i/j}}{A_{i/j}}\right)^2 + \left(\frac{\delta C_{i/j}}{C_{i/j}}\right)^2 \quad (3.11)$$

Uncertainties on first two terms is considered to be uncorrelated, while other are derived using the following error propagation formula:

$$\left(\frac{\delta X_{i/j}}{X_{i/j}}\right)^2 = \left(\frac{\delta X_i}{X_i}\right)^2 + \left(\frac{\delta X_j}{X_j}\right)^2 - 2\rho_{ij} \frac{\delta X_i}{X_i} \frac{\delta X_j}{X_j}, \quad (3.12)$$

- ¹¹⁰ where X is a systematic component on the A or C and ρ_{ij} is a correlation between two estimates.
- ¹¹¹ Estimation of correlation parameters will be discussed in Chap. 14.

3.3 Combination of electron and muon cross-section measurements

The probability density function for a "true" value m to get a value μ with uncertainty Δ in measurement is:

$$P(m) = \frac{1}{\sqrt{2\pi\Delta}} \exp\left(-\frac{(m-\mu)^2}{2\Delta^2}\right), \quad (3.13)$$

where it is assumed, that the uncertainty has a Gaussian shape. The corresponding χ^2 function is:

$$\chi^2(m) = \frac{(m-\mu)^2}{\Delta^2}. \quad (3.14)$$

In case of N statistically independent measurements, the probability density function is proportional to:

$$P(m) \propto \prod_{i=0}^N \exp\left(-\frac{(m-\mu_i)^2}{2\Delta_i^2}\right), \quad (3.15)$$

which corresponds to the χ_{sum}^2 :

$$\chi_{sum}^2(m) = \sum_i \chi_i^2 = \sum_i \frac{(m-\mu_i)^2}{\Delta_i^2}, \quad (3.16)$$

that can be rewritten in the form of the Eq. 3.14:

$$\chi_{sum}^2(m) = \frac{(m-\mu_{ave})^2}{\Delta_{ave}^2} + \chi_0^2, \quad (3.17)$$

- ¹¹³ where μ_{ave} and Δ_{ave} are the average value and its uncertainty. These values are found by minimizing χ_{sum}^2 with the respect to m. Value χ_0^2 indicate a consistency of the measurements and should be $\chi_0^2/N \approx 1$.

Systematic uncertainties can be treated as a result of an experiment (e.g. measurement of the calibration) and added to the χ^2 as:

$$\chi_{syst}^2(\alpha) = \frac{\alpha - \alpha_0}{\Delta_\alpha^2} \equiv b^2, \quad (3.18)$$

where nuisance parameter \mathbf{b} corresponds to a coherent change of the measurements $\mu_i \rightarrow \mu_i + \mathbf{b}\mathbf{F}_i$. Using this nuisance representation, Eq. 3.17 can be rewritten in more general way:

$$\chi^2_{sum}(\mathbf{m}, \mathbf{b}) = \sum_i \frac{(m - \mu_i - \sum_j \Gamma_i^j b_j)^2}{\Delta_i^2} + \sum_j b_j^2, \quad (3.19)$$

116 where

- 117 • i runs over all experiments used in averaging.
- 118 • \mathbf{b} is the vector of nuisance parameters b_j corresponding to each source of systematic uncer-
- 119 tainty
- 120 • Γ_i^j is the absolute correlated systematic uncertainty
- 121 • Δ_i^2 is the uncorrelated (statistical) uncertainty.

122 3.4 PDF fits

123 In this thesis the xfitter program have been used for determine the parton distribution functions. In
 124 this section the main fit formalism used is presented in details, such as parametrisation of the PDFs
 125 at the starting scale, definition of χ^2 and treatment of experimental uncertainties.

The parton distribution functions can be parametrized differently at the starting scale Q_0^2 . Standard form, adapted by PDF groups, uses a simple polynomial for interpolation between low and high x regions:

$$xf(x; Q_0^2) = Ax^B(1-x)^C P_i(x), \quad (3.20)$$

126 where P_i is a polynomial of some order. In this analysis a standard HERA style parametrisation is
 127 used, so its implementation will be discussed in details

128 There are, in principle, 11 different partons to consider, however heavy parton (c and d quarks)
 129 distributions can be determined perturbatively, that leaves at least 7 independent combinations.
 130 The parameterised PDS at HERA are the valence distributions xu_v and xd_v , the gluon distribution
 131 xg , and the u-type and d-type sea $x\bar{U}$ and $x\bar{D}$, where:

$$xu_v = xu - x\bar{u}, \quad xd_v = xd - x\bar{d}, \quad x\bar{U} = x\bar{u}, \quad x\bar{D} = x\bar{d} + x\bar{s}.$$

132 For the strange quark distributions it is assumed, that $xs = x\bar{s} = f_s x\bar{D}$ at Q_0^2 , where $f_s = 0.31$ - is
 133 a strange fraction chosen to match the experiment data.

The following functional form is used for parametrization:

$$xf(x; Q_0^2) = Ax^B(1-x)^C(1+Dx+Ex^2), \quad (3.21)$$

135 where A_{uv} , A_{dv} and A_g are constrained by the number sum-rules and the momentum sum-rule, and
 136 the parameters $B_{\bar{U}}$ and $B_{\bar{D}}$ are set equal, so there is a single parameter for the sea distributions.

Similarly to averaging procedure, the nuisance parameters representation of the systematic un-
 certainties is used:

$$\mu_i = m_i(\mathbf{p}) + r_i \sigma_i + \sum_{\alpha=1}^{N_{syst}} \Gamma_\alpha^i b_\alpha, \quad (3.22)$$

137 where:

- 138 • $m_i(\mathbf{p})$ is the true value, that depends on set of parameters $\mathbf{p} = (p_1, p_2, \dots)$
- 139 • μ_i is the value, observed in the experiment,
- 140 • σ_i is the statistical and systematic uncertainty,
- 141 • Γ_α^i is the sensitivity of i-th measurement to the correlated systematic source α ,
- 142 • r_i are the normal random variables
- 143 • b_α are the nuisance parameters.

The simple parametrisation form of χ^2 is defined in Eq. 3.19. This equation can be rewritten using a Poisson distribution for statistical error:

$$\chi_{sum}^2(\mathbf{m}, \mathbf{b}) = \sum_i \frac{(m - \mu_i - \sum_j \Gamma_i^j b_j)^2}{\delta_{i,stat}^2 \mu^i m^i \prod_\alpha \exp(-\gamma_\alpha^i b_\alpha)} + \sum_\alpha b_\alpha^2, \quad (3.23)$$

144 The PDF uncertainties are estimated by varying the data points within their statistical and sys-
 145 tematic uncertainties using a Monte-Carlo technique. For each data set an QCD fit is performed to
 146 extract the PDF set. Typical number of data sets is N>100. The pdf uncertainties are estimated using
 147 the values and RMS of the replicas.

The profiling method allows to update the It is also possible to include the theoretical uncertainties in the nuisance parameters representation \mathbf{b}_{th} :

$$\chi_{sum}^2(\mathbf{m}, \mathbf{b}_{exp}, \mathbf{b}_{th}) = \sum_i \frac{(m - \mu_i - \sum_j \Gamma_i^j b_j)^2}{\delta_{i,stat}^2 \mu^i m^i \prod_\alpha \exp(-\gamma_\alpha^i b_\alpha)} + \sum_\alpha b_\alpha^2, \quad (3.24)$$

148

Part II

149

Experimental setup

150 Chapter **4**

151 **The Large Hadron Collider (LHC) and the**
152 **ATLAS experiment.**

153	4.1 The LHC and accelerator complex	15
154	4.2 The ATLAS experiment	17
155	4.2.1 Coordinates and kinematic variables	18
156	4.2.2 Inner detector	18
157	4.2.3 Calorimeters	19
158	4.2.4 Muon spectrometer	23
159	4.2.5 Trigger system	23
160	4.3 Luminosity measurement	24
161		
162		
163		

166 Particle physics requires to build a large machine for probing it theories. This a modern field of the
167 physics, that pushes a limits of engineering. In this section an overview of the experimental setup,
168 used to collect a data for this analysis will be given. The first section introduces an cutting edge of
169 particle accelerators: LHC. In the send section an ATLAS detector will be described.

170 **4.1 The LHC and accelerator complex**

171 Large hadron collider is the largest accelerator in the world. It was build in Geneva, Switzerland and
172 started its operation with the first collisions in 2009. It lies in a tunnel 27 kilometers in circumference.
173 It operates with pp and Pb-Pb beams with centre-of-mass energies up to 14 GeV. It was designed
174 to make a precise studies of Standard Model predictions and to search for a new physics beyond
175 standard model, such as supersymmetry. The heavy ion program serves a purpose of studying
176 matter properties and a quark-gluon plasma.

177 Beams acceleration consists of several stages, as it shown in Fig. 4.1. The beam source is a hydrogen
178 gas or lead source in case of the heavy ion. An electrical current is used to remove the electrons
179 from each atom, and then the ion begin its ride through the only linear accelerator in the chain
180 LINAC2, that accelerates protons up to 50 GeV or LINAC3 with up to 3.2 GeV/nucleon. The proton
181 beams from linac are ejected into the PS booster, where they are further accelerated to 1.4 GeV.
182 During a heavy ion operations nucleons from LINAC3 are injected into the Low Energy Ion Ring (LEIR)
183 and are accelerated up to 72.2 MeV/nucleon before injecting into PS. The last steps before ejecting
184 beams to the LHC are the rings of the Proton Synchrotron (PS) and Super Proton Synchrotron (SPC)

185 that accelerates protons to 25 and 450 GeV respectively. The bunch structure of the beam is formed
 186 at PS step and has a nominal pattern of 39 groups of 72 bunches with time 25-50 ns time spacing.
 187

188 In LHC beams are accelerated up to 7 TeV (yet 6.5 TeV achieved). The beams are circulating
 189 in opposite directions inside one of the 2 beam pipes, that are 6.3 cm in diameter. In order to
 190 bend beam trajectory, the pipes are surrounded by a 1232 superconducting dipole magnets. The
 191 superconducting cavities are used to accelerate the protons and maintain beam constant energy
 192 during the operation time.

193 As most of the circular colliders, LHC has several experiments installed in the regions, where
 194 beams are intersecting, that allows them to collect data in parallel. The main experiments are:

195 **ALICE** A large Ion Collider Experiment - a dedicated heavy ion detector, build to in the physics of
 196 strongly interacting matter, where a new phase of mater (quark-gluon plasma) is expected.

197 **ATLAS** A Toroidal LHC ApparatuS is a largest particle detector build. It is a general purpose detector,
 198 that is used to study QCD and a Standard Model predictions and searches for a new physics.
 A detailed description of this detector is given in Sec. 4.2.

199 **CMS** the Compact Muon Solenoid is an another multiple purpose detector at LHC, build with the
 200 different technologies in the respect to ATLAS.

201 **LHCb** the Large Hadron Collider beauty is specialized for measurement of heavy (charm and bottom)
 202 quark properties, that allows to study the parameters of CP violation.

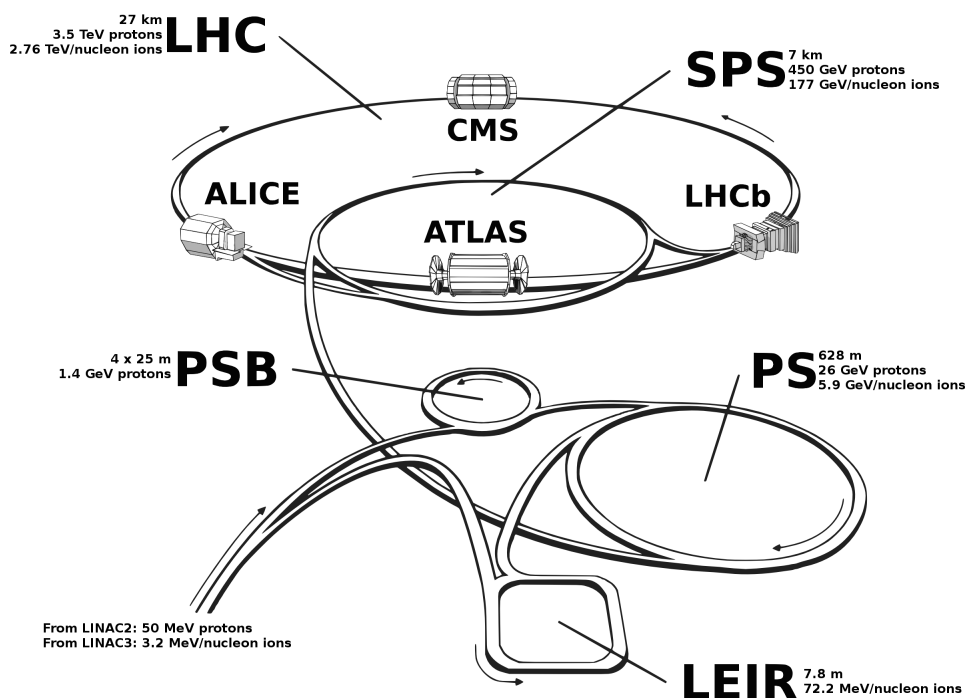


Fig. 4.1: The LHC acceleration complex [1]

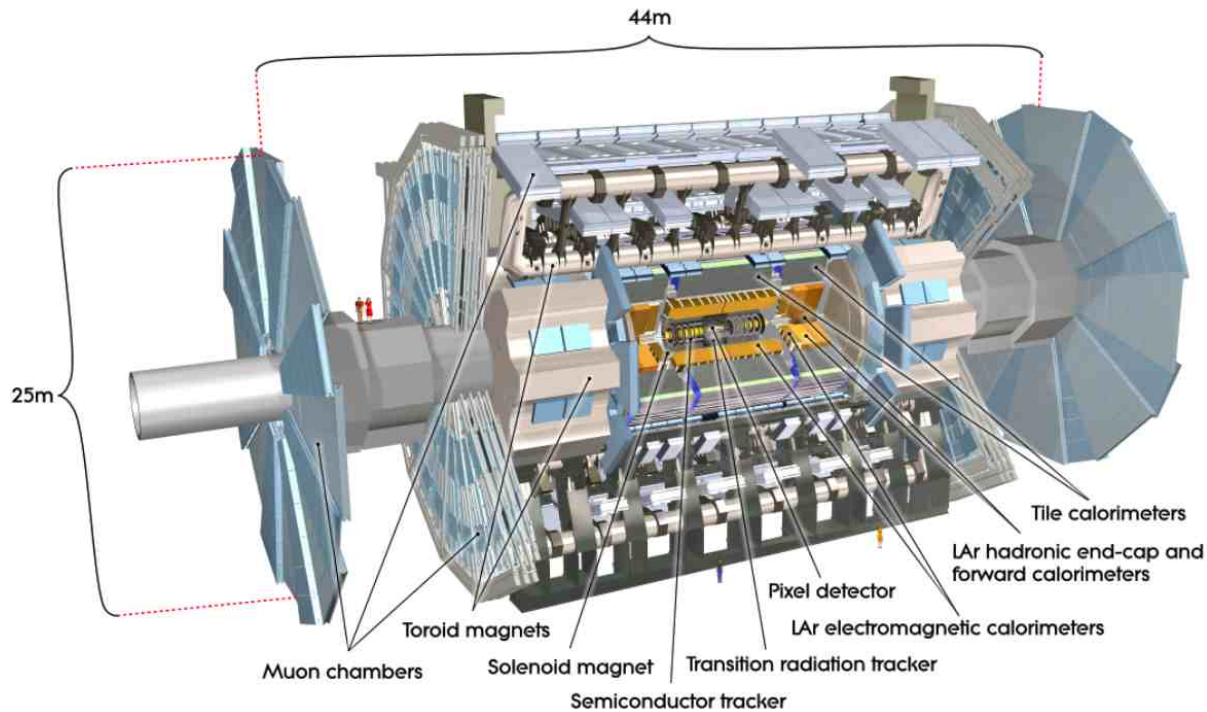


Fig. 4.2: The ATLAS detector [2]

4.2 The ATLAS experiment

ATLAS is a multi-purpose detector. It is used to perform different types of analysis. It is supposed to operate for 2 decades.

The physics goals and signatures of the particles are putting a strict set of requirements on ATLAS detector. Heavy particles, born in pp collisions are expected to decay almost immediately. Thus their properties are measured only indirectly through their decay products, that should be detected and identified. Good identification efficiency of photons, electrons and hadrons is achieved by the system of calorimeters. Because muons are minimum ionizing particles, they go further, than most of the particles, the special outer detector system is build. B-hadrons travel to the distance around 1 mm, producing a secondary vertex, so the vertex detectors near interaction point should be able to detect this. Neutrino from the decays are leaving the detector without interacting with it. However, it is possible to measure them through the energy imbalance in the detector. This means, that detector should cover a hermetically closed area near interaction point, so that no information is missed. Radiation hardness for all of the detectors and electronic is required because of the LHC harsh environment.

The ATLAS detector can be divided into 3 main subdetectors, each serving its own purpose

- The Inner Detector (ID), that is used for tracking and precise measurement of particles momentum
- The Calorimetry system that is used to measure the energies of electrons, photons and hadrons and to identify them
- Muon system designed to detect muons and measure their parameters.

224 Each subdetector can be divided into 3 parts: the barrel region near the interaction point and
 225 end-cap in the forward directions. The magnet system is used for tracking of charged particles
 226 for measurements of momentum and charge. The ATLAS detector has 4 large superconducting
 227 magnet: solenoid, build around inner detector and 3 toroids (end-cap and forward) used for the
 228 muon spectrometer.

229 4.2.1 Coordinates and kinematic variables

230 The detector shape motivates the choice of the coordinate system. It is natural to choose z axis
 231 to be aligned with the beam, with the start in interaction point, while leaving x and y axis to be
 232 perpendicular to it. Because of detector symmetry along the beam z axis, the cylindrical coordinates
 233 are often used, with the radial distance $r = \sqrt{x^2 + y^2}$ and the polar θ and azimuth ϕ angles.

The direction of the particles can be quantified via rapidity:

$$y = \ln \sqrt{\frac{E + p_z}{E - p_z}}, \quad (4.1)$$

where E is the energy of the particle and p_z is z component of the momentum. In the limit of the vanishing masses, this quantity is converges to another widely used variable called pseudorapidity:

$$\eta = -\ln \left[\tan \left(\frac{\theta}{2} \right) \right]. \quad (4.2)$$

234 It is preferred over the polar angle, because the differences in pseudorapidity is the Lorentz invariant
 235 along the boost in the beam direction.

The spacial distance between two Lorentz vectors is defined as:

$$\Delta R = \sqrt{(\Delta\eta)^2 + (\Delta\phi)^2}. \quad (4.3)$$

The transverse momentum is defined as:

$$p_T = \sqrt{p_x^2 + p_y^2}, \quad (4.4)$$

236 where p_x and p_y are the x and y components of the particle momentum. Because the incoming
 237 protons are alligned along the z axis, the total transverse momentum (together with non-interacting
 238 particles) in the detector should be fixed to 0.

239 4.2.2 Inner detector

240 The Inner Detector (ID) is the closest to the interaction point detector system. It used for recon-
 241 struction of charged particles tracks and vertexes. Approximately 1000 particles are emerging during
 242 one collision within Inner Detector (ID) acceptance ($|\eta| < 2.5$). In order to achieve a good momentum
 243 and verex resolution it is required to use a high granularity detector. The layout of ID is shown in
 244 Fig. 4.3.

245 The inner detector consists of 3 sub-detectors:

- 246 • The precise reconstruction of vertexes with spacial resolution of 1 mm achieved because
 247 of the pixel detectors, placed close to the interaction point. The pixel detector consists of
 248 approximately 80.4 million readout channel placed in 3 barrel and 3 disk layers at the end of

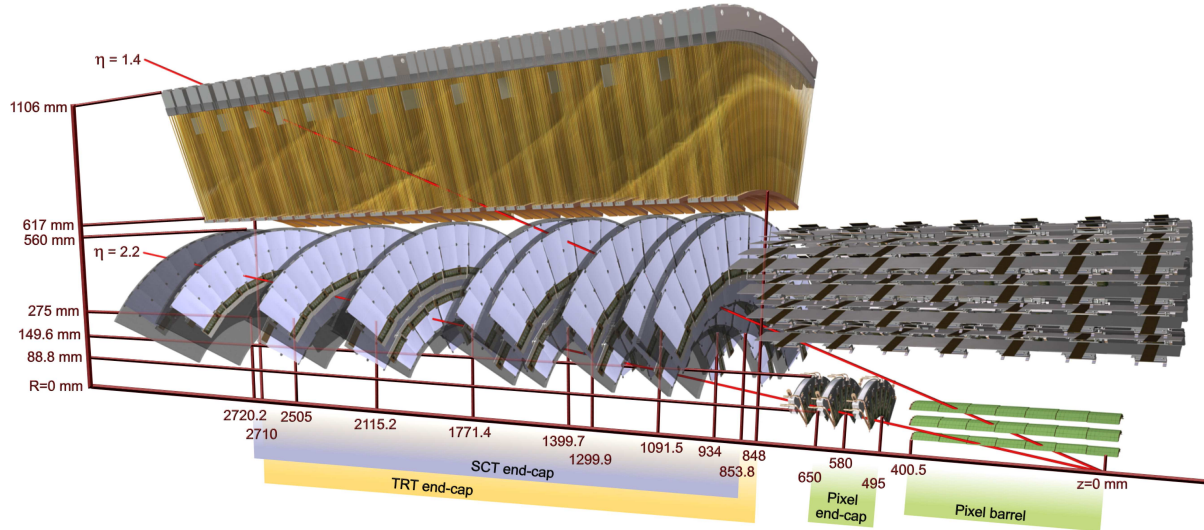


Fig. 4.3: Cut-away view of the ATLAS Inner Detector. Drawing is showing the sensors and structural elements traversed by two charged tracks of 10GeV pT in the end-cap inner detector [3]

each barrel region. Each pixel module made of the silicon layer and s lower layer of electronics. Charged particle, passing through the module, creates a movement of electron-hole pair, that causes a current in the readout electronics.

- The silicon strip detector (SCT) consists of 6.3 million readout channel. It gives a significant contribution on a measurement of charged particle momentum, because of the large number of hits particle produce in the detector. It works in a similar way with pixel detector, however has a smaller precision. Each track crosses around 8 strip layers.
- Transition radiation tracker (TRT) consists of the straw tubes and provides the largest number of hits (~ 36 per track). Each straw is a polimide drift tube 4 mm in a diameter. The tubes are placed parallel to the beam in the barrel region and radially in the wheels.

The combination of the precision measurements near the interaction point and big amount of hits at larger distances allows atlas to have a good precision of the coordinates measurements.

4.2.3 Calorimeters

The calorimeter system is used to measure position and energy of particles from their deposits in the material. The general structure of ATLAS calorimeter is shown in Fig. 4.4. The calorimetric system consists of barrel ($|\eta| < 3.2$) and two end-cap parts ($3.1 < |\eta| < 4.9$). The central part used of the high precision measurements, while the end-cap part has a coarser granularity and mostly used for jet reconstruction and E_T^{miss} measurements.

Particles, entering the calorimeter, produce a cascade of the secondary particles called a particle shower. Each shower is registered by the set of smallest structures of calorimeter providing the response, called cells. Cell structure, called shower shape, differs for different types of particles and used for identification. Each calorimeter also has a dead material, that is used to absorb particles and does not produce any signal response. The full particle energy is reconstructed from the ratio between amount of energy absorbed in dead and active material.

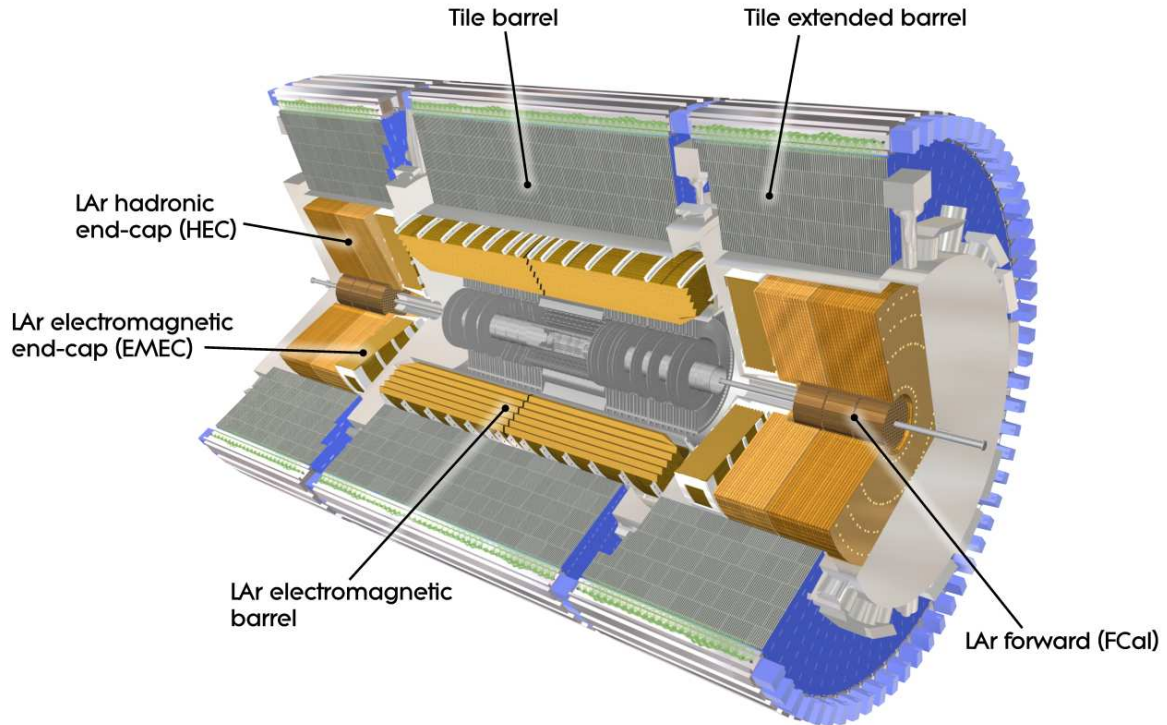


Fig. 4.4: Cut-away view of the ATLAS calorimeter system [3]

273 In order to measure the energy of the particle properly, shower should be fully contained by the
 274 calorimeter. Since depth of the shower, caused by electromagnetic particle is significantly smaller,
 275 than depth of the hadronic shower, calorimeters are divided into two types: electromagnetic (EM)
 276 and hadronic. EM calorimeters are placed closer to the interaction point and has smaller amount of
 277 the dead material, compared to the hadronic calorimeters.

278 The central region calorimeters are required to have high granularity for combination with ID
 279 information and a precision measurement of photons and electrons. Forward part has a smaller
 280 granularity and mostly used for jet reconstruction and missing transverse energy measurements.

281 **Electromagnetic calorimeter**

282 The main purpose of electromagnetic calorimeter is to measure energies of electrons and photons.
 283 The EM showers starts from initial high-energy electron and photon entering the calorimeter. High-
 284 energy photons are loosing their energy via production of electron-positron pairs, while electrons
 285 and positrons are emitting photons via Bremsstrahlung. These two processes continues till the photon
 286 reaches the pair production threshold.

287 The EM calorimeter consists of a barrel part (EM barrel = EMB) and two symmetric end-caps (EM
 288 end-cap = EMEC), that cover a range of pseudorapidity $|\eta| < 1.475$ and $1.5 < |\eta| < 3.2$ respectively.
 289 These calorimeters have an accordion structure, as shown in Fig. 4.5. This geometry allows to have a
 290 full coverage in ϕ coordinate. It consists of the layers of lead/steel interplaced with liquid argon, that
 291 acts as a sensitive material, and electronics.

292 There are four samplings in EMB calorimeter, as showed in Fig. 4.5:

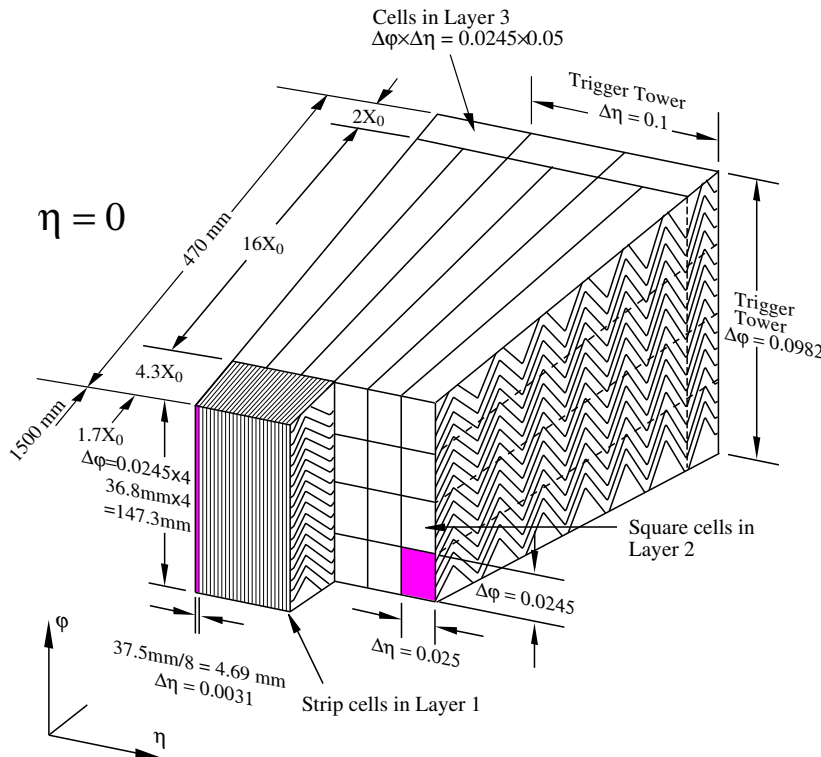


Fig. 4.5: The sketch of EMB module. The granularity in η and ϕ of the cells of each of the three layers and of the trigger towers is also shown [3]

293 **presampler** A single layer of LAr without dead material in front of it. It allows to correct for the
294 energy losses in front of the calorimeter.

295 **1st sampling** The first layer has a fine segmentation in η with thin η strips with size $\Delta\eta \times \Delta\phi =$
296 0.0031×0.098 . Because of the resolution this layer provides an information for γ and π^0
297 separation.

298 **2nd sampling** The majority of the energy is deposited in the second sampling layer. It consists of
299 the square cells with size $\Delta\eta \times \Delta\phi = 0.0245 \times 0.0245$.

300 **3rd sampling** Just the highest energy electrons are reaching the third layer, therefore it has a bigger
301 cell size.

302 Each wheel of the EMEC calorimeter consists of the 2 co-axial wheels: Inner Wheel (IW) and Outer
303 Wheel (OW). Each endcap wheel is divided into 8 wedge-shaped modules. <MORE ABOUT EMEC.
304 <Add about trigger>

305 **Hadronic calorimeters**

306 The mechanism of hadronic shower development differs from the electromagnetic one. The main
307 physical processes, that are determining the shower development are: hadron production, nuclear
308 deexcitation and pion and muon decays. It usually takes longer to develop a hadronic shower, than
309 an EM one.

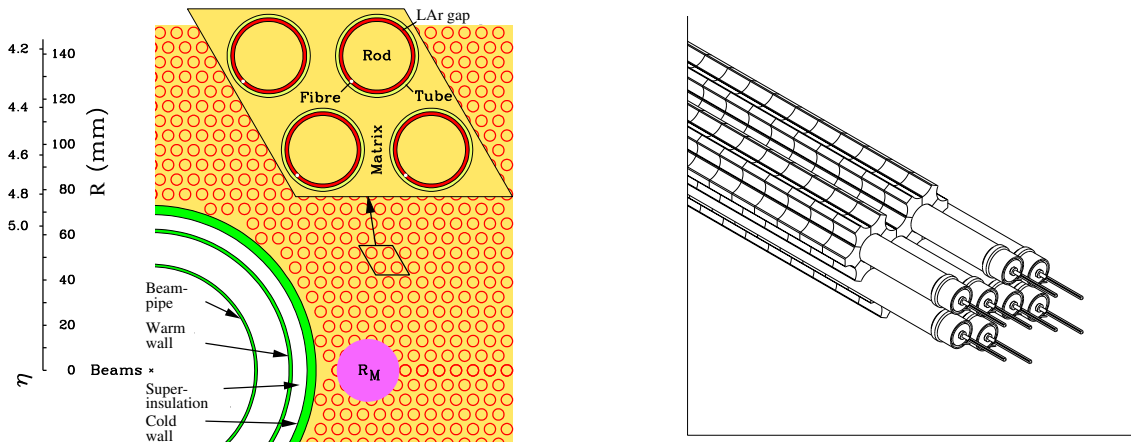


Fig. 4.6: Electrode structure of FCAL1 with the matrix of copper plates and copper tubes and rods with the LAr gap for electrodes [3]

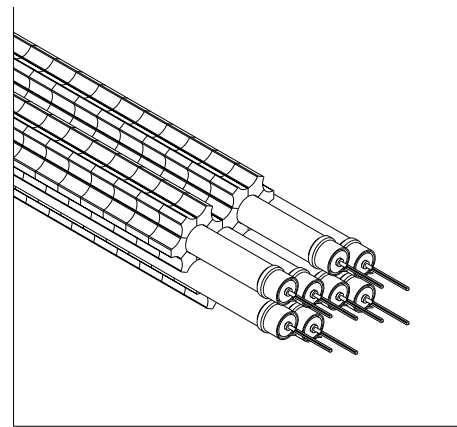


Fig. 4.7: View of the FCAL hadronic module absorber matrix, including a set of tungsten rods and copper tubes surrounded by 1 cm long tungsten slugs [3]

310 The ATLAS hadronic calorimeter consists of the tile and liquid argon Hadronic End-cap Calorimeter
311 (HEC). The forward part of the hadronic calorimeter will be discussed separately.

312 The tile calorimeter placed right after the EMEC and covers a pseudorapidity range up to $|\eta| < 1.0$ in
313 the barrel region and $0.8 < |\eta| < 1.7$ in the 2 end-caps. It is a sampling calorimeter with steel acting as
314 a dead material and scintillator ties for a sensitive material. The readout from scintillator performed
315 using the wavelength shifting fibers. The readout cells are build by grouping the fibers into the
316 photomultiplier. Granularity of the detector

317 The HEC calorimeter uses a liquid argon as a sensitive material and shares the same LAr cryostat
318 with EMEC. The copper-plate are acting as an absorbers with a flat-plate design. The size of the cell
319 in HEC is $\Delta\eta \times \Delta\phi = 0.1 \times 0.1$ for $|\eta| < 2.5$ and $\Delta\eta \times \Delta\phi = 0.2 \times 0.2$ for forward region $|\eta| > 2.5$

320 Forward calorimeter

321 The forward calorimeter (FCAL) is placed in the same cryostat with EMEC and covers the range of
322 pseudorapidity $3.1 < |\eta| < 4.9$. It is placed 4.7 m away from the interaction point and imposed for a
323 high fluxed. This motivates the choice of detector design with small amount of the sensitive material.
324 The FCAL module consists of the co-axial copper rod and anode tube, separated by the wire around
325 the rod. The LAr fills the gap between rod and anode. Small size of the gaps allows to have faster
326 signal transfer together with avoiding signal degradation caused by distortion of the electric field in the
327 gap (some reference). The structure of one of the FCAL calorimeters is shown in Fig. 4.6.

328 The FCAL is divided into 3 modules: one electromagnetic FCAL1 and 2 hadronic FCAL2 and FCAL3.
329 Parameters of these modules are summarized in Tab. 4.1. In hadronic modules it was decided to use
330 a tungsten instead of the copper in order to optimize the high absorption length. These modules
331 a similar to the FCAL1, except for the use of tungsten rods instead of the copper rods. The space
332 between the end-plates and tubes is filled with tungsten slugs, as shown in Fig. 4.7.

333 The electrodes are forming the readout cells from the group of four, six and nine for FCAL1, FCAL2
334 and FCAL3 respectively. The granularity of the detector is about $\Delta\eta \times \Delta\phi \approx 0.2 \times 0.2$

Table 4.1: Table of parameters for the three FCAL modules

Calorimeter	Type	Absorber	Gap width (μm)	Number of electrodes	Number of readout channels
FCAL1	electromagnetic	coper	250	12 260	1008
FCAL2	Hadronic	tungsten	375	10 200	500
FCAL2	Hadronic	tungsten	500	8 224	254

335

4.2.4 Muon spectrometer

336 The muon trajectories are already measured in the ID, however for a high P_T muons it could be
 337 difficult to make a precise determination of charge and momentum. The Muon Spectrometer (MS)
 338 provides an information at a much larger scales to measure the bending of the trajectory because
 339 of the magnetic field. The MS is placed in the most outer part of the ATLAS detector, behind the
 340 calorimeters. The amount of the mateiral in front of the MS is adjusted so, that it can be assumed,
 341 that all of the particles entering the it are muons.

342 The muon spectrometer covers the area up to $|\eta| < 2.7$ and allows to trigger on these particles
 343 in the range $|\eta| < 2.4$. The precision tracking is performed by the Monitored Drift Tubes (MDT). The
 344 MDT consists of 8 layers of the drift tubes and allowing to have a resolution of $80 \mu m$ per tube
 345 or $35 \mu m$ per chamber. In addition, in forward region $2.0 < |\eta| < 2.7$, the Cathode-Strip Chambers
 346 (CSC) are used. The CSC are the multiwire proportional chambers and giving a resolution $40 \mu m$ in
 347 the bending plane and 5 mm in the transverse plane.

348 The trigger system in muon spectrometer is composed from the fast detectors namely Resistive
 349 Plate Chambers (RPC) and Thin Gap Chambers (TGC) in the barrel($|\eta| < 1.05$) and end-cap ($1.05 < |\eta|$
 350 < 2.4) regions respectively.

351

4.2.5 Trigger system

352 Processing and storing of the events is a difficult task at LHC. The collision frequency at LHC is 40
 353 MHz. The full readout information of 1 second of operation requires requires 1 Tb of storage space.
 354 However, the events of interest (such as production of bosons) makes just a small fraction out of
 355 these events. The trigger system used for reducing the information stored, while leaving "interesting"
 356 events untouched. It covers a range of pseudorapidity up to 2.5.

357 The trigger system can be divided into 3 levels of selection:

358 **Level-1** The first level trigger should have a high operation speed, so it uses reduced-granularity in-
 359 formation form Resistive Plate Chambers (RPC) and Thin-Gap Chambers (TGC) and calorimeter
 360 systems. It searches for leptonic and hadronic signatures (or large total transverse energy) in
 361 the detector. This trigger allows to reduce a rate, that can be handled by a readout electronics
 362 (75 kHz).

363 **Level-2** The second level trigger analyses in more details Regions-of-Interest (RoI's) identified by
 364 Level-1 trigger. It uses an information on RoI's such as energy and a position of clusters to
 365 further reduce the data transferred. The Level-2 event rate is below 3.5 kHz, with processing
 366 time around 30 ms in average.

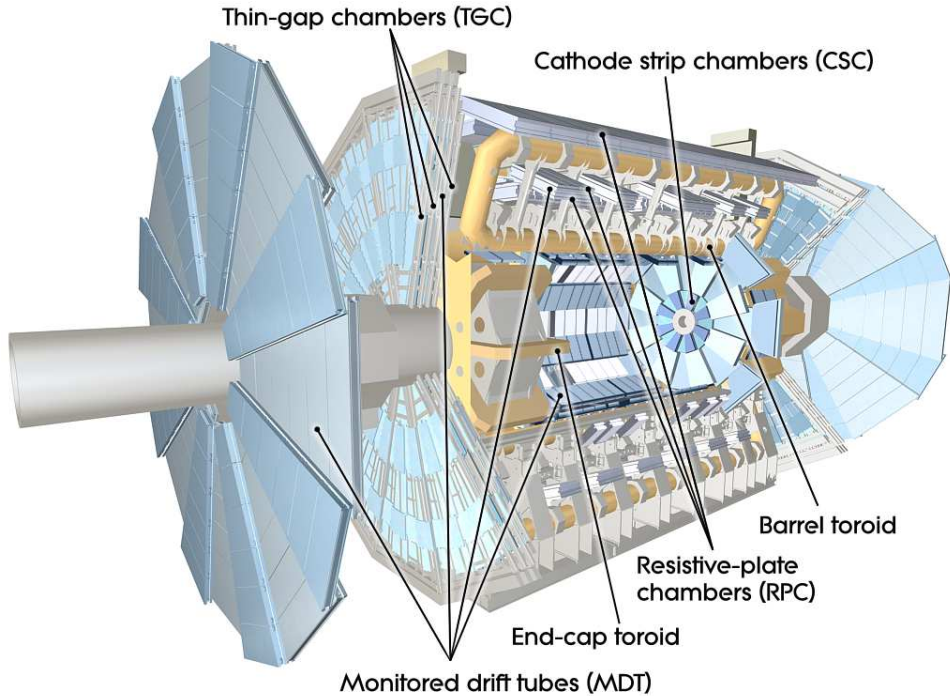


Fig. 4.8: Cut-away view of the ATLAS muon system. [3]

³⁶⁷ **High-Level Trigger (HLT)** The last level selection is performed offline on large farm of CPUs. It anal-
³⁶⁸ yses a full information from detectors to refine a trigger selections. The additional information
³⁶⁹ from tracking allows to improve particle identification and distinguish electrons and photons.
³⁷⁰ About 200 events per second are left after the HLT and transmitted to the permanent storage.

³⁷¹ The data acquisition system (DAQ) receives information from the readout electronics at the L1
³⁷² trigger rate and transfers the data to L2. After passing the L2 selection criteria the event is build
³⁷³ and transmitted to HLT.

³⁷⁴ 4.3 Luminosity measurement

One of the main components, characterizing the collider is the instantaneous luminosity $\mathcal{L}(t)$ delivered, that is defined as a proportional factor between the cross-section σ_p and number of interactions per second $\frac{dR}{dt}$, as :

$$\frac{dR}{dt} = \mathcal{L}(t) \times \sigma_p (cm^{-2}s^{-1}). \quad (4.5)$$

³⁷⁵ This value is a relativistic invariant and independent on physical reaction.

In case of LHC, that performs head-on collisions of particle bunches, it could be calculated as per beam value:

$$\mathcal{L} = \frac{N_p^2 N_b f_{\text{rev}}}{4\pi \sigma_x \sigma_y} F, \quad (4.6)$$

³⁷⁶ where N_p is the number of protons per beam, N_b - number of bunches, f_{rev} is the revolution
³⁷⁷ frequency, σ_x and σ_y are the horizontal and vertical beam profile widths. The factor F is coming from

378 the beam crossing angle. In 2012, at 8 TeV centre-of-mass energy, the LHC machine was able to
379 reach an instantaneous luminosity $7.7 \times 10^{33} [cm^{-2}s^{-1}]$.

380 The ATLAS experiment uses several detectors to measure the recorded luminosity. The Beam
381 Condition Monitor (BCM) monitors a beam parameters close to the interaction point and allows to
382 measure bunch intensities. In the forward region a special detector for a luminosity measurements is
383 placed: the LUCID (LUminosity measurement using Cerenkov Integrating Detector) detector. It detects
384 the inelastic scattering.

Chapter 5

386 Event reconstruction

389	5.1 Tracks and vertexes	27
390	5.2 Electron reconstruction and identification	28
391	5.2.1 Central electrons reconstruction	28
392	5.2.2 Forward electrons reconstruction	28
393	5.2.3 Electron identification	29
394	5.3 Muon reconstruction and identification	29
395	5.4 Missing transverse energy reconstruction	30
396	5.4.1 Standard missing transverse energy reconstruction	30
397	5.4.2 Reconstruction of missing transverse energy from hadronic recoil	31

401 The raw detector information could not be used in the physics analysis. It is required to have a
 402 separate process of interpretation of electronics signals, called reconstruction. It is used to determine
 403 the particles, born in the collision, their momentia, direction and vertexes, they are coming from. In
 404 this chapter the reconstruction and identification of the objects at ATLAS experiment, used in the
 405 analysis will be described.

406 It should be noted, that the missing transverse energy reconstruction stands separately, since
 407 the standard procedure was not applicable for 2.76 TeV data and a different approach have been
 408 adapted.

409 5.1 Tracks and vertexes

410 The tracks are reconstructed from the ID information. The reconstruction can be divided into 2
 411 steps. On the first step the inside-out algorithm is used for the pixel and silicon detector. Tracks are
 412 reconstructed from the random 3-points seed in the detector and then adds the new points, while
 413 moving to the interaction point using the Kalman filter. The Kalman filter is the iterative algorithm
 414 that provides the best estimate based on projection of previous and current measurement. Ambiguities
 415 in the track candidates are resolved and tracks are extended in TRT.

416 At the second step, algorithm searches for the segments, reconstructed in TRT and then extends
 417 them into the silicon detector. The tracks in TRT with no silicon extension are referred as TRT-
 418 standalone tracks.

419 Vertexes are reconstructed using the iterative vertex finding algorithm. The vertex starts from
 420 the z-position at the beamline of one of the tracks. The χ^2 fit is performed on that seed and

421 nearby tracks. The tracks, that are displaced for more, than 7σ are treated as a separate vertex.
422 The procedure is repeated till no new vertexes are found. During the reconstruction vertexes are
423 required to contain at least 2 tracks, but the requirement of the 3 tracks could give more robustness.
424 From the vertex candidates, the vertex with highest sum of the transverse momenta of the outgoing
425 tracks is defined as a primary vertex.

426 5.2 Electron reconstruction and identification

427 Due to the detector design electrons are divided into the 2 groups: central and forward. For the
428 central electrons ($|\eta| < 2.5$) there is a tracking information available. Presence of the ID track allows
429 to perform the precise reconstruction and identification. On another hand, for the forward ($|\eta| > 2.5$
430) electrons could be reconstructed using just the calorimeter information, so the different algorithm
431 is used. In this section the identification of the central electrons and reconstruction for both central
432 and forward electrons will be discussed.

433 5.2.1 Central electrons reconstruction

434 The central electron reconstruction starts from the clusters in the EM calorimeter. On the first step
435 the calorimeter is divided by the grid with the cell size $\Delta\eta \times \Delta\phi = 0.25 \times 0.25$. The EM calorimeter
436 clusters are formed from the cells with total transverse energy in all layers above 2.5 GeV using the
437 sliding window algorithm with size 3×5 cells. The position of the cluster is determined from its
438 barycenter.

439 On the second step track with $P_T > 0.5$ GeV are extrapolated to the middle layer of the EM
440 calorimeter. A track and a cluster are considered matched to each other if the distance between
441 track and cluster is $|\Delta\eta| < 0.5$ GeV. In order to take into account effect of the bremsstrahlung losses
442 the azimuthal distance is allowed within $\Delta\phi < 0.1$ on the side where the extrapolated track bends as
443 it traverses the solenoidal magnetic field.

444 An electron is considered to be reconstructed if at least 1 track is matched to EM cluster. In case if
445 there are several tracks passing the requirements, the tracks with silicon hits are given the priority,
446 an the match with the smallest distance $\Delta R = \sqrt{\Delta\eta^2 + \Delta\phi^2}$. In case if there is no track matched,
447 the cluster is treated as a photon candidate.

448 After the track matching the cluster size is optimised. The cluster size is enlarged to 3×7 and
449 5×5 in barrel and end-cap EM respectively. The total reconstructed electron energy is determined
450 from the corrected cluster energy, estimated energy deposit in the material in front of EM and
451 the estimated energy deposits outside of the cluster and calorimeter. The absolute energy scale
452 determination is described in Sec.??

453 5.2.2 Forward electrons reconstruction

454 Since there is no tracking in the forward region ($2.5 < |\eta| < 4.9$), the electron could be reconstructed
455 using just the information from EMEC and FCAL detectors. Opposite to the central electrons with
456 fixed size of the cell, for forward electrons the topological clustering algorithm is used [4]. The
457 main principle of this algorithm is that cells with energy higher than expected noise, are merged
458 together iteratively. The average noise in the cell is obtained in the calibration runs and includes a
459 contribution from pile-up. The cluster starts from the cell with significant energy and then expanded
460 by neighborhood cells. If 2 clusters are sharing 1 neighborhood cell, they are merged together. The

461 threshold, defined as $t = \frac{E_{cell}}{E_{noise}}$, is 4 and 2 for the starting the cell and expanding neighborhood
462 respectively.

463 The energy of the electrons is defined as the sum of the energies, taking into account for energy
464 losses in passive material in front of calorimeter. The direction of the electron is defined as the
465 barycentre of the cluster cells.

466 5.2.3 Electron identification

467 The application of additional criteria on reconstructed electrons allows to get better purity of the
468 sample and exlude objects, that can be misidentified as electrons, such as: jets and electrons from
469 the photon conversion.

470 The identification of the central electron is based on a sequential cuts, on calorimeter infromation,
471 tracking and combined variables. There are 3 sets of selection criteria, used for a physics analyses,
472 designed in hierarchical way at to provide incresied background rejection with cost of decreasing
473 identification efficiency. They are:

474 **Loose** The loose identification criteria uses the shower shape variables in first and second layer of
475 EM calorimeter and the fraction of energy, deposited in hadronic calorimeter. There are also
476 additional requirements on electron track and track-cluster matching.

477 **Medium** The medium selection is made out of loose identification with adding the information from
478 the 3-rd level of EM calorimeter, transverse impact parameter d_0 and TRT (to reject charged
479 hadron background) if available. Additionally the measured hit in the innermost layer of pixel
480 is required to discriminate against the photon conversions. These requirements are allowing to
481 increase the background-rejection power by an order of magnitude, compared to loose.

482 **Tight** The tight selection uses the full information of the particle identification tools available. In
483 addition to medium criteria, it puts stricter requirements on track quality, on ration of EM
484 cluster energy to the track momentum and veto on reconstructed photon conversion vertices
485 assosiated with the cluster. The overall strength of background rejection is 2 times higher, that
486 for a medium selection.

487 It should be noted, that neither of these criteria requires no additional tracks close to the identi-
488 fied electrons. The optimization of these requirements (called isolation requirements) is left for the
489 dedicated analysis.

490 5.3 Muon reconstruction and identification

491 The ATLAS experiment uses the information from ID and muon spectrometer for a precise re-
492 construction of the muons. Energy measurments in calorimeter can also be used for the muon
493 identification. The muons, based on the information, available from these detectors, can be divided
494 into different types:

495 **Combined (CB)** Muons with track both in ID and MS, that could be matched to each other. This is
496 the main type of the muons.

497 **Segment-tagged (ST)** Muons with track in the ID and at least one local track segment in the MDT
498 or CSC chambers. This type of muons could be used for the small P_T muons or in the reduced
499 MS acceptance region.

500 **Stand-Alone (SA)** These are the muons, that are crossing at least 2 layers of MS chambers, but
 501 have no reconstructed track in the ID. The parameters of the track are determined using the
 502 extrapolation to the primary vertex, taking into account the estimated energy loss in the
 503 detector in front of MS. These muons are mainly used to extend the acceptance up to $|\eta| < 2.7$,
 504 where there is no ID information.

505 **Calorimeter-tagged (CaloTag)** Muons, that have a track in the calorimeter, that can be associated
 506 with the minimum ionizing particle.

507 The muons are reconstructed in MS in two steps: first the local segments within one layer are
 508 combined and then the segments are combined in a full track. The reconstruction of
 509 the MS and combined ID-MS track can be done using one of the two independent reconstruction
 510 procedures [5], called Staco and Muid.

511 The Muid algorithm performs full track refit using the parameters from ID and MS [6]. For the staco
 512 algorithm the reconstruction of the track in MS starts from the segment from the outers station.
 513 The segments from middle and inner layers are iteratively added till the full track is obtained. The
 514 matching between ID and MS sub-detectors performed via statistical combination of the parameters
 515 in ID and MS using the corresponding covariance matrices [7]. Staco algorithm is the algorithm, used
 516 in this analysis.

517 The following additional requirements are applied on ID track for the muons:

- 518 • at least 1 pixel hit
- 519 • at least 2 SCT hits
- 520 • at most 2 active pixel or SCT hits, that are transversed by the track, but have no hit.
- 521 • in the region of full TRT acceptance ($0.1 < |\eta| < 1.9$) at least 9 TRT hits.

522 5.4 Missing transverse energy reconstruction

523 ATLAS detector has almost 4π coverage. This allows to calculate imbalance of energies inside
 524 calorimeter, especially transversal part of it called E_T^{miss} . In W-analyses E_T^{miss} is used as a proxy
 525 for neutrino from a $W \rightarrow l\nu$ decay. It leaves detector without interacting with it and that causes
 526 large energy imbalance in an eventA. In this section two methods of E_T^{miss} reconstruction and the
 527 reasons for using non-standard one will be discussed.

528 5.4.1 Standard missing transverse energy reconstruction

Standard reconstruction of E_T^{miss} at ATLAS experiment [8] uses transverse energy deposits in the
 calorimeter, energy losses in cryostat and reconstructed muons for a calculation:

$$E_{x(y)}^{\text{miss}} = E_{x(y)}^{\text{miss,calo}} + E_{x(y)}^{\text{miss,cryo}} + E_{x(y)}^{\text{miss,muon}}. \quad (5.1)$$

The calorimeter term is using information from reconstructed physics objects for calibration of
 the cell response. The total transverse energy in calorimeter is defined as:

$$E_{x(y)}^{\text{miss}} = E_{x(y)}^{\text{miss},e} + E_{x(y)}^{\text{miss},\gamma} + E_{x(y)}^{\text{miss},\tau} + E_{x(y)}^{\text{miss,jets}} + E_{x(y)}^{\text{miss,SoftTerm}} + E_{x(y)}^{\text{miss},\mu}. \quad (5.2)$$

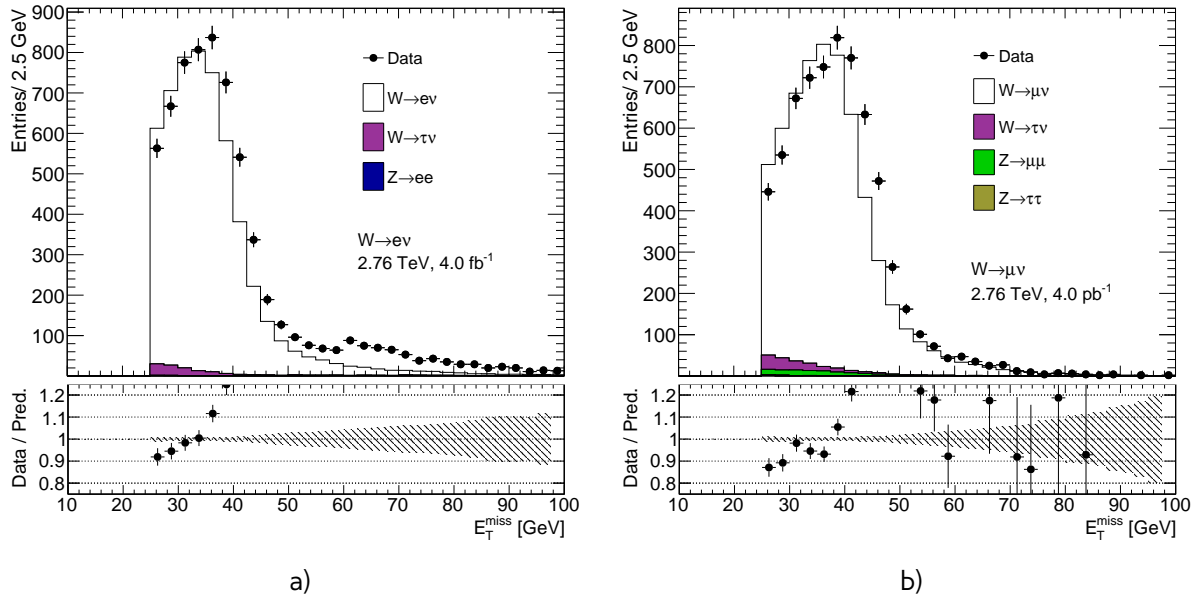


Fig. 5.1: Missing transverse energy distribution for a) the $W \rightarrow e\nu$ selection and b) the $W \rightarrow \mu\nu$ selection from Chap. 9. E_T^{miss} calculated using the standard ATLAS algorithm. The expected contributions from all backgrounds are estimated with Monte Carlo simulations, except for QCD background that is not included. All Monte-Carlo corrections from Chap. 10 are applied. There are visible discrepancies between data and MC, that cannot be explained by the contribution of the QCD background, which is expected mainly in the low E_T^{miss} region (Sec. 12.1).

529 where each term is calculated as a negative sum of the calibrated reconstructed objects, projected
 530 onto the x and y directions. Each jet with energy $P_T > 20$ GeV is corrected for a pile-up and a jet
 531 energy scale is applied. Soft term is calculated from topoclusters and tracks, that are not associated
 532 with high-pt objects. To avoid double counting, muon energy loss in the calorimeter is subtracted
 533 from E_T^{miss} . The E_T^{miss} muon term is calculated from the momenta of muons measured in a range
 534 of pseudorapidity $|\eta| < 2.7$. Since pileup has a significant effect on the E_T^{miss} performance several
 535 methods of pileup suppression are used [9].

536 The runs at 2.76 TeV are characterized by a low pileup (mean number of interaction per bunch
 537 crossing < 1.0), so the usage of a procedure optimized for high pileup 8 TeV runs may not be optimal.
 538 It was examined and found out, that there are big discrepancies between the E_T^{miss} distributions for
 539 data and MC simulation, as shown in Fig. 5.1, where the missing transverse energy for data is
 540 compared to signal and background MC predictions.

541 The differences are visible in both electron and muon channels and cannot be explained by the
 542 (missing on the control plots) contribution from the QCD background, which is expected mainly in
 543 the low E_T^{miss} region (see Sec. 12.1).

544 5.4.2 Reconstruction of missing transverse energy from hadronic recoil

A different way of E_T^{miss} calculation was developed for W and Z decays by the W mass measurements group [11]. This procedure is based on a requirement of a balance in the transverse momentum of a

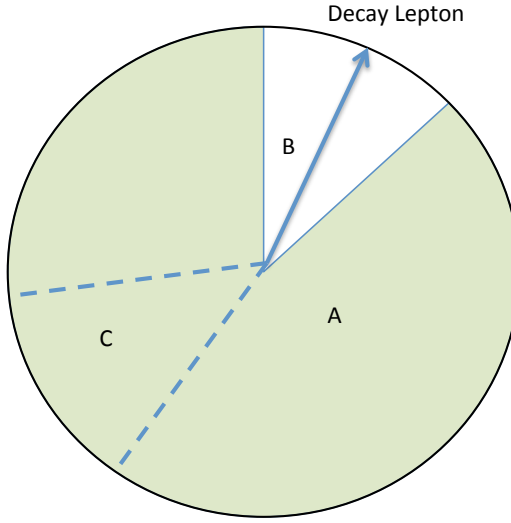


Fig. 5.2: Definition of different zones in the calculation of the cluster-based hadronic recoil. Zone B is excluded from hadronic recoil calculation because it contains decay lepton. To describe properly the overall acitivity it is replaced by the zone C, rotated in the direction of B. Zone A corresponds to the rest of the calorimeter [10].

W-boson and the initial (quark-gluon) state radiation:

$$\vec{P}_T^W = \vec{P}_T^l + \vec{P}_T^\nu = \sum \vec{P}_T^{ISRquarks,gluon}, \quad (5.3)$$

where $\sum \vec{P}_T^{ISRquarks,gluon}$ is a transverse momentum of partons from the initial state radiation, also called hadronic recoil (HR), \vec{P}_T^l and \vec{P}_T^ν are the transverse momenta of lepton and neutrino respectively. Therefore, E_T^{miss} can be determined as:

$$E_T^{miss} = -P_T^\nu = -HR + P_T^l \quad (5.4)$$

This procedure assumes, that recoil arises from one single leading jet, and the rest is coming from a soft hadronic activity. The hadronic recoil is computed as a vector sum of calorimeter clusters:

$$HR = \sum_{i=0}^{N_{topo}} \vec{p}_T^{topo} \quad (5.5)$$

while a scalar sum of all transverse energy contributions corresponds to the hadronic activity in the event:

$$\sum E_T = \sum_{i=0}^{N_{topo}} E_T^{topo} \quad (5.6)$$

⁵⁴⁵ To avoid double counting of lepton energy losses in the calorimeter, the clusters inside a cone with
⁵⁴⁶ a radius $dR = 0.2$ around the lepton direction are excluded from this calculation. To compensate
⁵⁴⁷ for the subtracted soft activity from the cone, a replacement cone is added (Fig. 5.2). This cone is

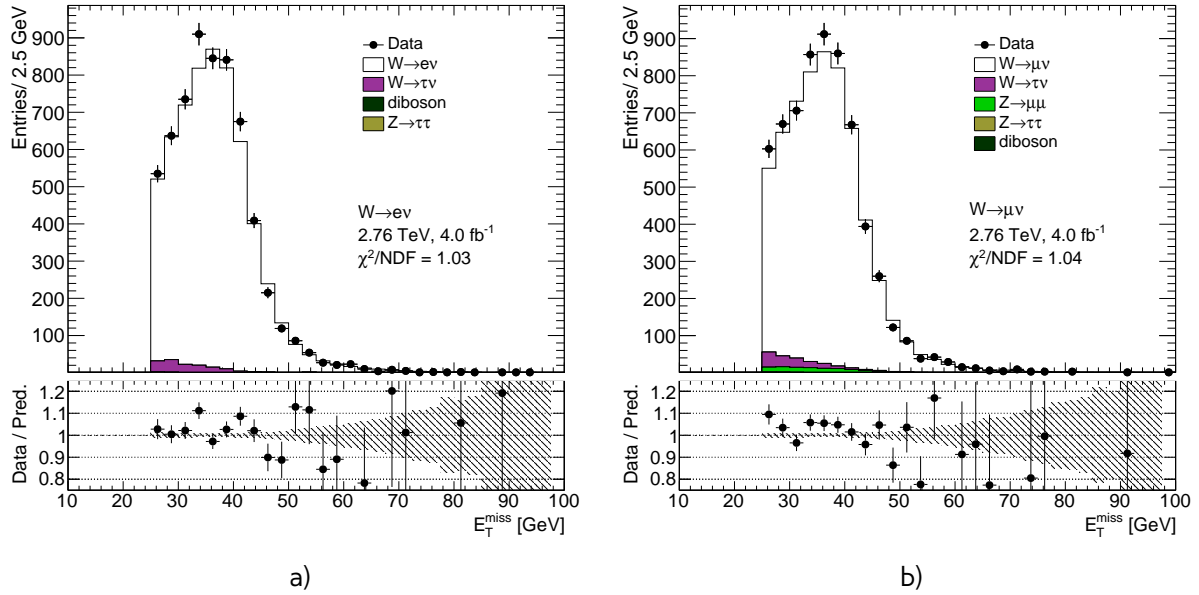


Fig. 5.3: Missing transverse energy distribution for a) the $W \rightarrow e\nu$ selection and b) the $W \rightarrow \mu\nu$ selection from Chap. 9. E_T^{miss} calculated using the hadronic recoil algorithm. The expected contributions from all backgrounds are estimated with Monte Carlo simulations, except for QCD background that is not included. All Monte-Carlo corrections from Chap. 10 are applied.

548 defined as a cone at the same pseudorapidity, but at a different ϕ . It should be far from any other
 549 lepton and hadronic recoil direction. The cone is then rotated to the original lepton direction. This
 550 definition does not take into account the jet reconstruction aspects.

551 Fig. 5.3 shows the control plots for the distributions of missing transverse energy calculated using
 552 the hadronic recoil procedure. In both electron and muon channels the agreement between data and
 553 MC simulation is much better than in the case of the standard procedure described in a previous
 554 chapter. It was desired to use hadronic recoil E_T^{miss} reconstruction method in 2.76 TeV data analysis.

556 Monte-Carlo simulation

557 The Monte Carlo (MC) method was invented by scientists working on the atomic bomb in the 1940s.
 558 Its core idea is to use random samples of parameters or inputs to explore the behavior of a complex
 559 system or process. Nowadays, MC experiments are essential part of research in both theoretical and
 560 experimental particle physics. This chapter gives an overview of the ATLAS experiment simulation
 561 scheme, the simulation methods and the software used. Also, techniques for fast simulation will be
 562 discussed.

563 6.1 ATLAS chain of Monte-Carlo production

564 Monte Carlo method allows to perform different analyses, generate predictions for comparisons
 565 with data, study the detector or the selection algorithms performance. All of these applications
 566 require accurate MC predictions. The simulation software implements precise physics models and
 567 uses statistics large enough, to exclude statistical uncertainties (usually 5 times more, than expected
 568 in a data). ATLAS simulation software is integrated into Athena framework.

569 Simulation chain is generally divided into 4 main steps (Figure 6.1):

570 **Event generation** Simulation of hard interaction, parton evolution and hadronisation. This step is
 571 independent of the ATLAS detector geometry.

572 **Simulation** Simulation of energy depositions ("hits") which are produced by final state particles.

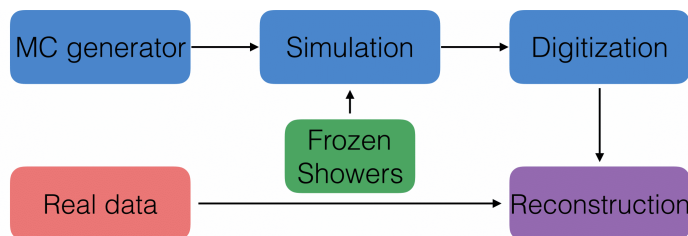


Fig. 6.1: Diagram of the ATLAS MC production chain. Stages in blue are completely related to Monte-Carlo production. The Frozen Showers technique for fast simulation will be explained in Chap. 7. Data sample collection is described in Sec. 4.2. Reconstruction is common stage for data and MC and described in Chap. 5. After the reconstruction events are going to the analysis chain.

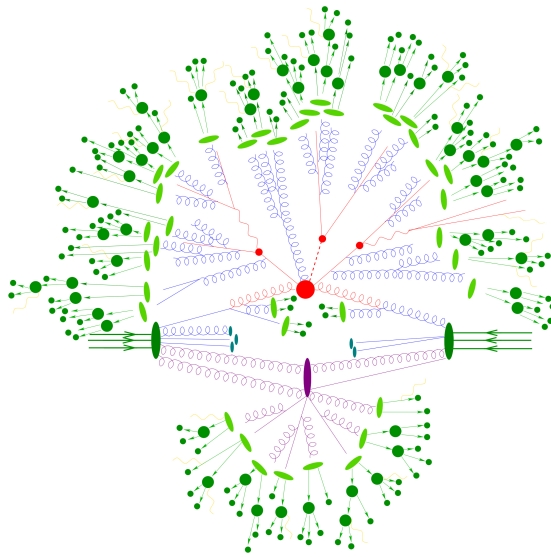


Fig. 6.2: Schematic view of a $t\bar{t}H$ event produced in a pp-collision: the hard scattering is shown as a red blob with the solid and dashed lines as the resulting three particles. Independently happening multi-particle interactions are indicated by the violet blob. Parton showers are shown with curly lines. Hadronization yields hadrons as shown in light green, while the final state particle are dark green. [12]

573 **Digitalization** Simulation of detector response using "hits" information: first inputs to the read out
 574 drivers (ROD's), called "digits" are constructed, then ROD functionality is emulated. Detector
 575 noise effects are added at this stage.

576 **Reconstruction** Production of the Analysis Object Data (AOD) files, which are containing the information needed for physics analysis. This stage is identical for both data and MC

578 Additionally, the pileup effects are added to MC by overlaying the simulation of the hard interactions
 579 with the simulation of soft inelastic scatterings. This scheme allows to use computing resources more
 580 efficiently, than with a single-step simulation and simplifies software validation, since it is possible
 581 to reuse files from previous stages. In the following sections event generation and simulation will be
 582 described in more details.

583 6.2 Event generators

584 The outcome of the hard interaction could be a simple scattering of the hadron elementary constituents, their annihilation into new resonances or a combination of two. This can lead to a final
 585 state with a large particle multiplicity. The main goal of the event generator is to provide a complete
 586 picture of the final state: description of the particle types and momenta on the event-by-event
 587 basis. The factorisation theorem [13] allows to make event generation in independent stages, which
 588 are dominated by different dynamics. Schematic plan of simulation of a $t\bar{t}H$ event is shown in Figure
 589 6.2:

591 **Modelling of hard subprocess** Hard subprocess happens at the smallest times and distances,
 592 where the colliding partons are considered free. The process of interest is simulated by select-

593 ing production channels and calculating corresponding matrix elements (ME) at a fixed order
594 of the strong coupling constant and including randomly chosen momenta of the incoming par-
595 tons, which are based on the parton distribution functions (PDF). Most of the generators have
596 leading (LO) order or next to leading order (NLO) in α_s .

597 **Parton showering** Quarks and gluons from hard process can radiate secondary quarks and gluons,
598 resulting in dozens of additional partons associated with the event. This process is calculated
599 as step-by-step evolution of momentum transfer scales from highest (hard subprocess), to the
600 lowest (around 1 GeV), where the perturbative calculations are not valid. There is a possibility of
601 double counting between showers and hard subprocess. This can be avoided using matching
602 approaches, for which higher order corrections to ME are integrated with parton showers, or
603 merging strategy, there jet resolution scale is used as an threshold between matrix elements
604 and parton showers.

605 **Hadronisation** Final, stable, color-neutral particles, which can be detected in an experiment, are
606 formed during hadronisation. This occurs at larger nonperturbative scales and is usually im-
607 plemented using different phenomenological models.

608 **Modelling underlying event** Parallel to the main process other collisions of partons can occur. They
609 are called underlying event. These additional interactions can produce partons which contribute
610 to the final state. This is one of the least understood aspect of hadronic collisions.

611 The current analysis uses samples generated with the following generators:

612 **Powheg** [14] Powheg is Monte-Carlo, which calculates the matrix element (ME) at the NLO level [15],
613 that can be interfaced to other generators (such as Pythia or Herwig) to get higher precision
614 of showering.

615 **Pythia** [16] Pythia is a general purpose generator for hadronic, hadron-lepton and leptonic collisions.
616 It can model ME, initial and final state showers, hadronisation and decays, underlying event
617 (via multi parton interactions). Pythia contains library with around 240 processes with LO ME.
618 It uses Lund String model [17] for hadronisation.

619 **Herwig** [18] Herwig is a LO general purpose event generator for simulation of lepton-lepton, hadron-
620 lepton and hadron-hadron collisions. The main difference between Pythia and Herwig is that
621 Herwig uses angular ordering in the parton showers and models the hadronisation step using
622 the cluster fragmentation

623 **Sherpa** [19] Sherpa is an event generator, that uses tree-level leading order matrix element for a hard
624 scattering and features its own implementation of parton shower and hadronisation models.

625 **Photos** [20] Photos is a program used for generation of QED radiative corrections. It is linked to
626 multipurpose generators.

627 **Tauola** [21] Tauola is a generator, used to describe leptonic and semi-leptonic τ -decays. It is also
628 linked to multipurpose generators.

6.3 Simulation in Geant4

After event generation, simulation software is used to provide hardware response for final state particles. The main method used by ATLAS experiment, referred to as *Full Simulation*, makes use of the Geant4 [22]. Geant4 is C++ based toolkit for the simulation of the passage of particles through matter. It is used in a wide range of experiments in high energy and nuclear physics.

Geant4 can simulate complex detector structures with sensitive detector material and corresponding infrastructure. It can also calculate basic properties of materials, like radiation and interaction length. Geant4 stores "hits" information - snapshots of physical interactions. In Geant4 events and particles are simulated separately and each particle is moved in steps. Size of each step is chosen to preserve both CPU performance and required precision.

Physics interactions are treated as a set of discrete processes. They could be handled either for particle at rest, or its along step, the maximum value of which depends on physics process, or after it. Geant4 package has different models and approximations for hadronic and electromagnetic processes. Some of them are approximate and computationally fast. It allows to choose a set of the models, called physics list, depending on particular requirements. There are several reference physics lists, that are validated for each new release of Geant4 software. ATLAS experiment uses one of these lists.

Most of the computing resources are taken by a mass MC production, required for each data taking periods. Uncertainties of some of Run-I analyses are dominated by available MC statistics. It is possible to improve in CPU usage by tuning physics list or replacing a complex magnetic field maps by a parametrisation. Also there are long-term developments for multi-threading and vectorisation of the code.

Run-2 has a higher pileup and luminosity, so even more MC events are needed. This means that fast and accurate simulation approach is essential. During the simulation largest time is spent on calorimeters. This is the motivation for development of fast calorimetry techniques.

There are two main methods used at ATLAS:

- Parametrisation of the calorimeter cells response. Spacial energy response is simulated using longitudinal and lateral energy profiles.
- Frozen Showers. This technique will be described in more detailed in Chap. 7

659

Frozen Showers

660	661	7.1	Introduction	40
662	663	7.2	Generation and use in simulation	45
664	665	7.2.1	Libraries tuning	45
666	667	7.3	Machine learning based bin finding procedure	47
668	669	7.3.1	Machine learning introduction	47
670	671	7.3.2	Model description	49
672	673	7.3.3	Interpretation of results	51
674	675	7.3.4	Reconstructed electron energy	53
676	677	7.3.5	Plans for the future	54
678	679	7.4	Validation of the new libraries	57

675 As it was mentioned in the previous chapter, fast simulation techniques are the essential part of
 676 the Monte-Carlo production at the ATLAS experiment. A typical time needed for a simulation of $t\bar{t}$
 677 event is around 1 minute, and most it is spent on a simulation of particle interaction in calorimeters.
 678 This motivates a development of fast calorimetry techniques, allowing to describe calorimeter
 679 response.

680 Frozen showers is currently the main fast calorimeter simulation approach used at ATLAS experiment.
 681 In this chapter we will discuss main principles,difficulties and current developments in this
 682 method.

683 Frozen shower method uses pre-simulated "frozen" showers. This allows to reduce the time spent
 684 on a simulation of a large amount of low energy sub showers. This method gives a 25% speedup in
 685 simulation. It is required to have in advance generated libraries for each detector and particle used in
 686 this method. For each shower in the library its lateral and transverse size and a list of the all energy
 687 deposition inside the sensitive material (hits) with information about their energy, position and time
 688 are stored. During the simulation, if energy of a secondary electron falls below cutoff energy it is

Table 7.1: Main parameters used for the frozen shower libraries

The general frozen showers parameters	
Detectors used	FCAL1, FCAL2
Type of the particle	photons, electrons, neutrons
Energy range	$E_\gamma < 10 \text{ MeV}$, $E_e < 1000 \text{ MeV}$, $T_n < 100 \text{ MeV}$

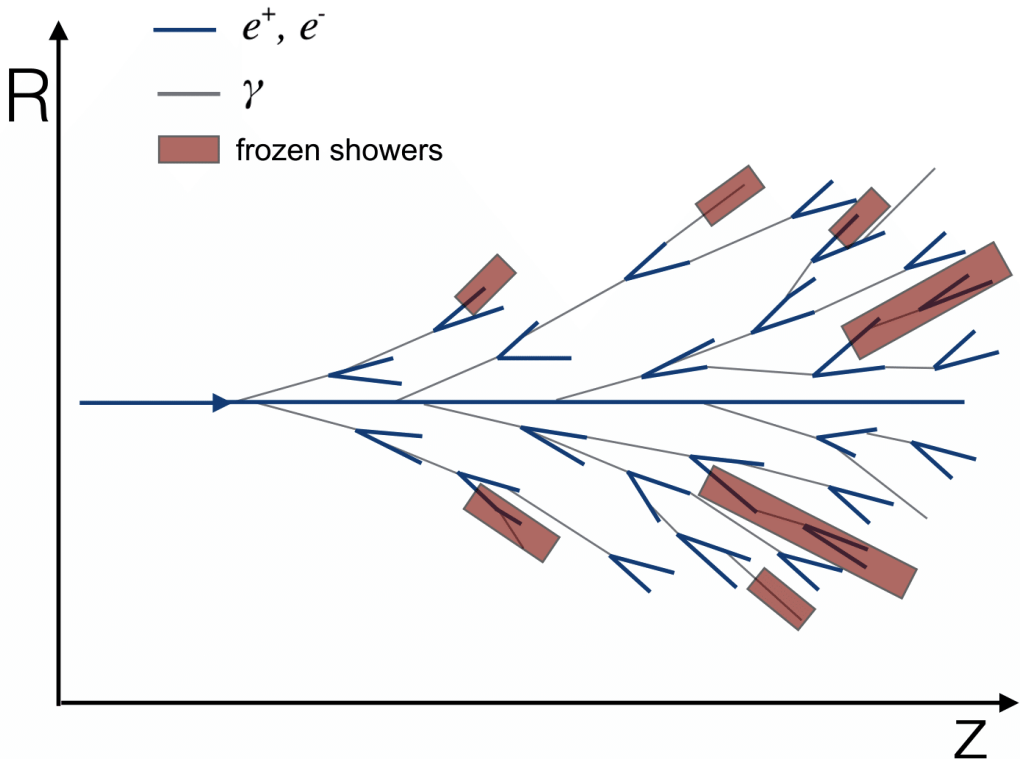


Fig. 7.1: Diagram showing the shower substitution of the low-energy particle, during the high-energy particle simulation. Some of the showers from a particles, substituted by frozen showers method marked by a red squares

replaced by a shower from a library, as shown in Fig. 7.1. Main parameters used in ATLAS simulation are summarized in a Tab. 7.1, where FCAL1 and FCAL2 are the first two forward calorimeters (see Sec. 4.2.3) and $E_\gamma < 10$, $E_e < 1000$, $T_n < 100$ are the maximum energies of photons, electrons and neutrons used in the method.

Since currently the Frozen Showers method is used only for FCAL, this chapter will fully concentrate on optimisation of Frozen Showers in forward calorimeter.

7.1 Introduction

The fast simulation of forward calorimeters (FCAL) is a complicated task due to its complex structure. As it was mentioned in Sec. 4.2.3 FCAL consists of hexagonal absorber cells with anode tube and cathod rod in the cell center and liquid argon in the gap between rod and tube. In order to simulate the resolution of high energy electrons, good fast simulation technique should take into account this feature of a large amount of non-uniformly distributed sensitive material.

The energy resolution of an electron inside the calorimeter can be written as:

$$\frac{\sigma}{E} \approx \frac{1}{\sqrt{E}} \oplus \frac{1}{E} \oplus const, \quad (7.1)$$

where symbol \oplus indicates a quadratic sum. The first term is a 'stochastic term', which includes intrinsic shower fluctuations, the second one takes into account readout noise effects and pile-up fluctuations.

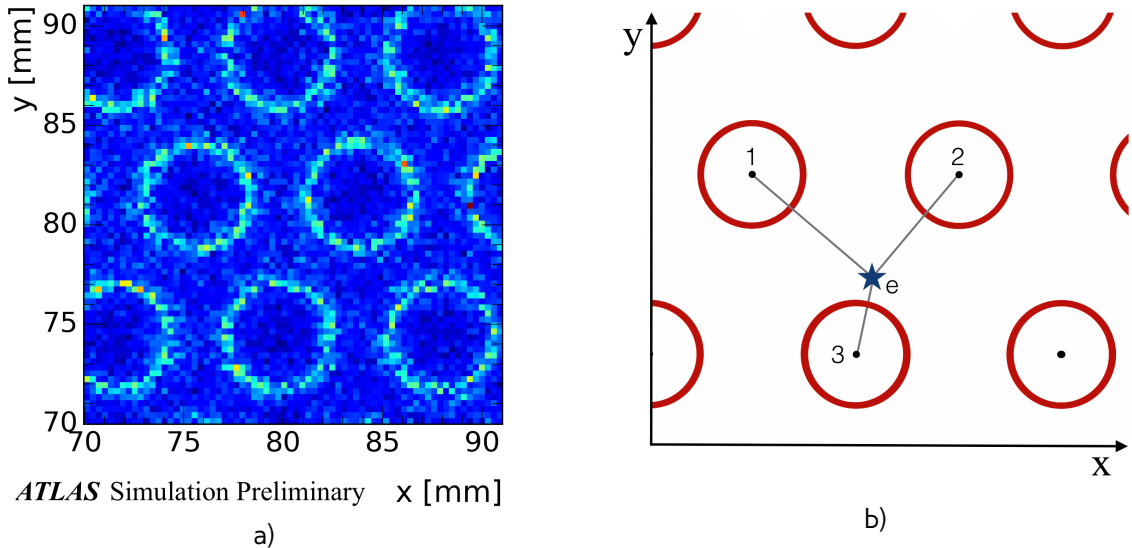


Fig. 7.2: a) Shower energy response histogram in the x vs y plane for electrons, generated with uniformly distributed x and y and energy less than 1 GeV. Light circles correspond to showers, started inside LAr gaps with on average higher energy response, while the dark parts correspond to dead material with smaller sum of the "hits" energy. b) Distance to a closest rod center scheme $d_{rod} = \min(d(1,e), d(2,e), d(3,e))$, where 1,2,3 are the positions of the rod centers and e is the position of initial electron.. Rod centers and liquid argon gaps are shown by black and red circles respectively.

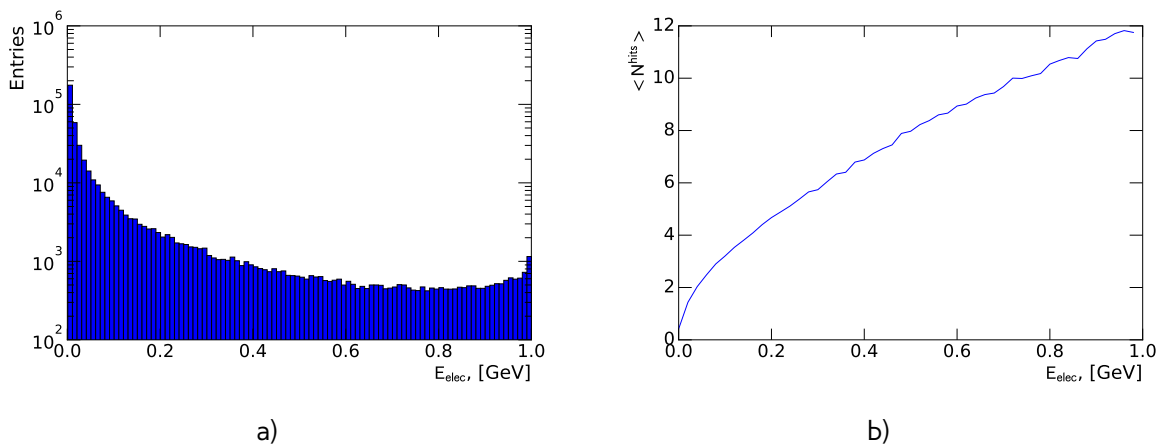


Fig. 7.3: Distribution of a) electron energies and b) mean number of hits in a shower vs energy of electron for electrons with energy less than 1 GeV coming from an initial electron with energy 1 TeV.

703 Constant term is connected to non-uniformities in a detector, causing large fluctuation of the energy
704 loss. The energy resolution of high-energy electrons is mostly dominated by the constant term.

Fluctuations due to the detector design are visible in a simulation of small energy electrons, generated at different points in forward calorimeter. Shower energy E^{shower} distribution in the x vs y plane is showed on Fig. 7.2 a). The shower energy is defined as:

$$E^{shower} = \sum E_i^{hits}, \quad (7.2)$$

705 where E_i^{hits} is an energy of i-th shower deposit inside the sensitive material. The periodic structure
706 resembles the calorimeter design, where the light circles correspond to gaps with liquid argon. It
707 could be reduced to a 1-d problem by introducing d_{rod} distance to the closest rod center, calculated
708 as shown on Fig. 7.2 b).

709 A typical electron substituted by a frozen shower coming from a simulation of high energy elec-
710 trons has a relatively small energy (Fig. 7.3 a)). A mean number of depositions in a sensitive material
711 in a "frozen" shower is around 5 and this value rises with electron energy (Fig. 7.3 b). Fig. 7.4
712 presents the distribution of the distance to a closest rod center vs shower energy for showers from
713 electrons with energy below 1 GeV coming from initial electrons with energy 1 TeV. The liquid argon
714 gap is marked by red lines. There is a clear difference in showers energies between electrons born
715 in a sensitive and dead materials. The differences in shower properties are also visible in a number
716 of hits (Fig. 7.5 a) and the standard deviation of energy of the hits in the shower (Fig. 7.5 b) distri-
717 butions. The size of these differences depends on electron energies and higher for smaller energies
718 (Fig. 7.6 a) and less significant for higher energies (Fig. 7.6 b). This fact combined with energy dis-
719 tribution states an importance of a proper simulation of non-uniformities for showers coming from
720 a small energy electrons.

721 On another hand, the use of the frozen showers in a small energy region can be suboptimal
722 because of the small number of energy depositions in a shower. For electrons with energy less than
723 30 MeV 90% of the showers have zero depositions and just 0.5% of showers have more than 1 hit
724 (Fig. 7.7). Below this energy single energy spot model has shown a better performance in simulation.

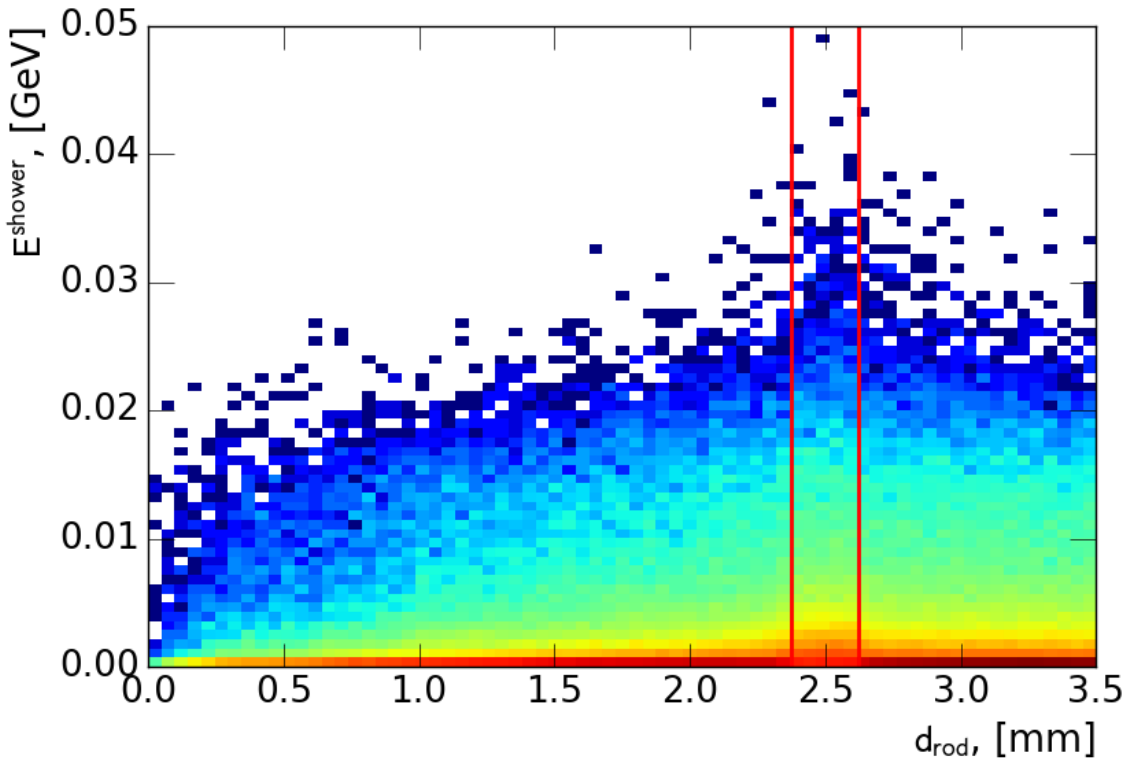


Fig. 7.4: Distribution of distance to a closest rod center vs shower energy for electron showers created by electrons with energy less than 1 GeV coming from initial electron with energy 1 TeV in distance to a closest rod center vs shower energy plane. Position of a liquid argon gap is noted by a red lines.

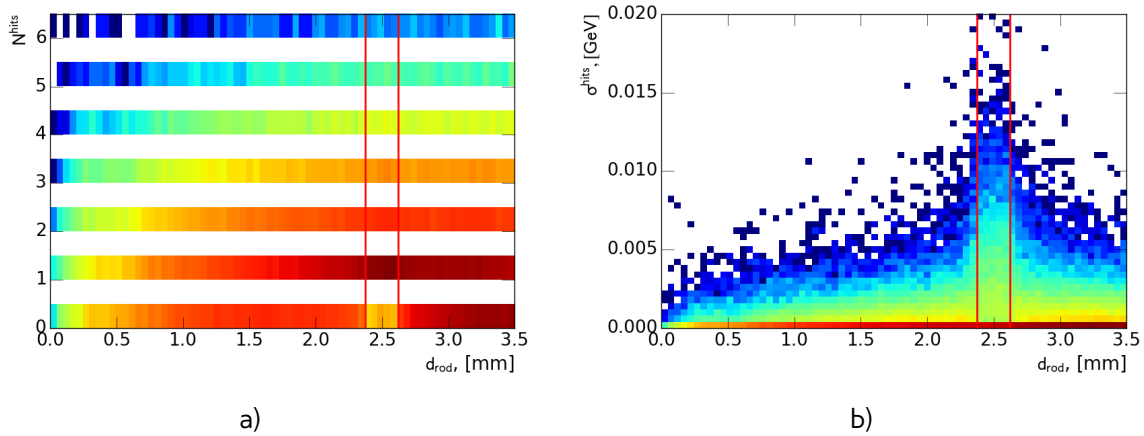


Fig. 7.5: Distribution of distance to a closest rod center vs a) number of hits in a shower plane and b) standard deviation of hits in a shower energy of electron showers created by electrons with energy less than 1 GeV coming from initial electron with energy 1 TeV. Position of a liquid argon gap is noted by a red lines.

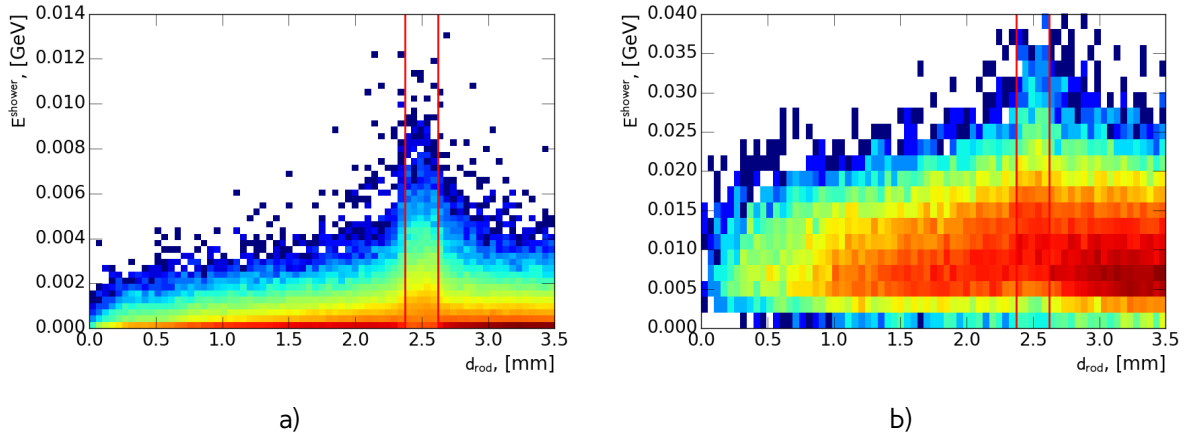


Fig. 7.6: Distribution of distance to a closest rod center vs shower energy for electron showers created by electrons with energy a) less than 100 MeV and b) higher than 300 GeV coming from initial electron with energy 1 TeV in plane. Position of a liquid argon gap is noted by red lines.

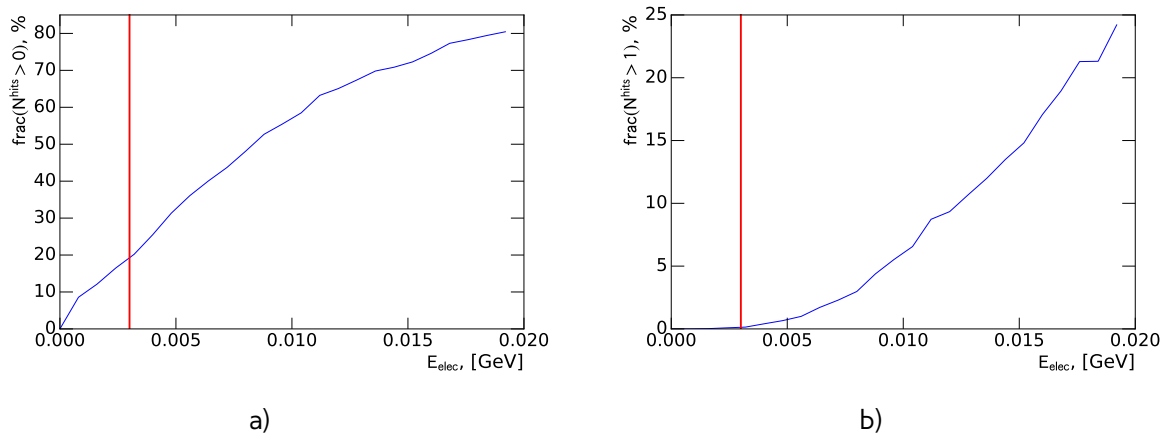


Fig. 7.7: Distribution of fraction of showers with a) at least 1 b) at least 2 depositions inside sensitive material depending on an initial electron energy. The red line denotes 30 MeV limit for a frozen showers method.

7.2 Generation and use in simulation

As it was mentioned in the introduction, the frozen showers method consist of 2 stages: generation of libraries and the use in simulation. Generation needs to be repeated for each significant change in the physics processes description in Geant4 or in a description of the detector. Showers are stored in a library in pseudorapidity and distance to a closest rod center bins, while energy remains unbinned. Distance binning was introduced to describe fluctuations from Sec. 7.1. The position of the liquid argon gap bin corresponds to the real gap position.

In order to have a proper energy distribution for generation of library particles coming from a simulation of physical process $t\bar{t}$ or high energy electrons are usually used. For each particle eligible for frozen showers use parameters are saved in a HepMC (reference) format for a later use. On a second stage, these particles are propagated through the calorimeter using standard ATLAS simulation infrastructure. Each hit is saved as a shower inside library in a corresponding pseudorapidity and distance bin.

Additionally, in order to save disc space as well as a memory consumption, the hit information is compressed. This compression is done in two steps:

Hit merging If the distance between any two hits is smaller, than a given parameter R_{min} , then hits are merged into one deposit at the energy weighted center of them. This process is done iteratively.

Truncation Hits which energies are below the fraction f of the total energy sum of all hits, are truncated. The energy of remaining hits is rescaled back to preserve the total deposited energy.

During simulation, if an energy of a particle falls below a cut-off energy, the particle algorithm examines resulting shower containment. It checks whether that particle is far from the edges of the calorimeter, so that the shower is by 90% inside the calorimeter. This depends also on an energy of the particle, because shower sizes are growing with energy. The algorithm searches for a shower with the closes energy in a corresponding pseudorapidity and distance bins. Shower is rotated in the direction of the particle. In order to correct the differences in the energy, each hit in a shower is scaled as:

$$E_{hit}^{new} = E_{hit} \cdot \frac{E_{part}}{E_{part,lib}}, \quad (7.3)$$

where E_{hit} is the energy of the hit, E_{part} is the energy of the particle and $E_{part,lib}$ is the energy of the particle from a library. Then particle is substituted by a resulting shower. Later, reconstruction algorithm uses hits from a frozen shower as a usual energy deposits in a sensitive material.

7.2.1 Libraries tuning

The good simulation method is required to be consistent with full simulation on all possible reconstructed objects. In case of Frozen Showers in forward calorimeter, the electron energy resolution is the most problematic value, since the resolution of the reconstructed electrons is around 2 times smaller (Fig. 7.8), than in a full simulation. It may be caused by a lack of the showers from liquid argon gap in a simulation. Most of this effect is coming from the electron libraries. This means that these libraries require additional reconstruction-based tuning after generation.

Usual tuning consists of 2-step manual procedure:

Changing bin width On this stage position of the liquid argon bin is moved, so what a bin width is enlarged. This causes a higher number of showers with higher response in simulation and

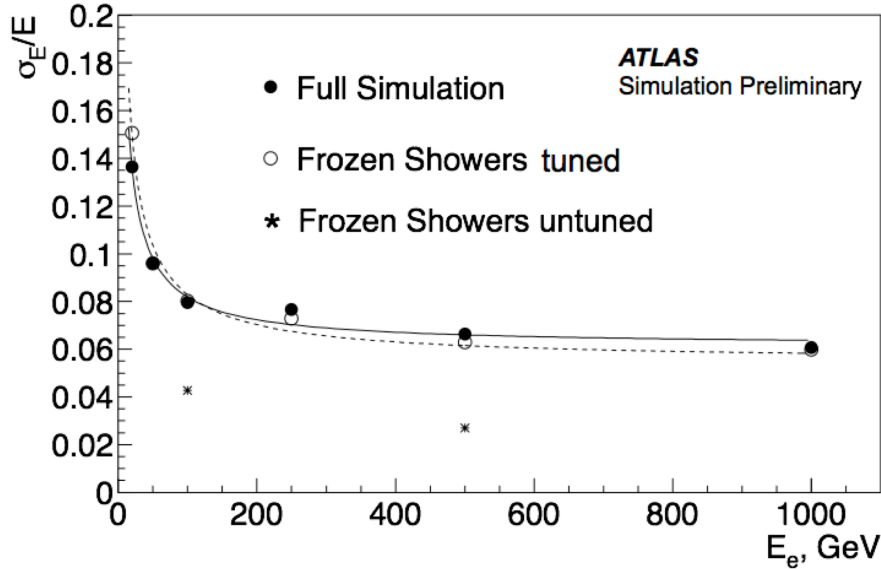


Fig. 7.8: Electron resolutions for full simulation(black dots), tuned(white circles) and untuned(star points) frozen showers. Electrons simulated with frozen showers libraries before tuning have twice smaller resolution, than an electrons from full simulation. Tuning allows to gain better agreement with full simulation.

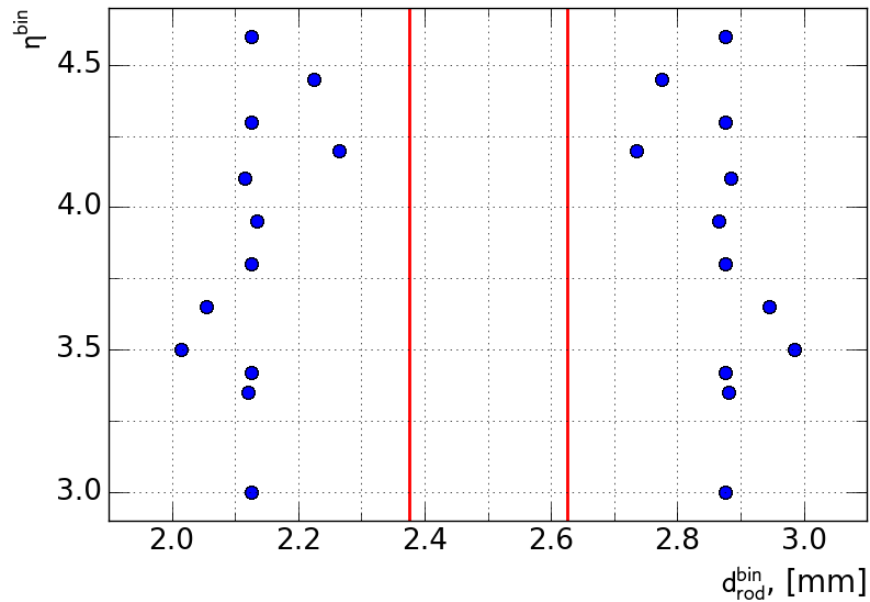


Fig. 7.9: Position of gap bins for different η bins in old libraries after tuning. Dots are corresponding to a limits of each bin. Red lines are denoting original position of bins, that are corresponding to a position of a liquid argon gap in the calorimeter.

758 therefore higher size of fluctuations. This leads to a higher resolution and a mean energy of
 759 reconstructed electrons.

760 **Shower energy scaling** In order to correct for the shift introduced in the mean energy, the shower
 761 energy is reduced by rescaling all the hits in a shower.

762 It is repeated iteratively in each pseudorapidity bin separately till the desired agreement is obtained.
 763 The resulting bin positions are shown on a Fig. 7.9. This method allows to have a relatively good agree-
 764 ment with full simulation (black dots on Fig. 7.8). However, it is necessary to repeat this procedure
 765 for each new library generation and requires significant tuning effort, that makes it not optimal.

766 7.3 Machine learning based bin finding procedure

767 Since frozen showers are planned to be used in Run-2 Monte-Carlo production, there is a need
 768 for a more automatic procedure of library generation with proper electrons resolution. One of the
 769 possible ways is to choose different position of liquid argon bin during libraries generation using
 770 machine learning tools. In this section automatic bin finding procedure will be discussed.

771 7.3.1 Machine learning introduction

772 Machine learning is a set of algorithms, which allows computers to learn and give predictions without
 773 being specifically programmed. This is a modern field of computer science, that is widely used in
 774 different fields like computer vision, natural language processing, data science etc. There are two
 775 main types of machine learning algorithms: supervised, where example of desired output is given by
 776 the "teacher" and the goal is to learn a general rule, that maps inputs to outputs and unsupervised
 777 learning, where no labels are given to the algorithm, and the algorithm discovers hidden patterns in
 778 the data. Initial data parameters of interest, that are used in algorithm to learn are called features.

779 Machine learning algorithms can be used for solving a classification problem, where each event
 780 should be identified to one of the specified classes. Since the first introduction of the machine
 781 learning classifiying algorithms called perceptron by Rosenblatt [\[ref\]](#) many different algorithms have
 782 been invented. In this analysis decision trees and support vector machines implemented in Scikit-
 783 Learn python package [\[reference\]](#) have been used.

784 Binary decision trees

785 Binary decision trees, called also single decision trees, are one of the most commonly used machine
 786 learning algorithms for a classification problems in particle physics. It can be represented as a set
 787 of sequential cuts on input variables. Scheme of this algorithm is shown in Fig. 7.10 a). Red circles
 788 show the nodes of the tree. Each node corresponds to the one of the internal input variables and
 789 connected to two branches, that are split in the respect to the a variable. The first node is called a
 790 root node. Depth of the tree is a number of edges from the node to the tree's root node. The tree
 791 ends with squares, called leaf nodes, where all events are classified to a certain class. Leaf node
 792 represents classification or decision. The tree, where each node has at most 2 children called binary
 793 decision tree.

The tree is build using the variable called Shannon entropy, what is similar to the entropy in physics:

$$S = - \sum_{i=1}^N p_i \log_2 p_i, \quad (7.4)$$

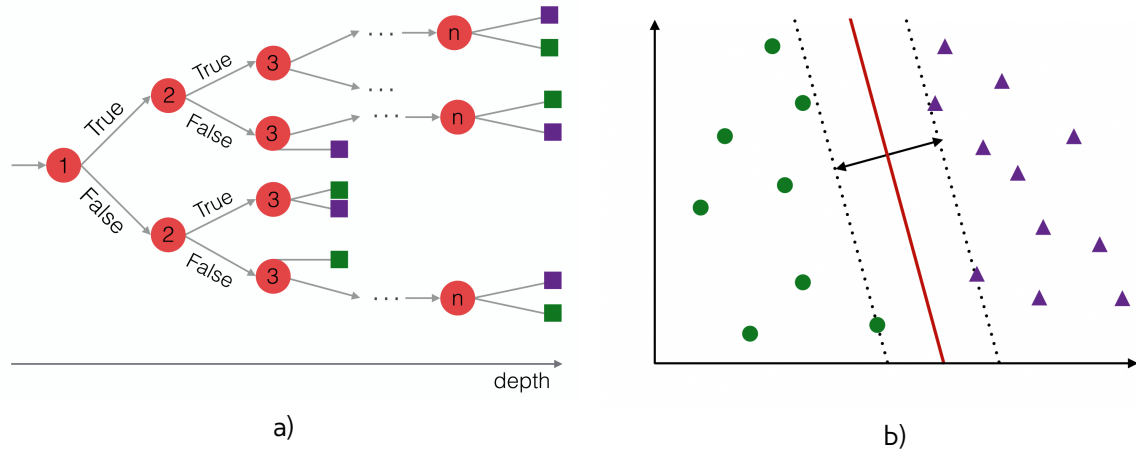


Fig. 7.10: Schematic representation of machine learning algorithms, used in the analysis for a classification of showers. Green figures represent first class of events, whereas violet ones belong to a second class. a) Representation of a binary decision tree structure: red circles correspond to nodes, that are split with respect to the one of the features. Squares represent leafs, where events classified to a certain class. Depth of the tree is calculated as a maximum number of edges from the node or leaf to the root node. b) Representation of the SVM algorithm. Dividing hyperplane is shown by a solid line. The dashed lines represent the maximum margin boundaries

where p_i is the probability to find event of class i . Each split in a variable should decrease the entropy of the system. The information gain is defined as the difference in entropy after the split:

$$IG(Q) = S_0 - \sum_{i=1}^2 S_i, \quad (7.5)$$

794 where S_0 is the initial entropy, without new node, S_i is the entropy of the one of the 2 node children.
 795 The node with the highest information gain is taken. One of the main advantages of the decision
 796 trees its simplicity of visualization and interpretation.

797 Support vector machines

Support vector machines (SVM) is a supervised machine learning algorithm which can be used for classification problems. In this algorithm each event is represented in a p -dimensional parameter space. Classification is performed by finding a hyper-plane that differentiates given two classes with the largest possible separation (Fig. 7.10 b). The hyperplane can be described with the set of points \vec{x} in a parameter space satisfying:

$$\vec{w} \cdot \vec{x} - b = 0, \quad (7.6)$$

798 where \vec{w} is the normal vector to the hyperplane and the parameter $\frac{b}{\|\vec{w}\|}$ determines the offset of the
 799 hyperplane from the origin along the normal vector \vec{w} .

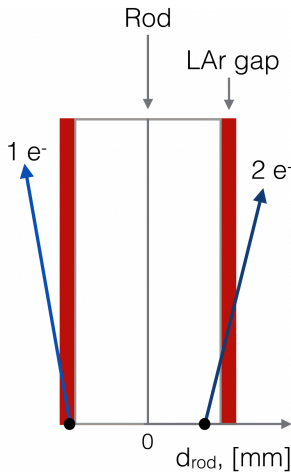


Fig. 7.11: Schematic representation of the model. Electron 1 is created in a liquid argon gap. Electron 2 is created near liquid argon gap and crosses it. This is causing a smearing of sensitive material showers distribution. Electrons created in a sensitive material tend to create more energetic showers, than electrons from a dead material. However, electrons, shown on this scheme, may give similar shower and therefore may not be distinguishable.

800 The maximum margin boundaries are described by equations:

$$\vec{w} \cdot \vec{x} - b = 1, \quad (7.7)$$

$$\vec{w} \cdot \vec{x} - b = -1, \quad (7.8)$$

801 where $\frac{2}{\|\vec{w}\|}$ is the distance between these 2 hyperplanes, so planes with the maximum margin between
802 them should have the minimum $\|\vec{w}\|$.

803 To prevent each point to fall into the margin, the following constrain should be satisfied:

$$\vec{w} \cdot \vec{x} - b \geq 1 \text{ where } y_i = 1, \quad (7.9)$$

$$\vec{w} \cdot \vec{x} - b \leq -1 \text{ where } y_i = -1, \quad (7.10)$$

where y_i represents the class of the i-th event, that can be either 1 or -1. These equations can be rewritten as:

$$y_i(\vec{w} \cdot \vec{x} - b) \geq 1 \quad (7.11)$$

It is also possible to construct a non-linear classifier by replacing the dot-product with a different kernel function. In this thesis, a radial basis function (RBF) kernel is used:

$$K_{rbf}(\vec{x}_i, \vec{x}_j) = e^{-\gamma|\vec{x}_i - \vec{x}_j|^2} \quad \gamma > 0, \quad (7.12)$$

804 where parameter γ adjusts the width of the kernel.

805 7.3.2 Model description

806 As it was mentioned in a previous sections, modules in FCAL consist of different types of material
807 and showers started inside the dead material are usually having smaller energies, than those started
808 in sensitive material. However, the validation study (Fig. 7.8) can be interpreted as an implication that

809 there are high energy showers outside the liquid argon gap. It could be explained by the fact, that
810 electron, created in a dead material, can cross a liquid argon gap and give a hit there as it is shown
811 in Fig. 7.11 (electron 2). These electrons would be indistinguishable from electrons, created directly in
812 a sensitive material (electron 1 in Fig. 7.11).

813 It was decided to treat these electrons in the same way as electrons created in the sensitive
814 material, and call the showers produced by them sensitive material showers. Showers that did not
815 crossed a liquid argon gap, are called a dead material showers. This model leads to a bigger gap size
816 from the definition.

817 From the definition, this model leads to the dependency of the liquid argon gap width on:

818 **Electron energy** The gap should get wider with higher energy of the initial electron, because of the
819 growth of the mean free path with energy.

820 **Direction of the electron** Electron aligned collinearly with liquid argon gap will have smaller prob-
821 ability to cross liquid argon gap. This probability will grow with the angle reaching its maximum
822 at 90°

823 Training sample

824 Real distributions, used in simulation, have a complicated structure and depend on a physics pro-
825 cesses simulated. Machine learning could catch these dependencies, instead of the needed ones.
826 This is why a simplified data is needed as a training sample for machine learning. The training sample
827 was made by simulation of electrons, created in forward calorimeters. In order to treat equally high
828 and low initial electron energy showers, the uniform distribution of energies is used.

829 Fig. 7.12 shows the distribution of the shower direction ($\eta^{direction}$) vs electron energy for electrons
830 coming from simulation of 1 TeV electron. Most of the showers have direction in η range between
831 3.0 and 5.0, that corresponds to position of the calorimeter. It was figured out, that the direction of
832 the shower is highly correlated with the position of the electron. Because of this it was decided to
833 use electrons with direction, uniformly distributed between 3.0 and 5.0.

834 First classifier

835 The first classifier classifier aims to categorize all showers by means of shower parameters. It is
836 possible to train supervised learning algorithm on pre-labeled artificially reduced training sample
837 and then expand the classification to the full training sample.

838 Pre-labeling could be easily done using a definitions of sensitive and dead material showers based
839 on a distance to a closest rod center (Fig. 7.13). Showers started in a liquid argon gap are 100 %
840 sensitive material showers, while showers coming from electrons born near the rod center and on
841 the edges of the the cells can be labeled as dead material showers, since there is a small probability
842 for the electron, which caused the shower, to reach the liquid argon gap.

843 For this classifier it was decided to use simple decision trees, because it has shown good clas-
844 sification efficiency (around 97%) on the reduced training sample. Different input parameters have
845 been tested, and it was figured out, that the best set of the differentiating parameters is:

- 846
- Shower energy, that is equal to the sum of all sensitive material hits energies in shower;

847

 - Maximum hit fraction. This quantity is calculated as the energy of the most energetic hit
848 divided by the shower energy;

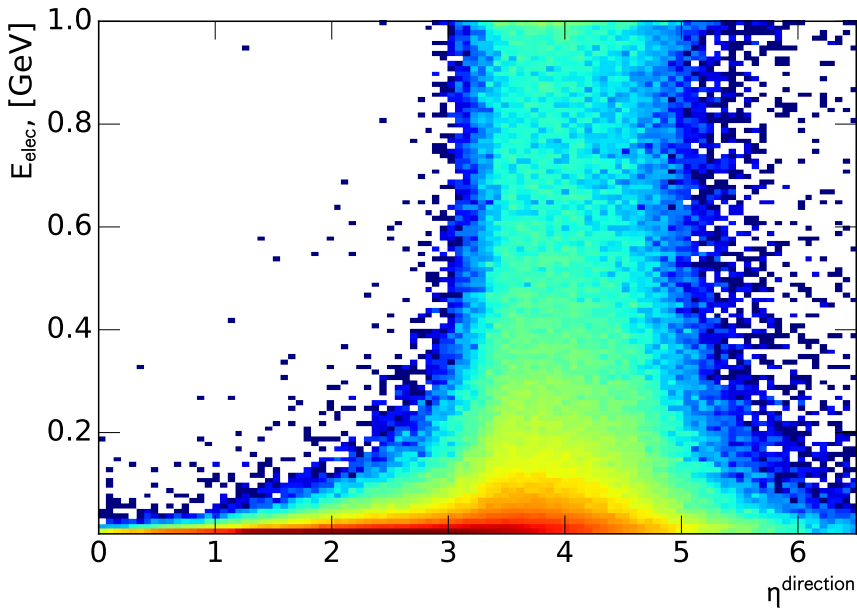


Fig. 7.12: Distribution of shower energy vs direction of shower $\eta_{momentum}$ for showers from the production of 1000 GeV electrons.

849 • RMS of the hits, calculated as a standard deviation of the hits energies in a shower.

850 Predictions of the first classifier for a full training sample is shown in Fig. 7.14 a).

851 Second classifier

852 The second classifier uses predictions of the first classifier as an input label. It is trying to reconstruct
 853 a best dividing hyperplane between two methods using a support vector machines. It uses as an
 854 input truth parameters of the electron, e.g. energy of the initial electron and its distance to a closest
 855 rod center. Different kernels have been tested and the best predictions have been obtained using
 856 RBF kernel (Eq. 7.12). Assuming, that $\eta^{momentum} \approx \eta^{position}$ classification is performed in each $\eta^{distance}$
 857 bin used in a library. Example of the classifier output is shown in a Fig. 7.14 b). As it is expected from
 858 the model, that the gap position is getting wider with higher energies of the electron. Variation of
 859 the obtained parameters have been found small, so the mean of the parameters has been used.

860 7.3.3 Interpretation of results

861 Because a full new regeneration of libraries and the validation of reconstructed variables is a time-
 862 consuming procedure, the toy Monte-Carlo method has been developed for a cross-check of clas-
 863 sifiers and its interpretation. It uses pseudorapidity $\eta^{position}$, energy of electron and distance to a
 864 closest rod center from data as a reference for a random generator. This simulation allows to com-
 865 pare shower energies and shower energies divided by the energy of the initial electron (SumE/E)
 866 distributions with distributions coming from full simulation, that are considered as a reference.

867 Several interpretations of the bin positions have been tested and the best one is shown in Fig. 7.14
 868 b) with black lines. It was decided to make 3 bins in liquid argon position instead of having only one.

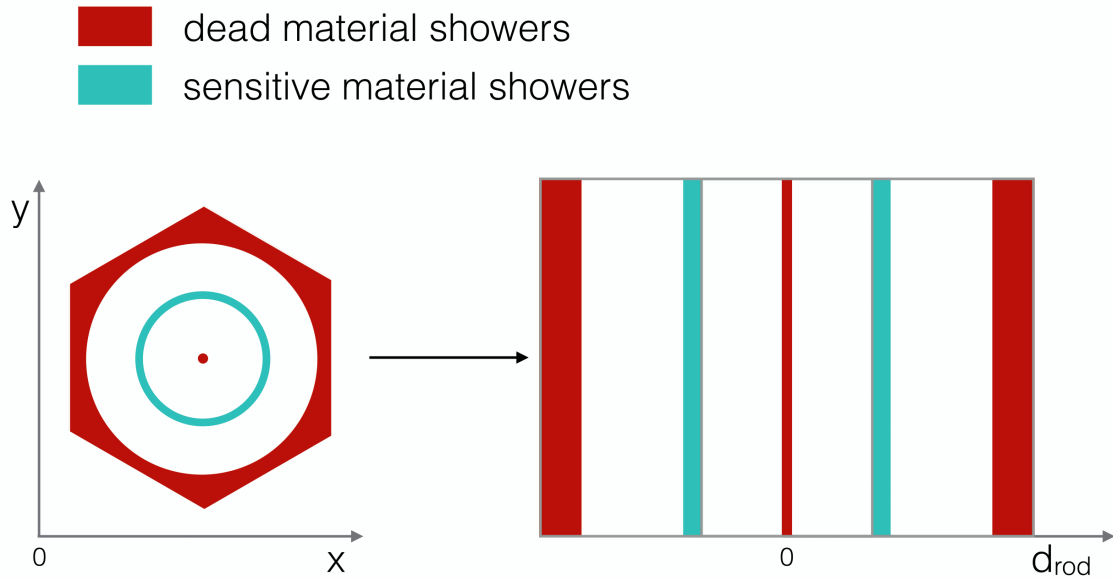


Fig. 7.13: Schematic representation of preselected data for a first classifier in x vs y (left) and distance (right) plane. Electrons, created near the rod center and on the borders of the module have low probability to cross the sensitive material, while those created inside liquid argon gap belong to sensitive material showers.

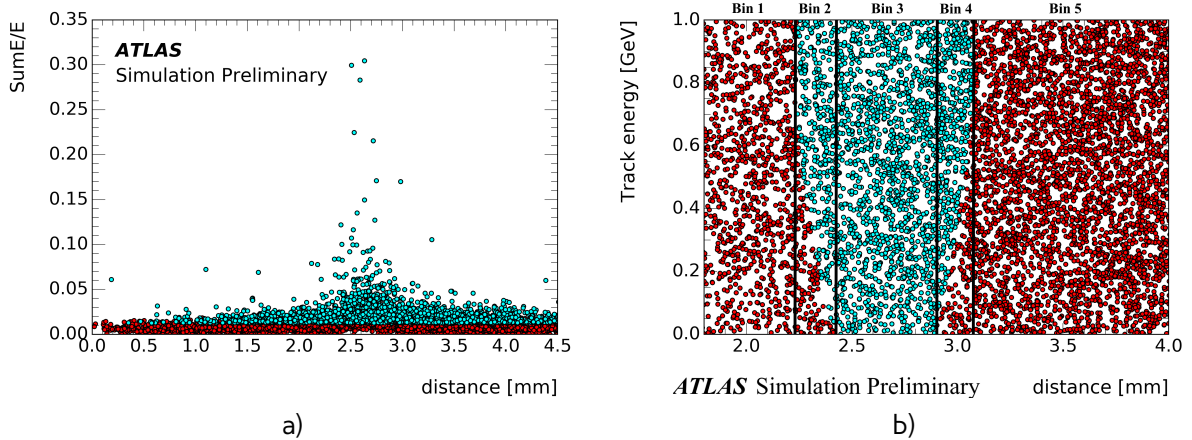


Fig. 7.14: Results of machine learning algorithm classification for a) first classifier b) second classifier. Cyan dots correspond to sensitive material showers, red to dead material showers. Black lines in Fig. b correspond to resulting bin positions

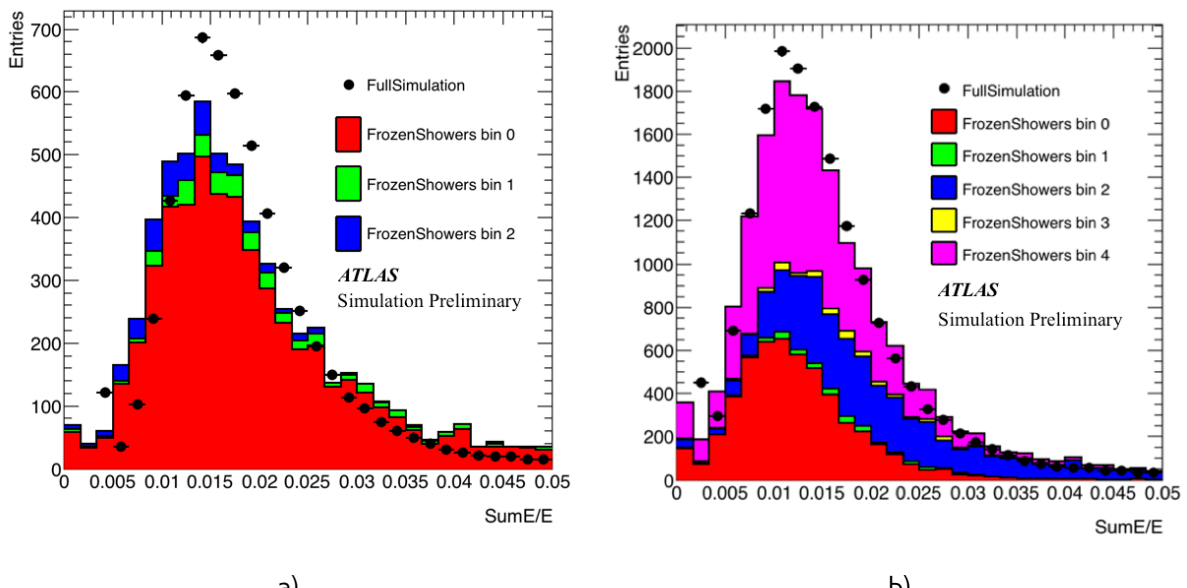


Fig. 7.15: Comparison of the distributions of shower energy divided by the energy of the initial electron between full simulation and toy MC using libraries for liquid argon gap bins and 2 closest to them bins for a) old "tuned" libraries with 1 liquid argon gap bin b) new libraries using 3 liquid argon gap bins. There are still remaining differences between full simulation and toy MC, but the new machine learning binning gives a better agreement with full simulation.

869 One bin contains, according to a classifier, just sensitive material showers events, while the other 2
870 there is a mixture of dead and sensitive material showers. The obtained positions of the liquid argon
871 bins are wider, than the nominal ones for both FCAL1 and FCAL2, as expected from the model.

872 Comparison of SumE/E distributions using toy MC on old libraries (Fig. 7.15 a) and the libraries with
873 the new binning (Fig. 7.15 b) has shown, that we could expect a better performance on reconstructed
874 values.

7.3.4 Reconstructed electron energy

876 Since the resolution of the single electrons can have a significant difference, the energies of recon-
877 structed electrons are validated before the mass validation of the different groups. Measurement of
878 the shift in the mean energy between full and fast simulation allows to correct the scale for frozen
879 showers.

Validation is performed for the following electron energies: 100 GeV, 200 GeV, 500 GeV and 1000 GeV and within the η directions that are corresponding to the 12 η bins of the library. The resolution is calculated as RMS of all reconstructed energies for the certain energy and η . The results of the electron resolution validation for the new machine learning based binning and old "tuned" libraries is shown in Fig. 7.16. The new methods gives a better or comparable resolution agreement than an old libraries. However, there are 2 bins, there new method resolution is significantly worse, than old one (3.5 and 4.3). This means, that this method still needs to be improved. The possible ways of its improvement are discussed in Sec. 7.3.5.

In a meanwhile it was decided to use a combination of the new and old libraries. The mean shift is corrected as described in Sec. 7.2.1 and showed in Fig. 7.17. The remaining differences between

890 full and fast simulation are considered negligible.

891 7.3.5 Plans for the future

892 The validation have showed a good agreement between full simulation and fast simulation for most of
893 the bins, however, because not all of the bins are performing equally well, the additional modifications
894 of the algorithm are needed. The following modifications have been investigated and planned to be
895 performed in the nearest future:

- 896 • Procedure with η dependent bin size. Currently all of the bins have the same size and position
897 of the liquid argon bin. However, because of the outlying bins, the procedure should be modified
898 and determine the bin position separately for each bin.
- 899 • Use of the closer to real case for training sample. The problem of electron resolution could be
900 also caused by too simplified models, used to train on. It is planned to repeat the procedure
901 for training sample with distributions, closer to the nominal ones.
- 902 • Adding the direction of the shower binned variable. Since there is a complicated dependency
903 between position of the electron and its direction (especially in small energy region), the addi-
904 tional binning could solve the remaining problems with electron energy resolution.
- 905 • Replacing distance to the closest rod binning by approximate path in the liquid argon.

7.3 Machine learning based bin finding procedure

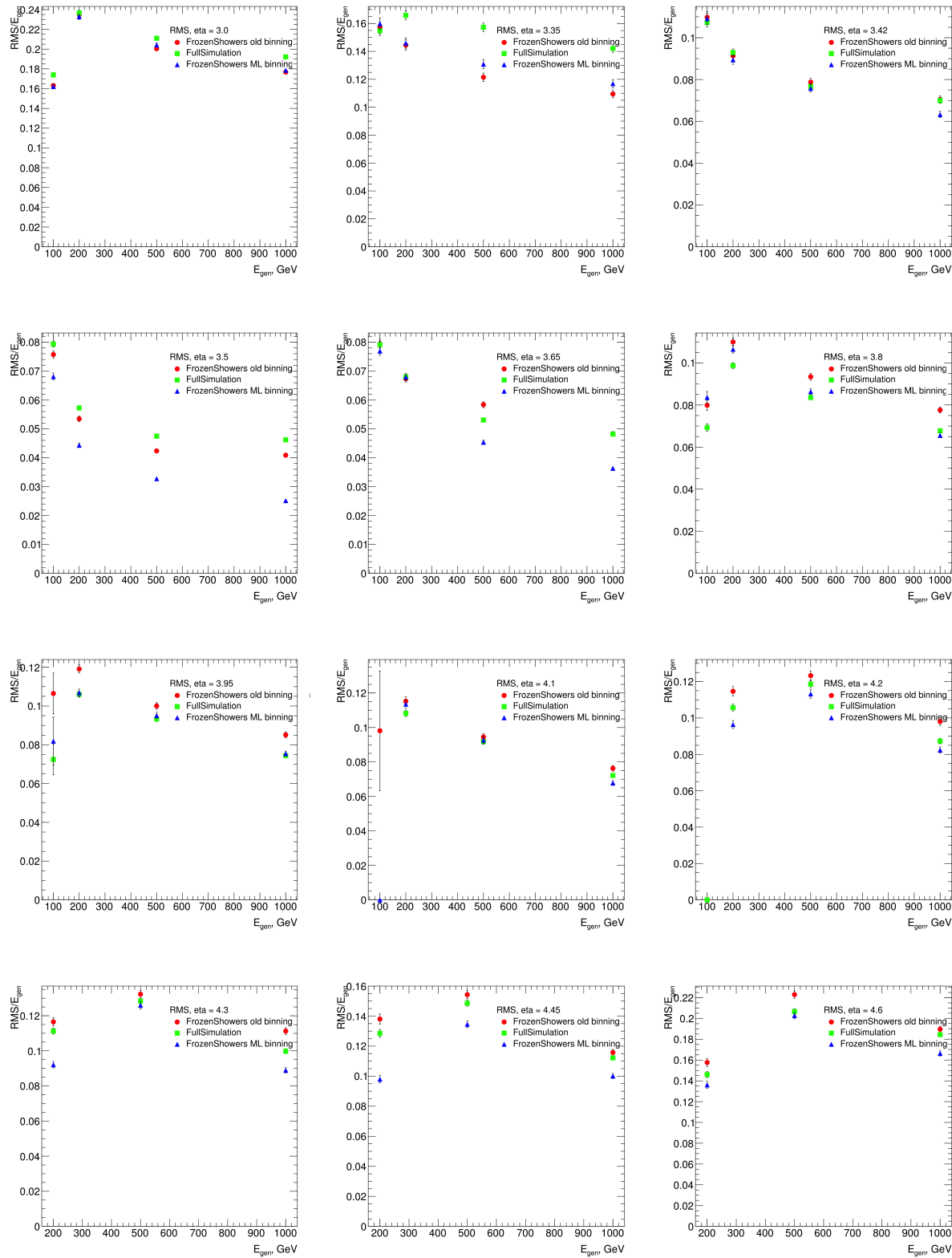


Fig. 7.16: Energy resolution of reconstructed electrons for full simulation, new libraries with ML binning and old tuned libraries with original binning for different η bins

Frozen Showers

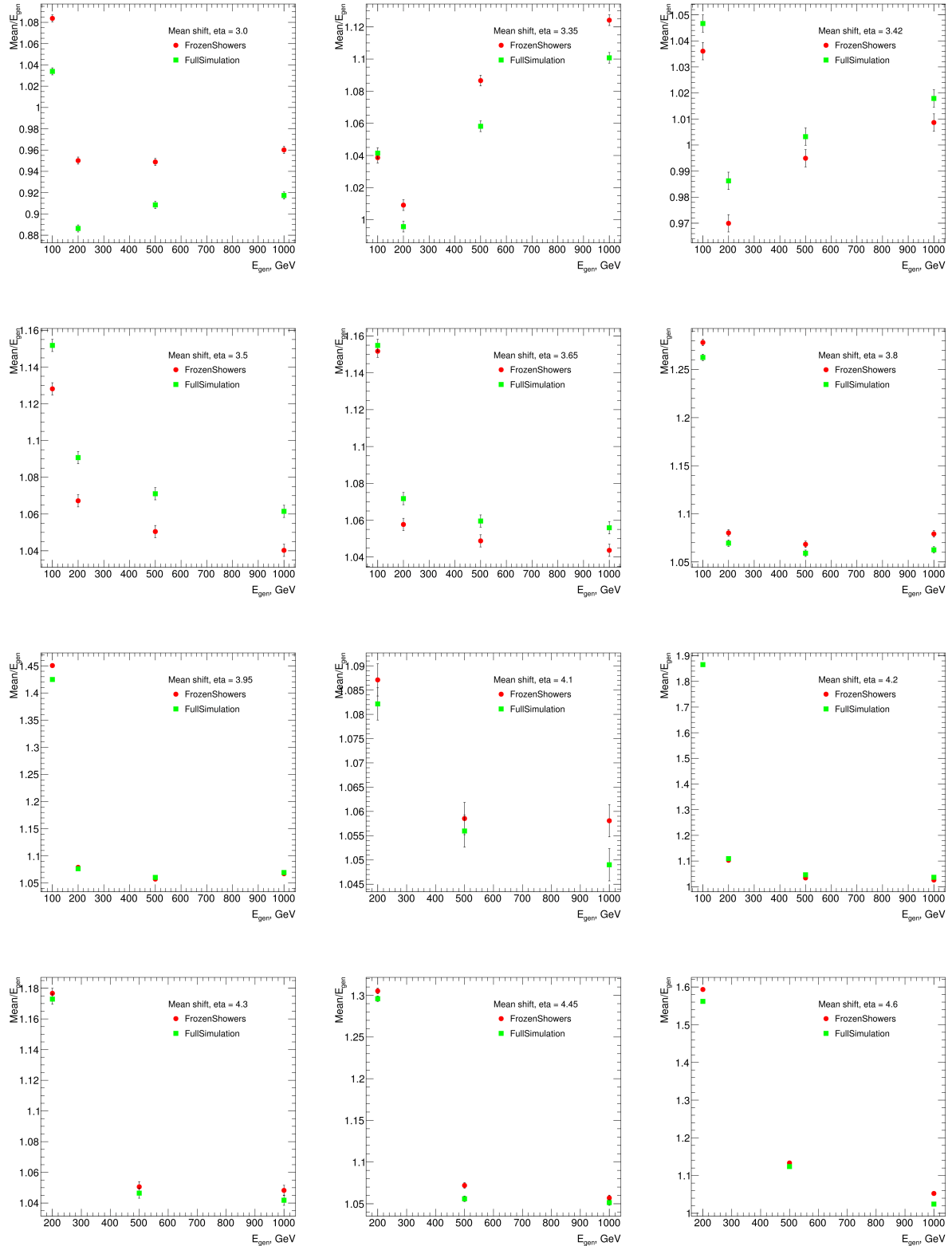


Fig. 7.17: Shift of the reconstructed energy to the truth energy of electrons for full simulation, new FS libraries with ML binning and full simulation for different η bins

906 **7.4 Validation of the new libraries**

907 The good fast simulation method should work equally good on all types of reconstructed objects,
908 this is why for each new frozen showers libraries production an new iteration of mass validation is
909 performed. The validation is done separately for each object by the different groups by comparing
910 the distibutions obtained from full and fast simulation

911 Frozen showers have been validated on following objects and showed a good agreement:

- 912 • Z bosons from $Z \rightarrow ee$ sample with one central and one forward electrons(Fig. 7.19 a). The
913 resolution of Z-mass peak is dominated by the resolution of the central electron, so Z boson
914 is mostly sensitive just to the mean energy of the forward electrons. There is visible shift in
915 the mass distribution between data and Monte-Carlo, that however, is within tolerable region.
- 916 • Jets form two jet events. The validation have showed a good agreement for all of the variables.
917 The distribution of the jet response (Fig. 7.19 b) showed, that Frozen Showers method does
918 not change the jet scale.
- 919 • Topo clusters from $t\bar{t}$ events.
- 920 • Forward electrons. The forward electrons validation have showed, that usage of the frozen
921 showers is not changing the η and E_T distributions of the forward electrons. Studies of forward
922 electrons resolution have been performed separately and will be discussed in the previous
923 section.

924 The total agreement between full and fast simulation for different objects makes a Frozen Showers
925 method applicable for a MC production in 2016.

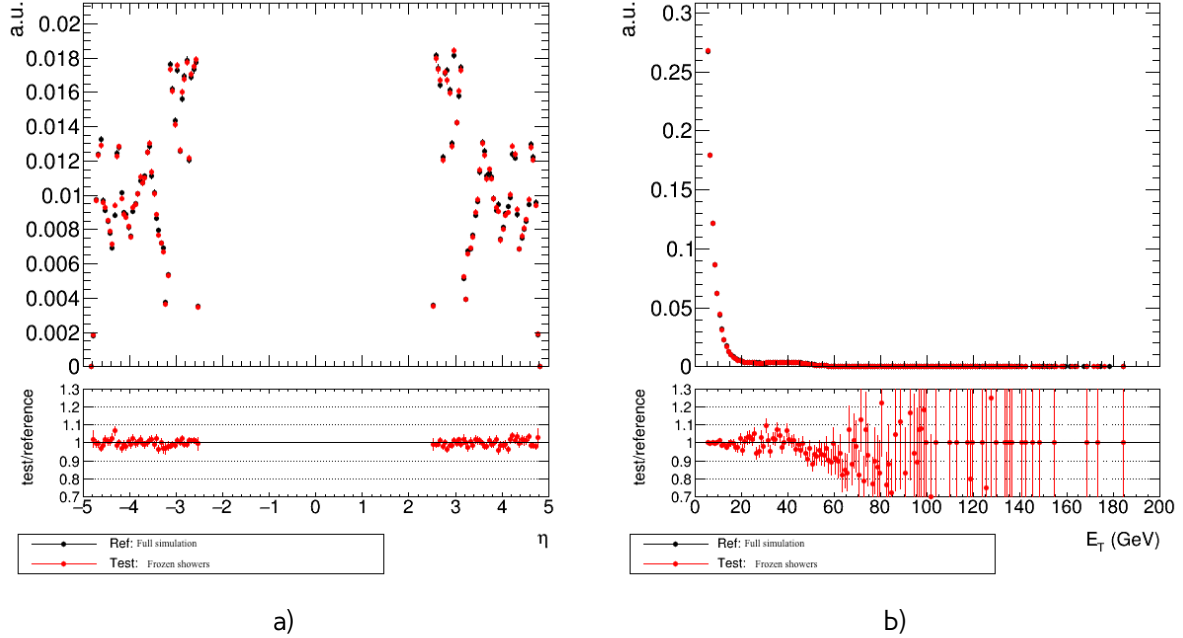


Fig. 7.18: Results of validation of the frozen showers library on forward electrons. Comparison between full simulation and fast simulation using frozen showers in forward electron events for a) pseudorapidity and b) electron transverse energy distributions. Modified from [23].

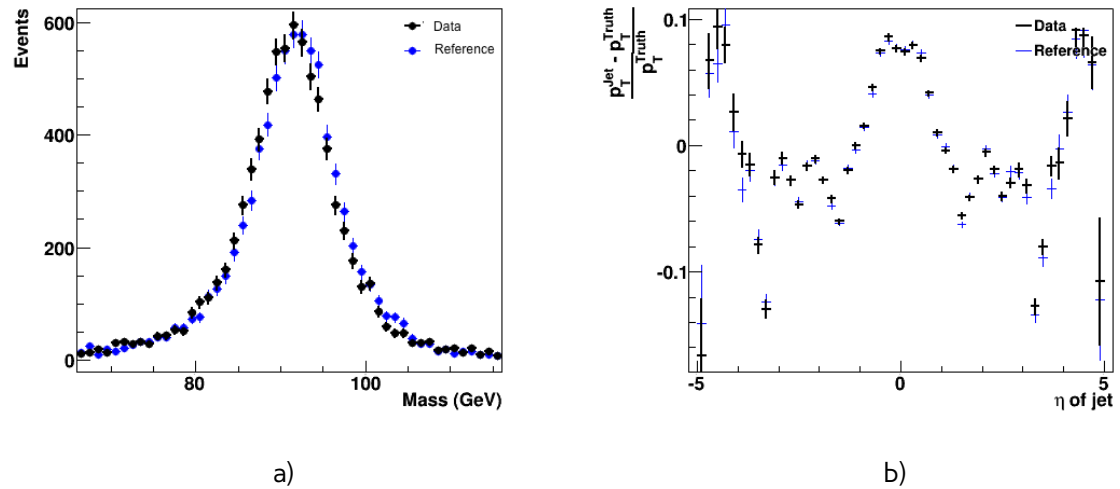


Fig. 7.19: Results of validation of the frozen showers library on jets and $Z \rightarrow ee$ sample. Comparison between full simulation and fast simulation using frozen showers for a) mass of the dilepton pair in $Z \rightarrow ee$ events (modified from [24]) b) jets response vs pseudorapditiy distribution (modified from [25]) .

927

Data and Monte-Carlo samples

928

8.1 Data sample

929 The data used in this analysis was collected in pp collisions with centre-of-mass energy 2.76 TeV
 930 during the Run-1 of the LHC operation using the ATLAS detector. This was a dedicated 2013 run for
 931 a heavy-ion group with unusual for LHC low pile-up. The mean number of interactions per bunch
 932 crossing, as shown in Fig. 8.1 a) was lower, than 1.

933 The this run ATLAS collected 4.45 pb^{-1} of data (Fig. 8.1 b)). However, not all of the data is applicable
 934 for a precise physics analysis, so the set of additional data quality (DQ) cuts was applied. It uses
 935 an information about sub-detectors, that could be disabled during data-taking. These information is
 936 stored in so called Good Run List (GRL). Total luminosity, used in the analysis is 4.0 pb^{-1} .

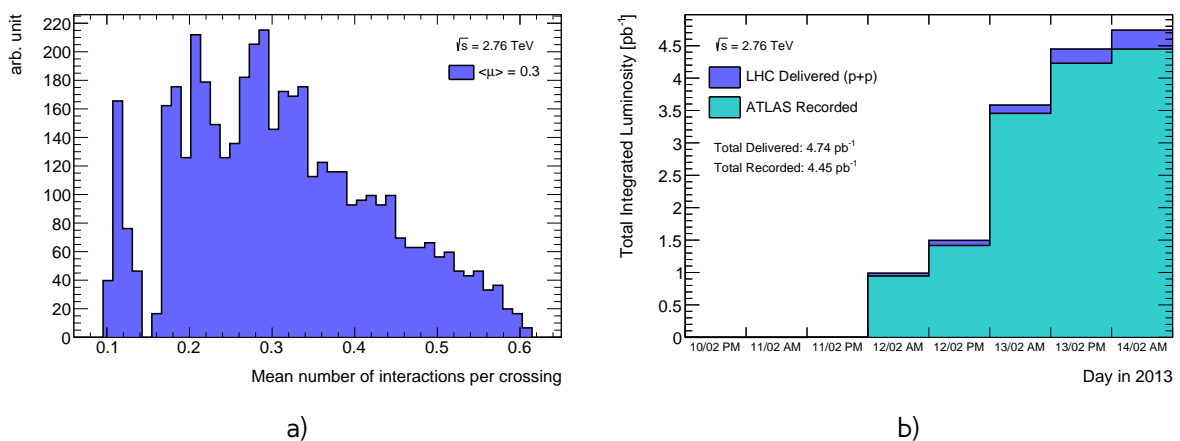


Fig. 8.1: a) Mean number of interactions per bunch crossing.

b) Cumulative luminosity versus day delivered to (dark blue), and recorded by ATLAS (light blue) during stable beams and for pp collisions at 2.76 TeV centre-of-mass energy in 2013

Table 8.1: Monte-Carlo samples, used to simulate various signals and backgrounds.

Process	Generator	N_{events}
Signal MC		
$W^+ \rightarrow e\nu$	Powheg+Pythia8	
$W^- \rightarrow e\nu$	Powheg+Pythia8	
$W^+ \rightarrow \mu\nu$	Powheg+Pythia8	
$W^- \rightarrow \mu\nu$	Powheg+Pythia8	
$Z \rightarrow ee$	Powheg+Pythia8	
$Z \rightarrow \mu\mu$	Powheg+Pythia8	
$W \rightarrow e\nu$	Sherpa	
$W \rightarrow \mu\nu$	Sherpa	
Background MC		
$W^+ \rightarrow \tau\nu$	Powheg+Pythia8	
$W^- \rightarrow \tau\nu$	Powheg+Pythia8	
$Z \rightarrow \tau\tau$	Powheg+Pythia8	
$t\bar{t}$	Powheg+Pythia6	
WW	Herwig	
ZZ	Herwig	
WZ	Herwig	
$b\bar{b}$	Pythia8	
$c\bar{c}$	Pythia8	

8.2 Monte-Carlo samples

937 The Monte-Carlo was used to simulate both signal and background processes. A summary of the
 938 MC samples used in analysis is given in Tab. 8.1. The primary signals MC is generated using Powheg
 939 generator using CT10 [26] PDFs interfaced with Pythia8 for parton showering using AU2 [27] tune.
 940 There is also additional signal MC sample for W-analyses, generated using Sherpa with CT10 PDFs.
 941 This sample is used for studies of the effect of matrix elements on final cross-section (see Chap.
 942 14).

943 The background sources are used to estimate fraction of the background events. The more de-
 944 tailed explanation of the background sources could be found in Chap. 12. The $W \rightarrow \tau\nu$ and $Z \rightarrow \tau\nu$
 945 are generated similarly to signal MC with Powheg+Pythia8 generator with CT10 PDF and AU2 tune.
 946 Events with diboson decays are generated by Herwig with CTEQ6L1 [28] PDF set and using AUET2 [29]
 947 tune. The $t\bar{t}$ sample generated using Powheg generator interfaced with Pythia6. The additional $b\bar{b}$
 948 and $c\bar{c}$ samples have been generated for QCD background determination and cross-check (Sec. 12.1)
 949 and generated using Pythia8 with AU2 tune and CTEQ6L1 PDF set.

951

Part III

952

The Measurement

954

Selection

955 Selection criteria is a set of requirements, that are applied both on data and MC. The selection
 956 criteria should separate process of interest (signal) from other processes. For $pp \rightarrow W \rightarrow ev/\mu\nu$
 957 and $pp \rightarrow Z/\gamma^* \rightarrow ee/\mu\mu$ selection criteria can be divided into 3 groups: data quality, lepton
 958 and boson cuts. The full set of cuts is summarized in a Tab. 9.1. In this chapter all of them will be
 959 discussed and a cut flow presented.

960

9.1 Data quality cuts

961 Data taking conditions are important in the analysis because of the possible biases. In order to pre-
 962 serve high data quality some events must be rejected. The reason may be unstable beam conditions,
 963 disabled parts of the detector or events with too many noisy cells. Numbers of runs, that can be

Table 9.1: Selection criteria

Data quality event selection	
Single lepton trigger	
Good Run List	
Reject events with LAr errors	
Number of tracks at primary vertex ≥ 3	
Lepton selection	
Electron Selection	Muon Selection
EF_e15_loose1 $P_T^l > 20\text{GeV}$ $ \eta^l < 2.47$ excluding $1.37 < \eta^l < 1.52$ OQ cut Medium electron identification $P_T^{cone,20} < 0.1$	EF_mu10 $P_T^l > 20\text{GeV}$ $ \eta^l < 2.5$ staco reconstruction chain combined muon $P_T^{cone,20} < 0.1$
W boson selection	Z boson selection
$E_T^{\text{miss}} > 25\text{ GeV}$ $M_T^W > 40\text{ GeV}$	$66 < M^Z < 116\text{ GeV}$

Table 9.2: Number of W boson candidates in data and signal MC, remaining after each major requirement. The signal MC is normalised to the NNLO cross-section shown in Tab. 12.1

Requirement	Number of candidates			
	Data	signal MC	Data	signal MC
	$W^+ \rightarrow e\nu$ $W^- \rightarrow e\nu$			
No selection	27491466	8354	27491466	5002
Event selection	333054	6044	333054	3139
Lepton selection	15075	4315	15075	2306
Boson selection	3914	3544	2209	1941
	$W^+ \rightarrow \mu\nu$ $W^- \rightarrow \mu\nu$			
No selection	27491466	8354	27491466	5002
Event selection	26475095	8226	26475095	4916
Lepton selection	11466	4782	11466	2595
Boson selection	4365	3936	2460	2164
	$Z \rightarrow ee$ $Z \rightarrow \mu\mu$			
No selection	27491466	1196	27491466	1196
Event selection	333054	1051	333054	1051
Lepton selection	459	430	459	430
Boson selection	430	418	430	418

used in the analysis are stored in the so-called Good Run List (GRL), which in the addition to the run numbers contains also information about luminosity blocks.

Events, where LAr calorimeter was malfunctioning are excluded by LAr quality criteria. Furthermore events are required to have at least one primary vertex from a hard scattering with at least 2 tracks, that are reconstructed from this vertex.

Online selection of events is based on a single lepton trigger, depending on a lepton flavor. For electron analysis EF_e15_loose1 trigger is used, which records electrons with $E_T > 15$ GeV. This trigger uses additional "loose" isolation requirements to exclude jets, that are misidentified as electrons. In the muon channel the lowest single lepton trigger is EF_mu10. It records events containing muons with $E_T > 10$ GeV.

9.2 Lepton quality cuts

Both analyses use similar selection criteria, applied on leptons. The leptons must satisfy requirement $P_T^l > 20$ GeV and match to the event trigger.

Electron candidates are required to be within pseudorapidity range $|\eta^l| < 2.47$. The electron candidates found within the transition region between the barrel and the endcap electromagnetic calorimeters, $1.37 < |\eta^l| < 1.52$, are removed. Additionally, for a better multijet background rejection medium identification and $P_{T\text{cone},20}^l < 0.1$ criterias are applied. The object quality (OQ) cut is applied in order to remove events from runs with dead front end boards in the calorimeter.

Muons have to satisfy the following criteria: they should be reconstructed by a staco algorithm in a muon spectrometer and fall within range $|\eta^l| < 2.5$. Set of medium requirements is applied. They

984 must also satisfy $P_T^{cone,20} < 0.1$ isolation criteria.

985 9.3 Boson selection

986 The events, containing W boson candidates are required to have exactly one lepton, fulfilling the
987 lepton selection. Missing transverse energy, used as a proxy for a neutrino from W decay is required
988 to be $E_T^{miss} > 25\text{GeV}$. The transverse mass, calculated from the lepton and missing transverse energy
989 as in Eq. 3.5 has to be bigger than 40 GeV ($M_T^W > 40 \text{ GeV}$).

990 The reconstructed lepton pair in case of Z boson analysis is required to have the invariant mass
991 between 66 and 116 GeV. Both upper and bottom limits allow to exclude regions with high background
992 contamination.

993 9.4 Cut flow

994 The effect of each selection can be studied using cut-flows, which show the number of events
995 passing each set of cuts in a sequential order. Cut flows for W and Z analysis are shown in a Tab.
996 9.2.

997 Chapter **10**

998 **Monte-Carlo corrections**

999 Monte Carlo plays important role in the cross-section measurement. It is constantly being improved,
1000 in order to obtain a better precision in data description. Part of these corrections have been described
1001 in Chap. 6. Unfortunately, not everything can be taken into account during simulation itself. This
1002 leads to differences between data and Monte Carlo, that need to be accounted for. There are two
1003 possible methods to correct Monte Carlo without regenerating it. First one is to apply event weights,
1004 so that each MC event can contribute by a non one entry to a histogram. This procedure is called
1005 event reweighting. Second one is a MC smearing. It uses random numbers to alter the reconstructed
1006 4-vectors.

1007 This chapter describes all additional corrections, that have been applied on MC samples in this
1008 analysis. All of these correction are introducing additional systematic error, that will be discussed in
1009 the Chap. 14.

1010 **10.1 Lepton efficiency corrections**

1011 The efficiency of lepton detection at ATLAS detector can be divided into three components:

- 1012 • The reconstruction efficiency ϵ_{rec} is a probability to reconstruct lepton as a lepton of this
1013 flavor.
- 1014 • The identification efficiency $\epsilon_{id|rec}$ is a probability that a reconstructed lepton survives identi-
1015 fication requirements.
- 1016 • The trigger efficiency $\epsilon_{trig|rec,id}$ is a probability, that the lepton satisfies the trigger requirements.

The full efficiency for a single lepton can be written as:

$$\epsilon_{total} = \epsilon_{rec} \times \epsilon_{id|rec} \times \epsilon_{trig|rec,id} \quad (10.1)$$

1017 All these efficiencies are measured using tag-and-probe method in $Z \rightarrow ll$ decays. One of the
1018 leptons from Z boson, called "probe", is initially selected with all of the cuts, except the one under
1019 study. Second one, called "probe", satisfies tighter selection with some additional cut, e.g. trigger
1020 matching.

1021 The reconstruction efficiency is associated with the algorithm used in the event reconstruction
1022 process. This is causing differences between electrons and muons efficiencies. In the electron case
1023 the reconstruction efficiency is understood as a probability to reconstruct an electron which has
1024 deposited its energy in electromagnetic calorimeter cluster as an electron candidate.

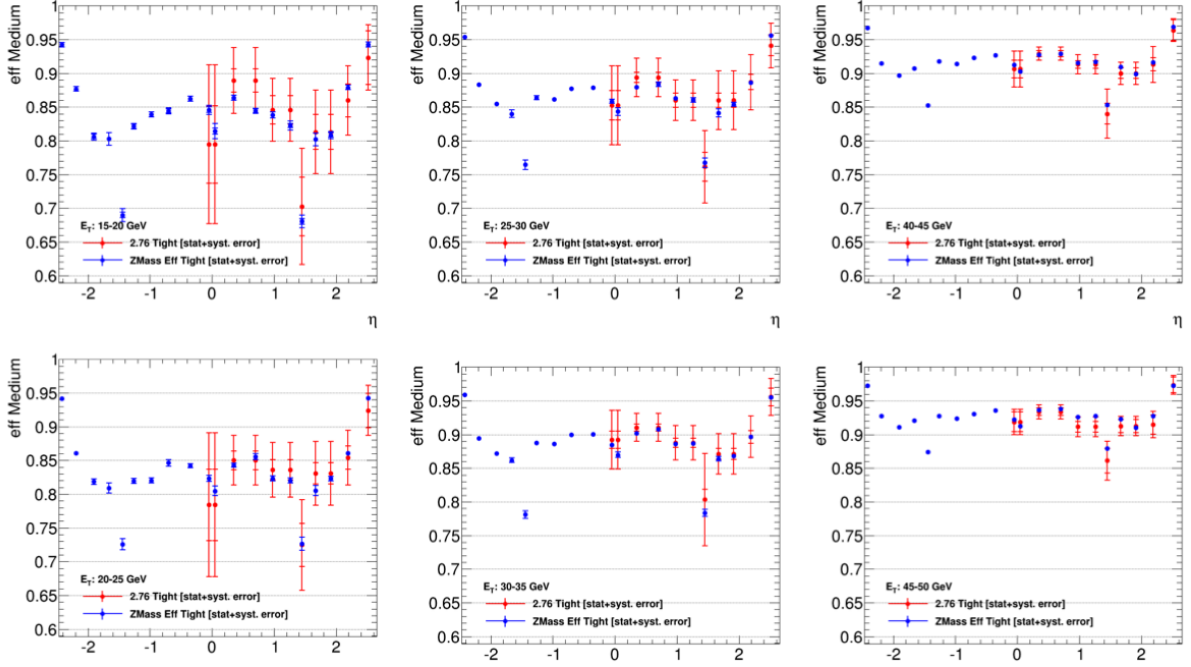


Fig. 10.1: Comparison of electron efficiencies as calculated for 8TeV (blue points) and 2.76TeV (red points) for MC simulation. Efficiencies are shown as a function of pseudorapidity (η) for different electron E_T bins. Both statistical and systematic uncertainties are shown.

The muon reconstruction efficiency is given by:

$$\epsilon_{reco,\muon} = \epsilon_{reco,\muon|ID} \cdot \epsilon_{ID} \approx \epsilon_{reco,\muon|ID} \cdot \epsilon_{ID|MS}, \quad (10.2)$$

where $\epsilon_{reco,\muon|ID}$ is a conditional probability that a muon reconstructed in ID is also reconstructed using MS as a combined muon, and ϵ_{ID} is a probability that the muon is reconstructed as an ID track. This quantity ϵ_{ID} cannot be measured directly in the data and therefore is replaced by $\epsilon_{ID|MS}$ - probability that muon reconstructed in MS is also reconstructed in ID, that can be measured by the tag-and-probe method.

Simulation samples are corrected to match data efficiencies by a scale-factor :

$$SF_{reco,id,trig} = \frac{\epsilon_{reco,id,trig}^{data}}{\epsilon_{reco,id,trig}^{MC}}. \quad (10.3)$$

The scale factors are calculated in P_T^l and η^l bins and have associated statistical and systematic uncertainty components. The statistical component is connected to a size of $Z \rightarrow ll$, which in our case is around 500 events per each lepton flavor. This makes statistical error the dominant one and means that precise calculation of scaling factors based on this data is difficult.

It is possible, however, to use scale factors for 8 TeV 2012 data. The main difference between these data samples are center of mass energy and the pile-up conditions (10 in 2012 and less than 1 in 2013). The effects of these differences have been studied by the electron performance group at ATLAS using $Z \rightarrow ee$ MC sample. Fig. 10.1 shows the scale factors for different P_T^l ranges as a function of η^l , for the MC data produced at 2.76TeV and 8 TeV centre-of-mass energy. The differences in the

Table 10.1: Muon trigger scale factors

	SF	SF stat.error
μ	0.988	0.011
μ^+	1.012	0.015
μ^-	0.964	0.015

scale factors are negligible and fully covered by the statistical errors. This justifies the usage of 8 TeV scaling factors with increased uncertainty (that is considered to be fully statistical) in the analysis at 2.76 TeV.

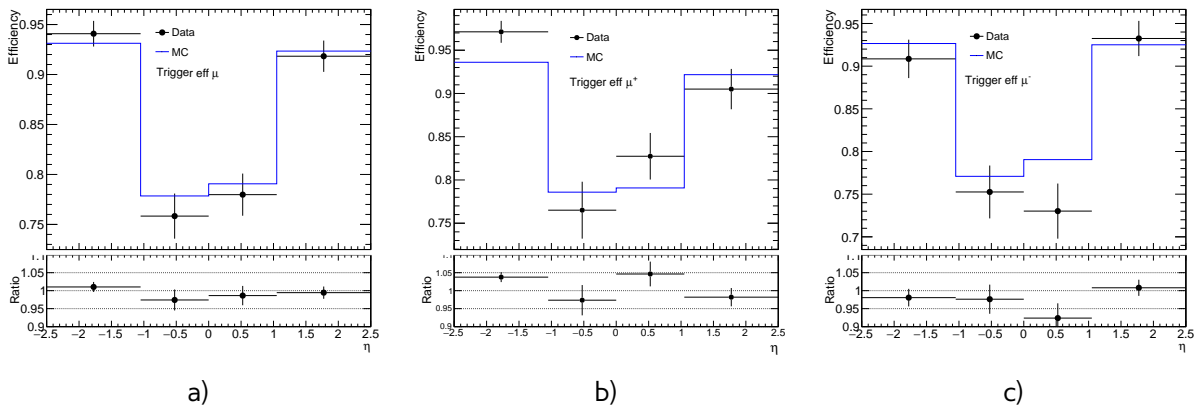
10.1.1 Muon Trigger SF

Unfortunately, single muon trigger has not been present in the 2012 data, so muon trigger scale factor had to be derived from the 2.76 TeV data. The size of the Z sample is not big enough to make the scale factors in P_T^l and η^l bins.

Since the P_T^μ cut is significantly higher, than the trigger threshold, the trigger efficiency in P_T^μ can be considered flat. On the another hand, the η dependence are expected. Binning in η is motivated by the detector construction: $|\eta| < 1.05$ corresponds to a barrel part of the muon spectrometer, while $1.05 < |\eta| < 2.5$ is an end-cap MS (see Sec. 4.2.4). The muon trajectory is bend in a magnetic field. That can lead to small differences in a trigger efficiencies for different muon charges. Possible charge dependency of the scale factors also have been studied.

Total scale factors are presented in Tab. 10.1. Scale factors for μ^+ and μ^- are more than 3σ away from each other, that is a clear indicator of a charge dependency. Trigger efficiencies for data and MC in η bins are shown in a Fig. 10.2.

Effect of applying different scale factors on muon for W analysis is shown on Fig. 10.3 - 10.5. Best agreement with data is achieved by applying single bin scale factor. This, together with the fact that difference in efficiencies is smaller than 1σ for most of the η bins motivates a choice of single bin charge dependent scale factor for this analysis.


 Fig. 10.2: Trigger scale efficiencies distribution for a) μ b) μ^+ c) μ^- as a function of pseudorapidity

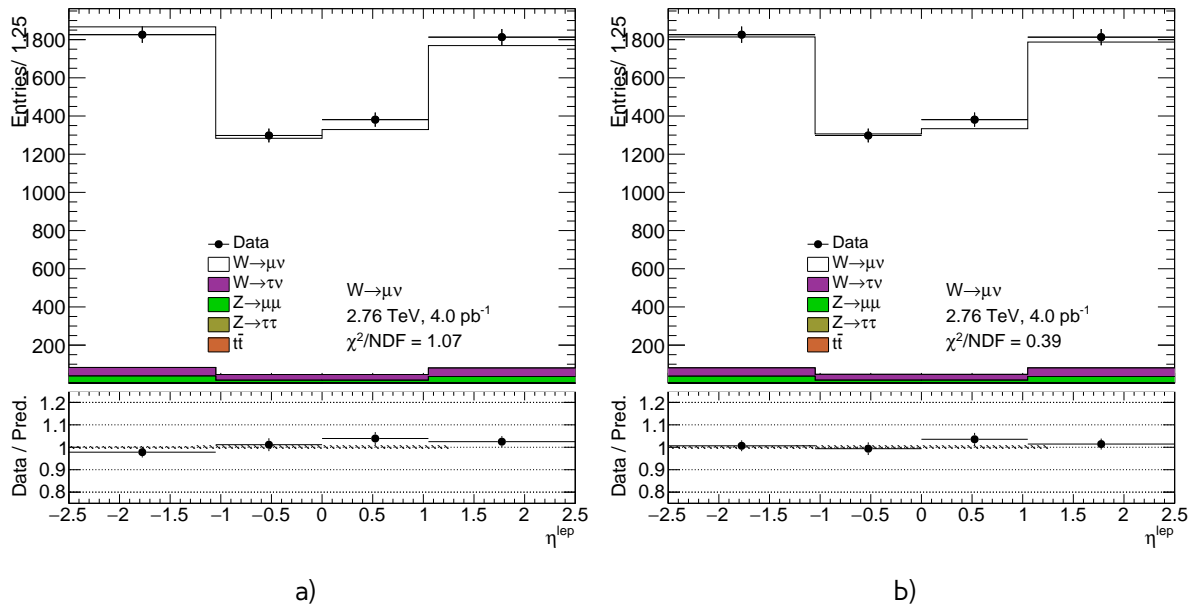


Fig. 10.3: Muon pseudorapidity distribution from the $W \rightarrow \mu\nu$ selection with a) binned b) not binned charge dependent trigger scale factor applied

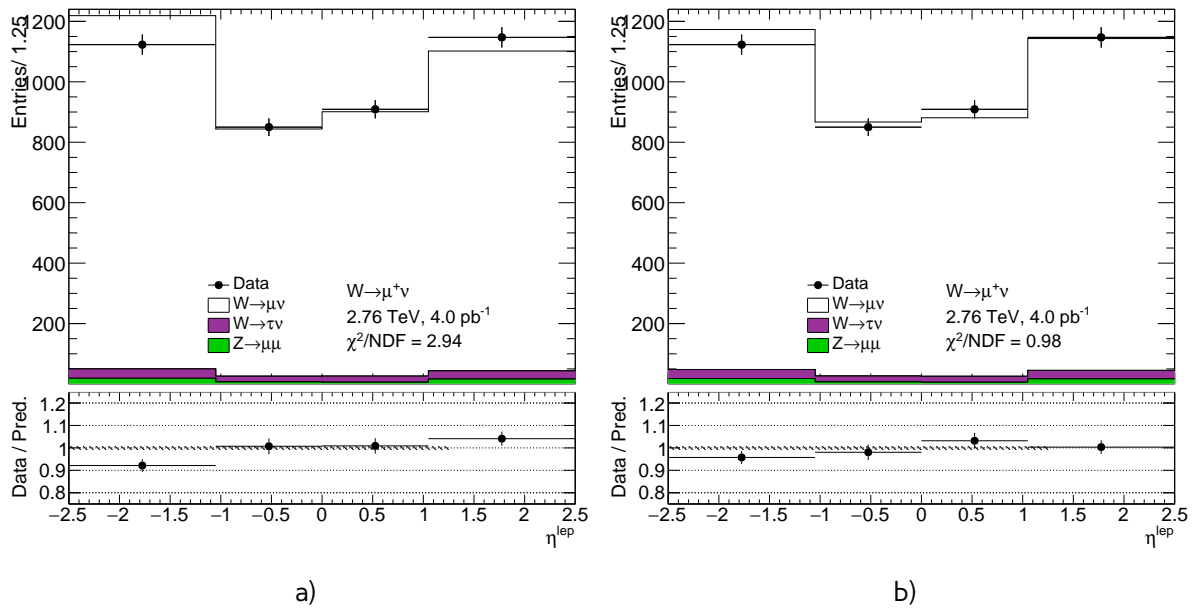


Fig. 10.4: Muon pseudorapidity distribution from the $W \rightarrow \mu^+ \nu$ selection with a) binned b) not binned charge dependent trigger scale factor applied

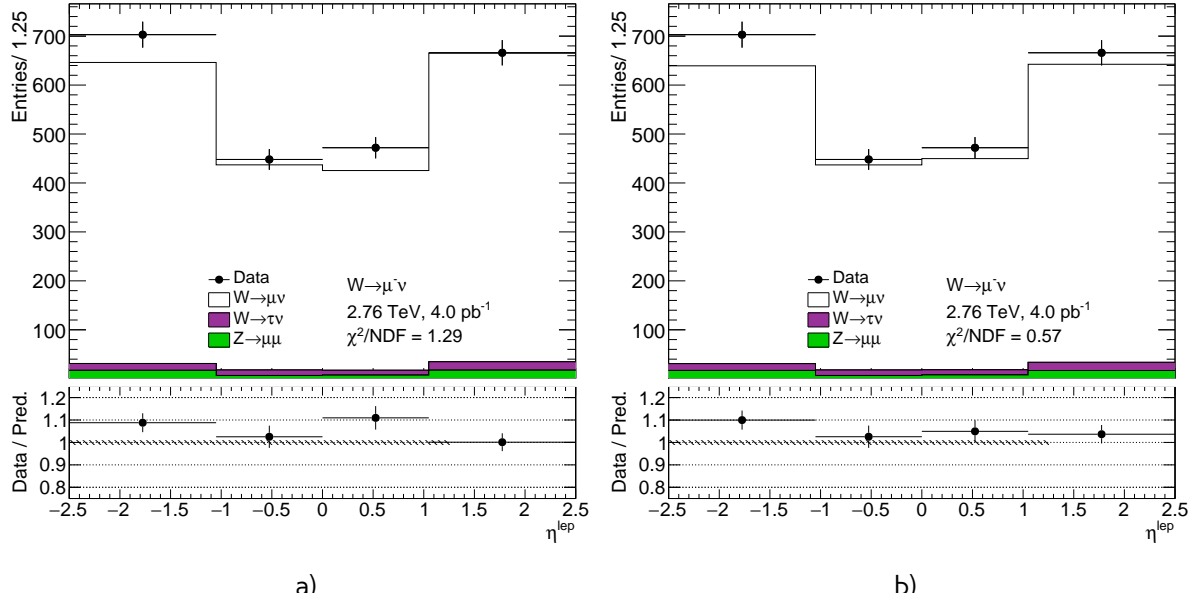


Fig. 10.5: Muon pseudorapidity distribution from the $W \rightarrow \mu^- \nu$ selection with a) binned b) not binned charge dependent trigger scale factor applied

10.2 Electron energy scale and resolution

The energy of the reconstructed electron clusters tends to be shifted in comparison to the true energy of the initial electron. The correction of this shift is done in both data and MC as a 3 step procedure:

- Electronic calibration, that transfers a raw signal from a readout to a cluster energy deposit.
- MC based calibration. It corrects the effects of the energy loss in the material in front of the calorimeter and the leakage into the hadronic calorimeter. This calibration is applied on both data and MC.
- Correction of the calorimeter cell response in the data. This allows to get the right response in non-optimal HV-regions and to exclude biases in the calorimeter electronics reconstruction.

The energy shift is parametrised, as:

$$E^{\text{data}} = E^{\text{MC}}(1 + \alpha_i), \quad (10.4)$$

where E^{data} and E^{MC} are the energies in data and simulation, respectively and α_i is a mean shift in a given bin i in η . The effect of this miscalibration on a reconstructed mass of Z boson neglecting second order terms is:

$$m_{i,j}^{\text{data}} = m_{i,j}^{\text{MC}}(1 + \alpha_{i,j}), \quad \alpha_{i,j} \sim \frac{\alpha_i + \alpha_j}{2}, \quad (10.5)$$

where $m_{i,j}^{\text{data}}$ and $m_{i,j}^{\text{MC}}$ are the reconstructed mass of the Z boson in i and j bins in η for data and MC respectively.

Additionally the difference in the electron resolution has to be corrected. The dependency of electron resolution on its energy was described by Eq. 7.1. It is assumed, that the sampling and

the noise terms are well modeled by the MC simulation and the main difference is coming from a constant term. So, the electron resolution correction can be written as:

$$\frac{\sigma_E}{E_i}^{Data} = \frac{\sigma_E}{E_i}^{MC} \oplus c_i \quad (10.6)$$

where c_i is an η dependent relative resolution correction. Similarly to an energy scale correction it is possible to derive resolution correction factor by a comparison of $m_{i,j}^{data}$ and $m_{i,j}^{MC}$ distributions.

The correction values α_i and c_i are obtained via the χ^2 fit of an invariant mass of electron pairs in data and MC. The resulting energy scale is applied to the data, while the resolution is corrected in MC. The resulting scale is validated using the $J/\psi \rightarrow ee$ and $Z/\gamma \rightarrow ee$ samples.

10.3 Muon momentum correction

The muon momentum resolution depends on η , ϕ and p_T of the muon [3]. There is an empirical formula to describe it inside the detector (ID or MS):

$$\frac{\sigma_{Det}(p_T)}{p_T} = \frac{r_0^{Det}(\eta, \phi)}{p_T} \oplus r_1^{Det}(\eta, \phi) \oplus r_2^{Det}(\eta, \phi) \cdot p_T. \quad (10.7)$$

The first term originates from the fluctuations of the energy loss in the traversed material. The second term is coming from the magnetic field inhomogeneities and the local displacements. The third term describes the intrinsic resolution effects.

Similarly to electrons, the overall energy scale shift between data and MC is parameterised as:

$$p_T^{data} = p_T^{MC} + s_0^{Det}(\eta, \phi) + s_1^{Det}(\eta, \phi) \cdot p_T^{MC}, \quad (10.8)$$

where $s_0^{Det}(\eta, \phi)$ is coming from the imperfect knowledge of energy losses for muons passing through detector.

This leads to a total correction formula:

$$p_T^{Cor,Det} = \frac{p_T^{MC,Det} + \sum_{n=0}^1 s_n^{Det}(\eta, \phi) (p_T^{MC,Det})^n}{1 + \sum_{m=0}^2 \Delta r_m^{Det}(\eta, \phi) (p_T^{MC,Det})^{m-1} g_m}, \quad (10.9)$$

where g_m are normally distributed random variables with the mean 0 and the width 1. Due to a small amount of material between the interaction point and the ID, $\Delta r_0^{ID}(\eta, \phi)$ and $s_0^{ID}(\eta, \phi)$ are set to 0. The misalignment effect of the MS is corrected on a simulation level by adding a random smearing to the alignment constants. This allows to set $\Delta r_2^{MS}(\eta, \phi)$ to 0 during the fit.

The correction factors are extracted using events with $Z \rightarrow \mu\mu$, where muon candidates fulfill the combined muon criteria described in Sec.5.3. For the correction, the invariant mass distributions $m_{\mu\mu}^{ID}$ and $m_{\mu\mu}^{MS}$ are considered individually within a specific $\eta - \phi$ region of the fit. The combined muon parameters are used to obtain angles η and ϕ . The correction extraction is performed first for the ID and then for the MS. Additionally, the following fit variable is considered:

$$\rho = \frac{p_T^{MS} - p_T^{ID}}{p_T^{ID}}, \quad (10.10)$$

1086 which represents the p_T imbalance between the ID and the MS.

In a second step corrections are propagated to the combined momentum, using a weight average:

$$p_T^{Cor,CB} = f \cdot p_T^{Cor,ID} + (1 - f) \cdot p_T^{Cor,MS}, \quad (10.11)$$

1087 where the weight f is derived from the MC.

1088

Chapter 11

Hadronic recoil calibration

1090

1091

11.1 Introduction	75
11.2 Hadronic recoil resolution correction	78
11.2.1 Event activity correction	78
11.2.2 Resolution corrections using Z events	84
11.3 Hadronic recoil bias correction	87
11.3.1 Bias determination from M_T^W distribution	88
11.3.2 Bias determination using u_{\parallel} distribution	90
11.3.3 Systematic uncertainty estimation	91
11.4 Summary on hadronic recoil systematics	91

1092

As it was mentioned in Sec. 5.4 due to the discrepancies between data and Monte-Carlo, this analysis uses a hadronic recoil based algorithm for the missing transverse energy reconstruction. The missing transverse energy E_T^{miss} affects significantly the W boson measurement, so it is important to have a solid understanding of possible sources of differences in the hadronic recoil reconstruction in the data and the Monte-Carlo.

This chapter describes the procedure of the calibration bias and the resolution mismodelling corrections for a hadronic recoil, that was adapted for the 2.76 TeV data.

11.1 Introduction

This analysis uses a standard hadronic recoil calibration procedure, described in [30], that was modified and adapted for the low statistics 2.76 TeV case. The standard procedure consist of the 3 main steps.

The first step in the hadronic recoil calibration procedure aim to correct differences in the pile-up modeling in the event. Additional interactions can have a significant effect on E_T^{miss} and $\sum E_T$ distributions. These discrepancies are usually corrected by reweighting average number of interactions per bunch crossing in MC to match the data. However, the ATLAS simulation is adjusted for high pile-up runs, so this quantity is modeled discrete in case of 2.76 TeV analysis (Fig. 11.1), what makes the precise reweighting impossible. However, since the mean number is below 1, effect of these discrepancies on E_T^{miss} distributions can be neglected.

In the second and the third steps possible discrepancies in the resolution and the scale of the hadronic recoil are corrected. The hadronic recoil algorithm performance can be studied in MC through the projection of $\vec{H}\vec{R}$ on the direction of the transverse momentum of the vector boson, as

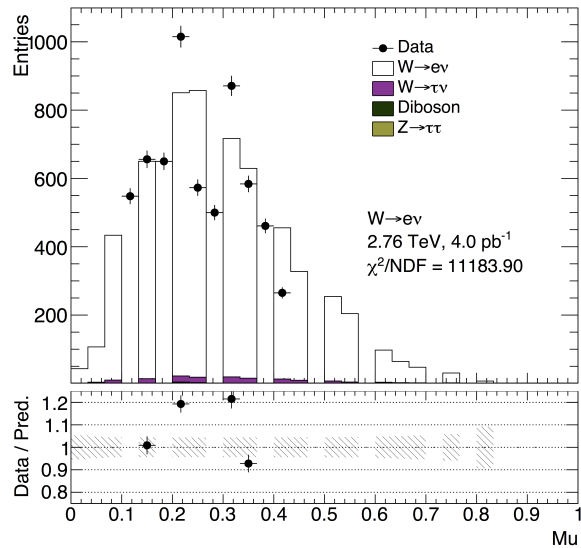


Fig. 11.1: Mean number of interactions per bunch crossing in $W \rightarrow e\nu$ events. In MC the pileup is modeled in a few bins only, that makes the application of the standard data to MC reweighting procedure not feasible.

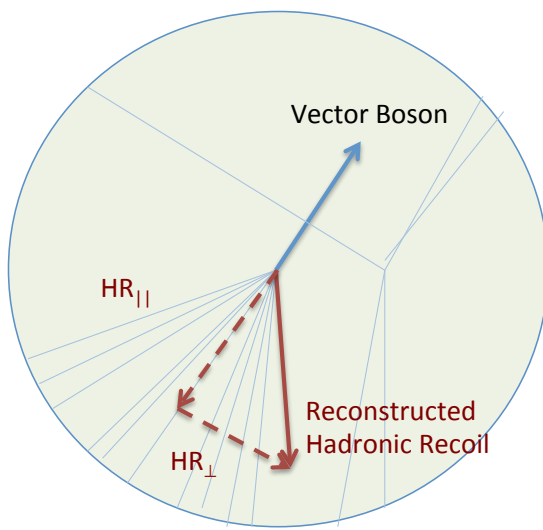


Fig. 11.2: Parallel and perpendicular projections of the hadronic recoil with respect to the transverse momentum of the vector boson [10]

shown in Fig. 11.2. This projection can be divided into perpendicular u_{\perp} and parallel u_{\parallel} components as follows:

$$u_{\parallel} = \vec{v}_{xy} \cdot \vec{HR} \quad (11.1)$$

$$u_{\perp} = v_x \cdot HR_y - v_y \cdot HR_x, \quad (11.2)$$

where \vec{v}_{xy} is a unitary vector along the transverse component of a vector boson momentum and v_x and v_y are its projections on x and y axis respectively. In the case of the true kinematics $u_{\parallel} = -p_T^{bos}$ and $u_{\perp} = 0$. However the limited calorimeter resolution is causing relatively wide distributions for these projections. The parallel component u_{\parallel} is sensitive to a possible bias in the hadronic recoil, while the perpendicular u_{\perp} can be used for determination of the resolution discrepancies. The mean and the width of these distributions can depend on different variables, such as a mean number of interactions in an event, hadronic activity, boson P_T^{bos} etc.

It is convenient to use Z boson decays for a hadronic recoil calibration, since its transverse momentum P_T^Z can be determined not only from the hadronic recoil, but also from its decay products. The P_T^Z resolution coming from a lepton reconstruction is 3-4 times more precise, than the one extracted from a hadronic recoil. This allows to treat leptonically reconstructed P_T^Z as a reference P_T of the boson and to compare directly u_{\perp} and u_{\parallel} in the data and the MC. However, a small size of the Z sample in the 2.76 TeV data leads to a high statistics error for these distributions.

The calibration constants can also be derived from W boson decays. In order to exclude a possible bias from the P_T^W mismodelling these calibration constants are derived through the data vs MC comparison of P_T^W independent distributions (such as M_T^W).

In this analysis a combined procedure based on Z and W bosons decays has been used for a hadronic recoil calibration.

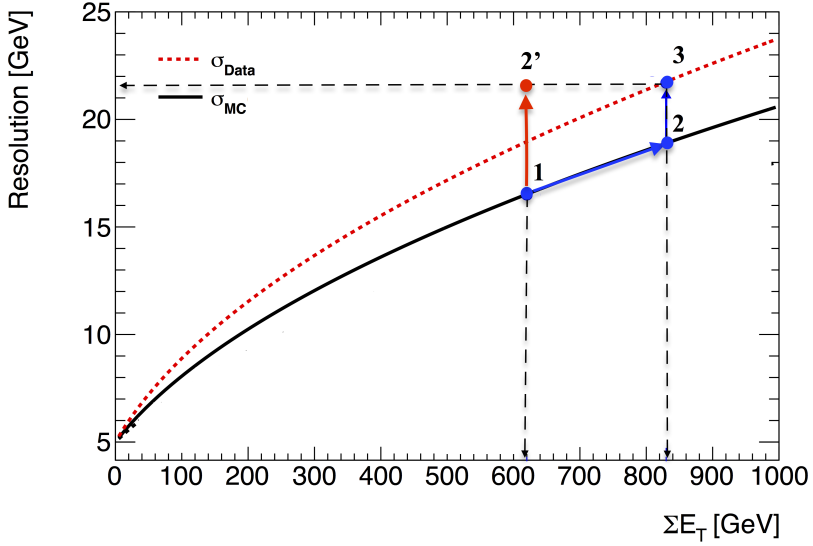


Fig. 11.3: Schematic view of the correction procedure: this figure illustrates the resolution of u_{\perp} as a function of event activity $\sum E_T$. The dotted curve represents data resolution (σ_{data}), the solid black one depicts a nominal MC resolution (σ_{MC}). Blue line from point 1 to point 2 corresponds to the $\sum E_T$ correction discussed in Sec. 11.2.1. The red line from point 1 to point 2' corresponds to a direct correction of the resolution mismodelling discussed in Sec. 11.2.2. Modified from [30]

11.2 Hadronic recoil resolution correction

The event activity plays an important role in the E_T^{miss} reconstruction. Since $\sum E_T$ and the hadronic recoil resolution values are correlated, the possible mismodelling of the event activity can lead to differences between the data and the Monte-Carlo E_T^{miss} resolutions. There are two ways to correct the resolution in the 2.76 TeV data (Fig. 11.3):

- A two step procedure, shown as path 1-2-3 in Fig. 11.3. The first step is to correct $\sum E_T$ distribution to match the data using reweighting of the events. Remaining differences in resolution are corrected at the second step. This method is discussed in Sec. 11.2.1.
- The second order effects on E_T^{miss} coming from $\sum E_T$ modelling are neglected and the resolution differences between data and MC corrected directly. This procedure is shown as the path 1-2' in Fig. 11.3 and described in Sec. 11.2.2.

Both of these methods have been implemented and will be described next.

11.2.1 Event activity correction

The distributions of the event activity $\sum E_T$ are shown in Fig. 11.4. There is a visible shift between data and the MC distribution for both W boson channels. The standard procedure, used in the M_T^W measurement at 7 TeV uses a Smirnov transformation of MC, determined from the $\sum E_T$ and P_T^{bos} distributions in Z events [30]. Distribution of the event activity in the Z-boson events are shown in Fig. 11.5. Since the value of χ^2/NDF is around 1, it is clear that size of the Z sample is not

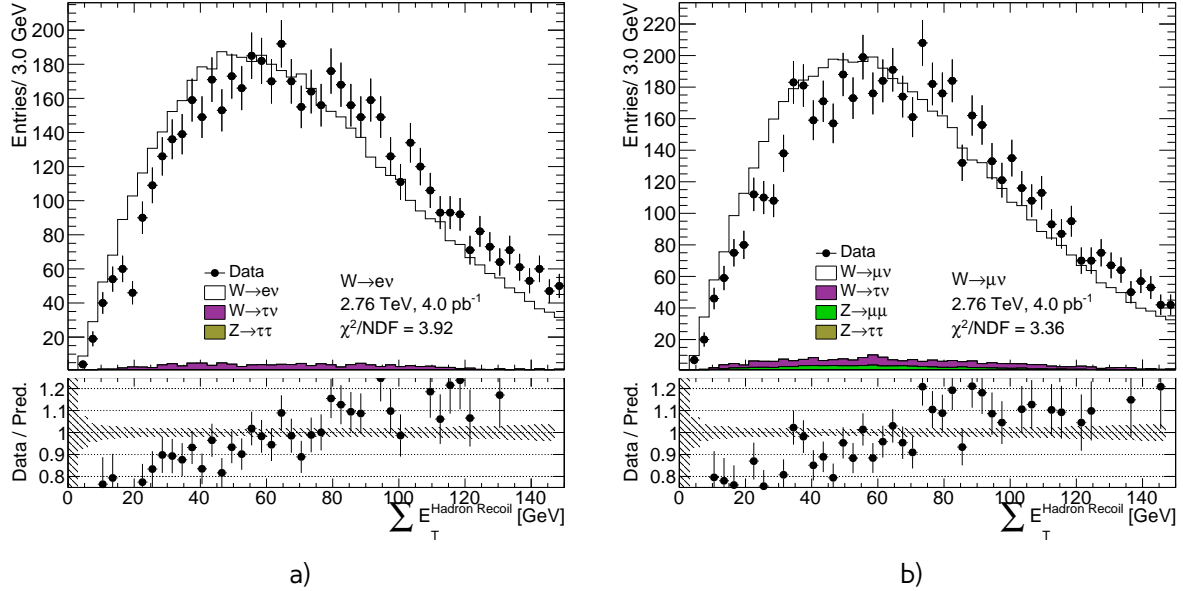


Fig. 11.4: Event activity $\sum E_T$ distribution from a) the $W \rightarrow ev$ selection and b) the $W \rightarrow \mu\nu$ selection. There is a clear sign of the event activity mismodelling in both channels, that should be corrected.

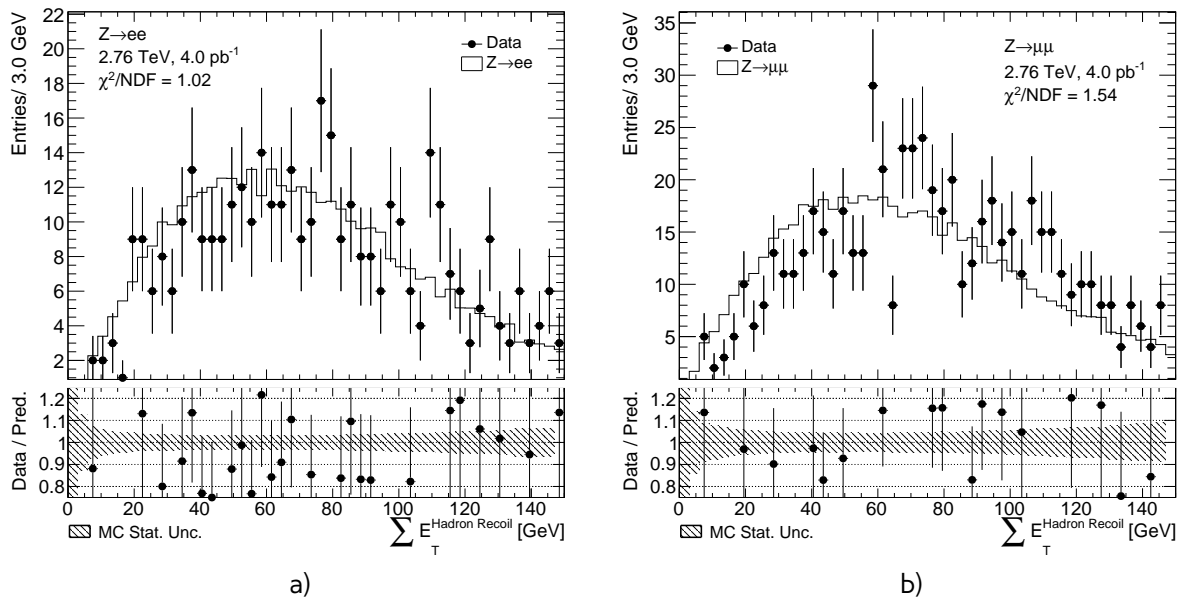


Fig. 11.5: Event activity $\sum E_T$ distribution from a) the $Z \rightarrow ee$ selection and b) the $Z \rightarrow \mu\mu$ selection. The size of the Z sample in 2.76 TeV data is insufficient to correct the mismodelling of the event activity.

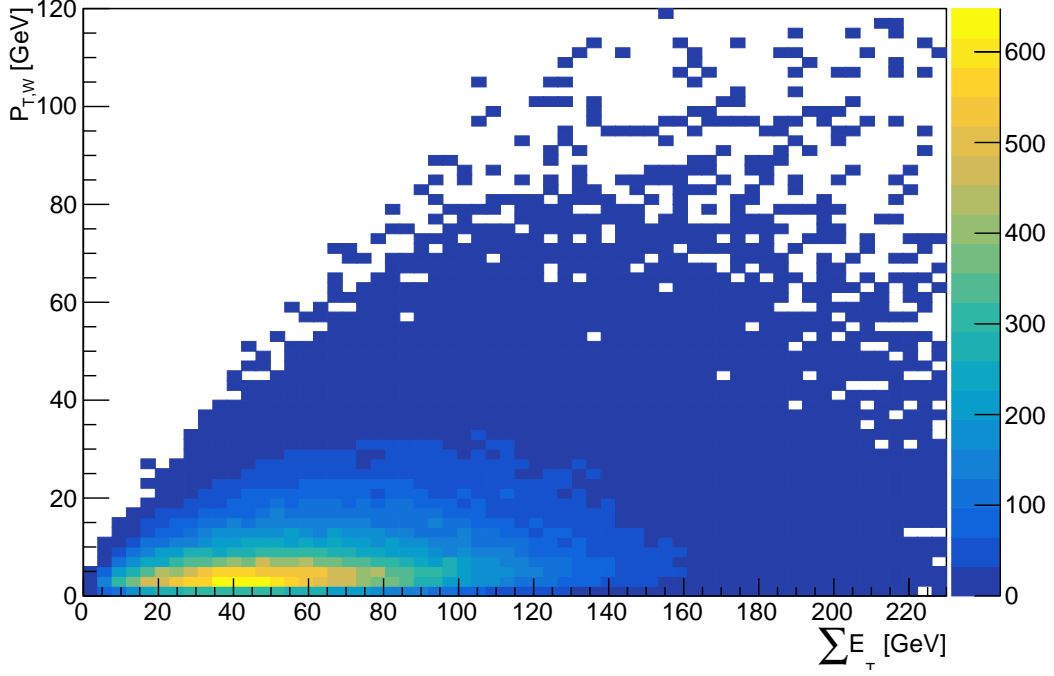


Fig. 11.6: Distribution of event activity $\sum E_T$ vs truth transverse momentum of the W boson P_T^W *truth* in the $W^+ \rightarrow e\nu$ MC sample.

1158 sufficient for this procedure for both $\sum E_T$ and P_T^{bos} distributions. This motivates a choice of the
 1159 $\sum E_T$ reweighting constants determination from the W-boson sample.

The event activity $\sum E_T$ is correlated to the truth transverse momentum of the boson, as shown in Fig. 11.6, so in order to avoid a bias from changing P_T^W spectrum, reweighting constants are derived in bins of reconstructed boson momentum $P_T^{W,rec}$. Inside each $P_T^{W,rec}$ bin the reweighting constants are calculated as:

$$SF^{channel} = \frac{\sum E_T^{data,selection}}{\sum E_T^{MC,no\ cuts}}, \quad (11.3)$$

1160 where $\sum E_T^{data,selection}$ is a $\sum E_T$ distribution inside a given $P_T^{W,rec}$ after the full event selection. In order
 1161 to reduce systematic uncertainty from this value, a combination of $W \rightarrow e\nu$ and $W \rightarrow \mu\nu$ events
 1162 is used.

1163 Second term $\sum E_T^{MC,no\ cuts}$ stands for $\sum E_T$ distribution in MC before any selection. The scale factors
 1164 are determined separately for each signal MC for W boson decays, in order to leave the total number
 1165 of events in the the MC after the correction unchanged. Transverse boson momentum binning is
 1166 chosen so that there is approximately the same number of events per bin. The total number of
 1167 $P_T^{W,rec}$ bins is 6. The scale factor are applied as a reconstructed weight on MC.

1168 The correction factors for two example $P_T^{W,rec}$ bins are shown in Fig.11.7. Resulting reweighting
 1169 constants for $W \rightarrow e\nu$ and $W \rightarrow \mu\nu$ MC samples are shown in Fig. 11.8. This method allows to
 1170 leave the reconstructed transverse momentum of the boson nearly unmodified and introduces only
 1171 a small change in a the truth boson spectrum, as shown in Fig. 11.10.

1172 There are two possible sources of the uncertainties of this correction: systematical, coming from

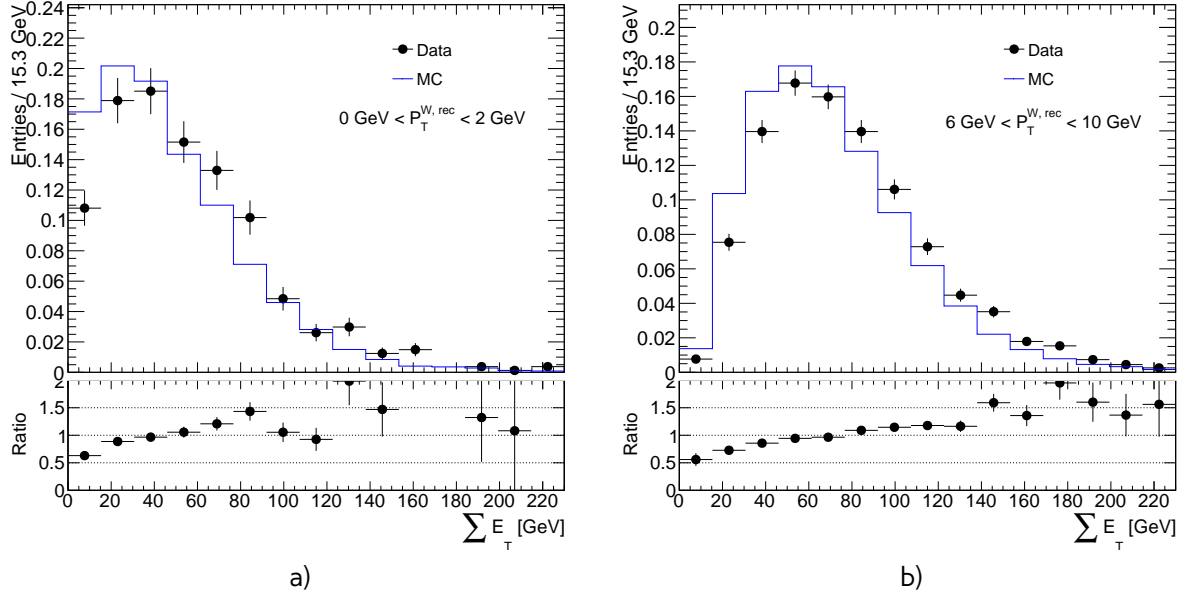


Fig. 11.7: Distribution of $\sum E_T$ for the different $p_T^{W,\text{rec}}$ bins for $W^+ \rightarrow e\nu$ MC sample

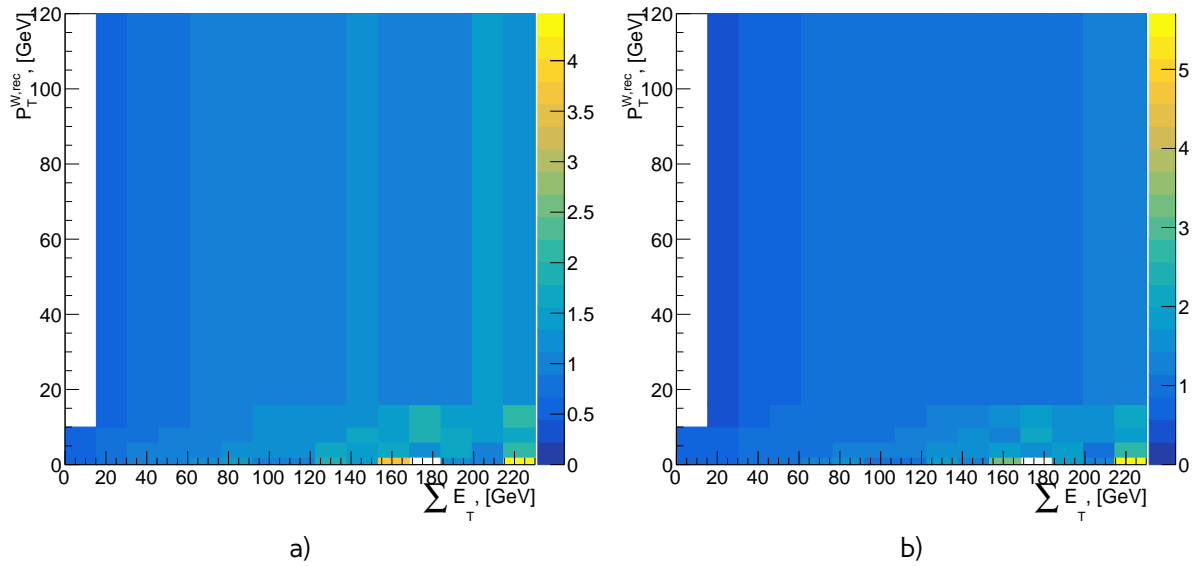


Fig. 11.8: Distribution of $\sum E_T$ reweighting constants derived for a) $W^+ \rightarrow e\nu$ and b) $W^+ \rightarrow \mu\nu$ MC sample.

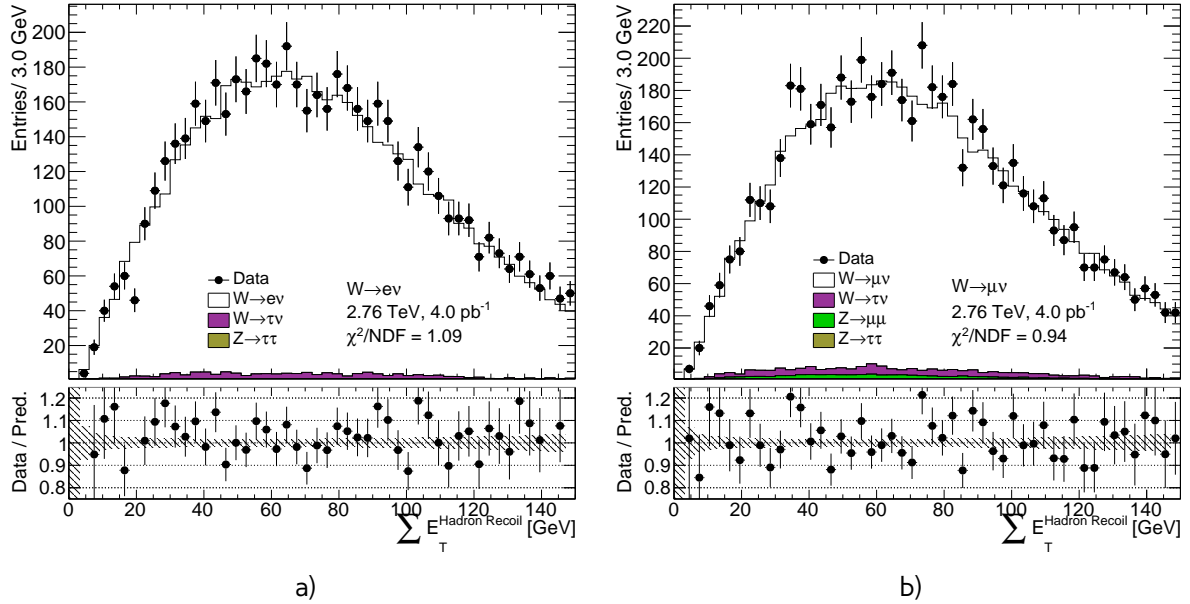


Fig. 11.9: Event activity $\sum E_T$ distribution from a) the $W \rightarrow e\nu$ selection and b) the $W \rightarrow \mu\nu$ selection after $\sum E_T$ correction.

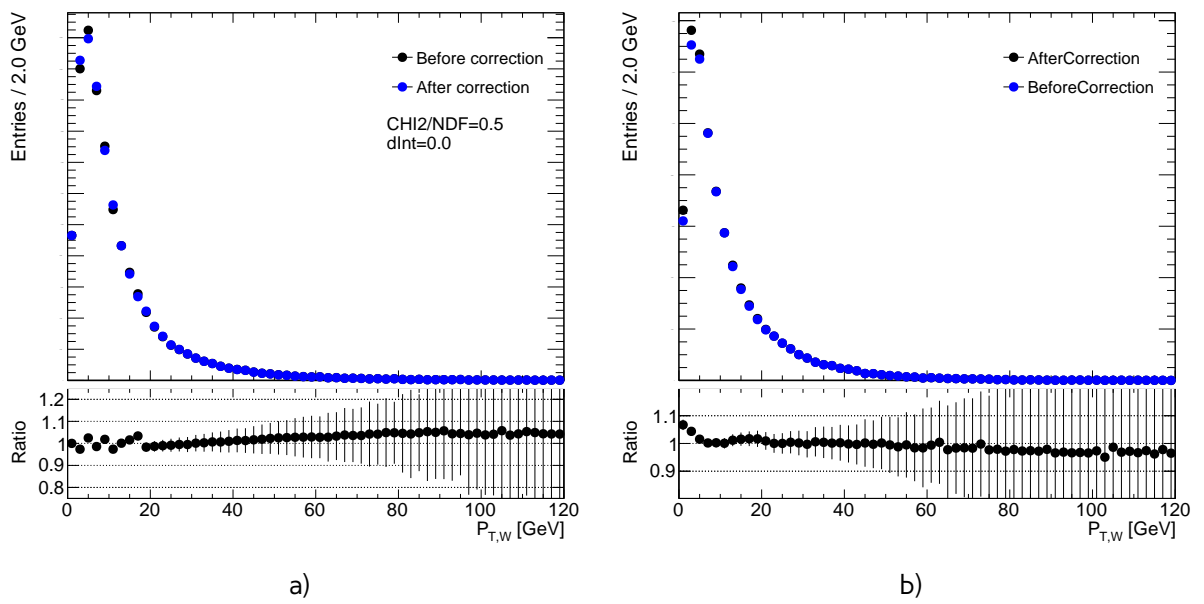


Fig. 11.10: Effect of the $\sum E_T$ reweighting on a) reconstructed transverse momentum of the boson and b) truth transverse momentum of the boson in $W^+ \rightarrow e\nu$ MC sample.

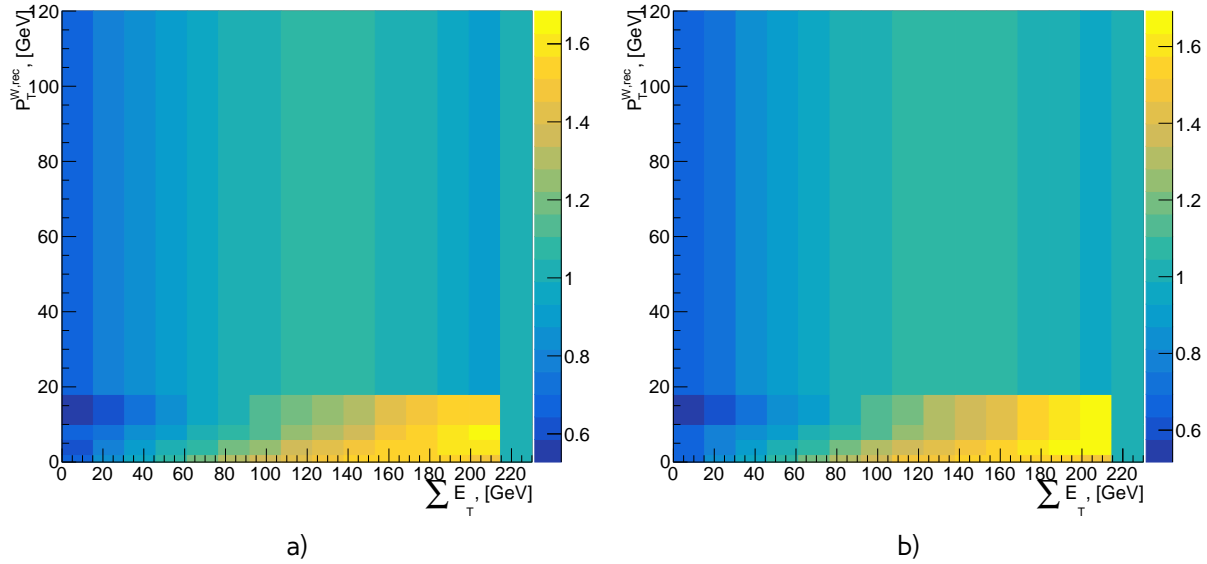


Fig. 11.11: Distribution of $\sum E_T$ reweighting constants derived for a) $W^+ \rightarrow ev$ and b) $W^+ \rightarrow \mu\nu$ MC sample using polynomial order 2 approximation.

1173 the method itself and a statistical, coming from the limited data statistic. The methods of their
1174 determination and an effect of the correction on C_W factors will be discussed.

1175 Systematic error estimation

Systematic error on this reweighting can be estimated approximating the data to MC ratio as a function of $\sum E_T$ inside each $P_T^{W,rec}$ bin with a polynomial degree 2 or 1. This method allows also to neglect effects of the data fluctuations, especially for the high $\sum E_T$ regions with low statistics, as it could be seen in Fig. 11.8. Because of the low statistics for $\sum E_T > 220$ GeV the ratio in the last bins has been set to 1 and this region haven't been included in the polynomial fit. The total reweighting constants obtained from this procedure are shown in Fig. 11.11.

1182 Statistical error estimation

1183 Statistical error on the $\sum E_T$ reweighting is estimated using Toy MC method, described in Chap.14
 1184 from the polynomial order 2 approximation, since the uncertainty of the fit parameters obtained
 1185 from the fit includes statistical error of data points. The fit parameters of the polynomials are varied
 1186 inside each $p_T^{W_{rec}}$ bin within their fit uncertainties as in Eq. 14.3.

Because of the possible correlations between the fit parameters, a multivariate gaussian distribution has been used. It is calculated as:

$$p(x; \mu, \Sigma) = \frac{1}{(2\pi)^{n/2} |\Sigma|^{1/2}} \exp\left(-\frac{1}{2}(x - \mu)^T \Sigma^{-1} (x - \mu)\right), \quad (11.4)$$

where $\mu \in R^n$ is obtained from the fit parameters vector and Σ is $n \times n$ covariance matrix of these parameters, $(x - \mu)^T$ is a transpose of the vector $(x - \mu)$. In case of the polynomial order two $n=3$.

Table 11.1: Effect of $\sum E_T$ correction on C_W for different channels and methods

Channel	δC_W no approximation	δC_W polynomial order 2	δC_W polynomial order 1	δC_W Toy MC
$W^+ \rightarrow e^+ \nu$		0.39%	0.31%	0.03%
$W^- \rightarrow e^- \nu$		0.33%	0.22%	0.03%
$W^+ \rightarrow \mu^+ \nu$		-0.20%	-0.28%	0.03%
$W^- \rightarrow \mu^- \nu$		-0.21%	-0.27%	0.03%

1189 For statistic error determination total number of 25 toys have been used. Total error is calculated
 1190 using Eq.14.4.

1191 Effect of the $\sum E_T$ correction on cross-section

1192 The effect of the $\sum E_T$ correction on cross-section is estimated by applying different correction
 1193 factors on MC. The error is estimated by calculating difference in C_W using On/Off method (see
 1194 Chap. 14). The overall effect of the $\sum E_T$ correction for different methods is summarized in Tab. 11.1.
 1195 Statistical error, estimated using Toy MC method is negligible. The systematic error is calculated as
 1196 a difference between C_W for a two methods and is considered to be small, compared to the overall
 1197 effect.

1198 The sign of the effect differs for different W channels, that cannot be explained by a systematic
 1199 error coming from the method or a data statistics. This effect also cannot be explained from a
 1200 physical point of view, since we expect a similar errors for both lepton flavors, so it was decided not
 1201 to use this corrections in a final analysis.

1202 11.2.2 Resolution corrections using Z events

1203 Another way to check resolution effects is to study u_\perp and $u_\parallel - p_T^Z$ distributions in events containing
 1204 Z boson. This correction assumes, that any resolution mismodelling reflects discrepancies in the $\sum E_T$
 1205 distribution, while the difference in the resolution at a given $\sum E_T$ is subleading.

Difference in hadronic recoil resolutions $d\sigma$ between the data and the MC can be quantified by value:

$$d\sigma = \sqrt{\sigma_{data}^2 - \sigma_{MC}^2}, \quad (11.5)$$

where σ_{data} and σ_{MC} are the RMS of these distributions. This value is affected by the statistical uncertainty of data standard deviation, that in case of the distributions close to normal can be calculated as [31]:

$$\sigma(\sigma_{data}) = \frac{\sigma_{data}}{\sqrt{2N}}, \quad (11.6)$$

1206 where N is the number of entries in histogram. The distributions of u_\perp and $u_\parallel - p_T^Z$ in $Z \rightarrow ee$,
 1207 $Z \rightarrow \mu\mu$, $Z \rightarrow ll$ events are shown in Fig. 11.12. The typical resolution uncertainty for data is
 1208 around 0.1 GeV for all distributions, while the the difference in resolution is 1.0 GeV and higher, that
 1209 is a clear indication of mismodelling of hadronic recoil resolution in the Monte-Carlo. The overall
 1210 difference in resolutions is consistent between u_\perp and $u_\parallel - p_T^Z$ distributions, however it depends

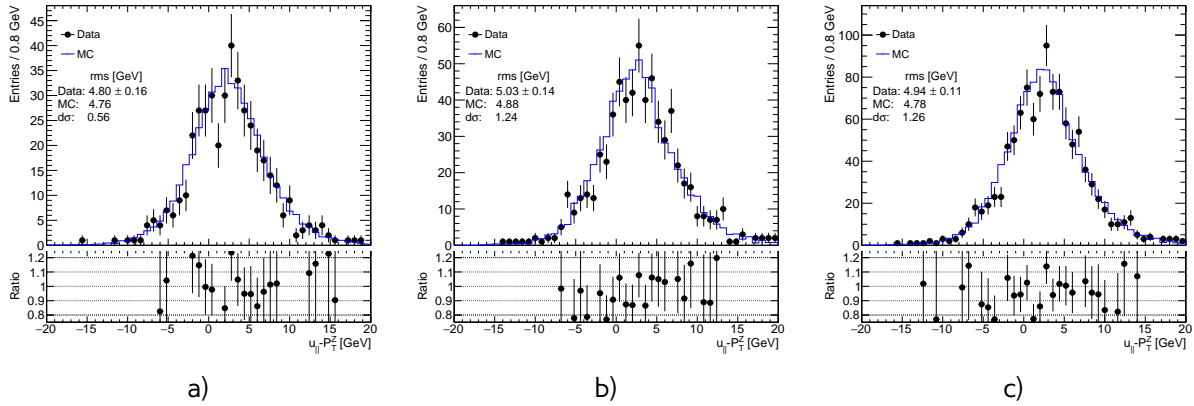


Fig. 11.12: Parallel hadronic recoil component distribution from a) the $Z \rightarrow ee$ selection b) $Z \rightarrow \mu\mu$ selection and c) $Z \rightarrow ll$ selection. The expected contribution from signal is estimated with Monte Carlo simulation, other background sources are considered negligible.

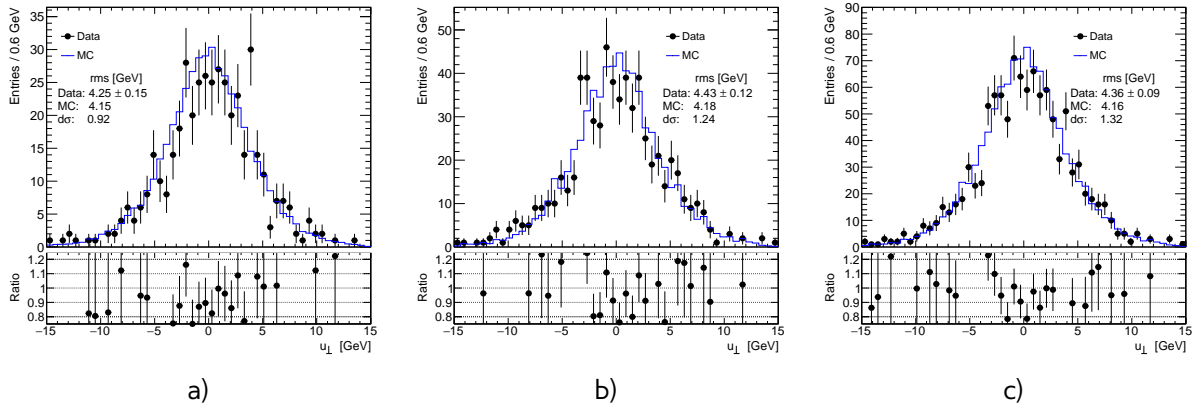


Fig. 11.13: Perpendicular hadronic recoil component distribution from a) the $Z \rightarrow ee$ selection b) $Z \rightarrow \mu\mu$ selection and c) $Z \rightarrow ll$ selection. The expected contribution from signal is estimated with Monte Carlo simulation, other background sources are considered negligible.

1211 on a lepton flavor, isolation and identification criteria. For a correction it was decided to choose the
 1212 value, obtained from combined $Z \rightarrow ll$ channel, where $d\sigma = 1.3$ GeV.

The resolution is corrected by a smearing, using a Gaussian distribution, of each component of the hadronic recoil in Monte-Carlo:

$$u'_{||} = u_{||} + Gaus(0, d\sigma) \quad (11.7)$$

$$u'_{\perp} = u_{\perp} + Gaus(0, d\sigma), \quad (11.8)$$

1213 Effect of the smearing correction on cross-section

1214 Effect of smearing correction is estimated using On/Off method (Chap. 14) on a C_W factor. Scan in
 1215 a big range of the parameter $d\sigma$ up to 2.0 GeV (Fig. 11.14) have showed, that C_W becomes smaller
 1216 with growth of the smearing parameter $d\sigma$. However, due to the random nature of the correction,
 1217 the C_W fluctuates within the mean value.

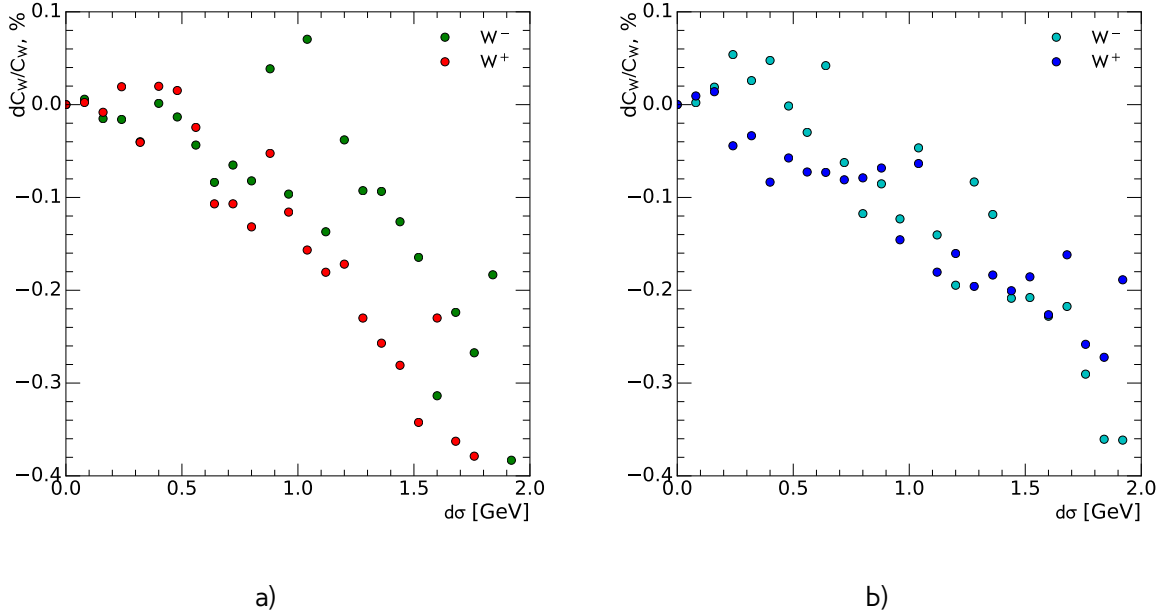


Fig. 11.14: Effect on a C_W from hadronic recoil resolution correction with different $d\sigma$ for a) $W \rightarrow e\nu$
b) $W \rightarrow \mu\nu$ channel.

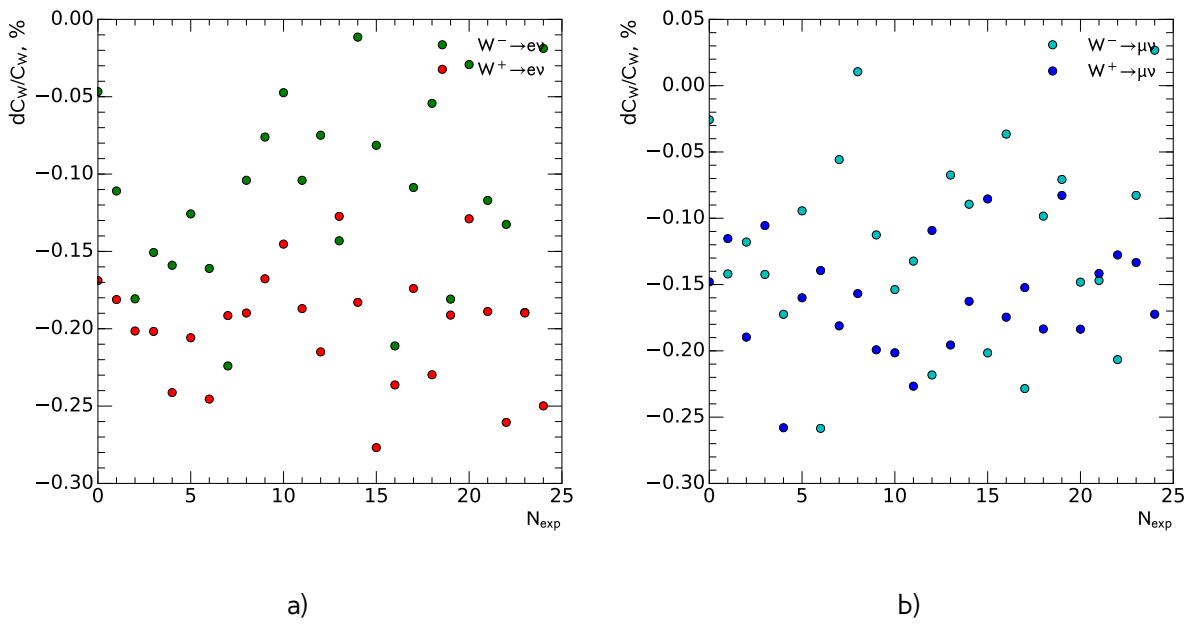


Fig. 11.15: Effect on a C_W from hadronic recoil resolution correction with $d\sigma = 1.3$ GeV for a) $W \rightarrow e\nu$
b) $W \rightarrow \mu\nu$ channel for repeated experiments. The overall systematic uncertainty of this
correction is estimated as the mean value of dC_W .

Table 11.2: Effect of smearing correction on a C_W for a different channels. The error of the mean value is estimated using the Eq. 11.11

Channel	δC_W	rms
$W^+ \rightarrow e^+\nu$	-0.20±0.4%	0.04%
$W^- \rightarrow e^-\nu$	-0.11±0.2%	0.06%
$W^+ \rightarrow \mu^+\nu$	-0.16±0.3%	0.04%
$W^- \rightarrow \mu^-\nu$	-0.12±0.2%	0.07%

Systematic error have been estimated by repeating correction on the same sample 25 times (Fig. 11.15). Table 11.2 presents the mean effect on C_W together with the rms of the distribution. Overall systematic effect is below 0.2% for each analysis channel, that makes it negligible compared to the statistics uncertainty in W samples (Chap. 14).

11.3 Hadronic recoil bias correction

As it was mentioned before, the hadronic recoil value in Monte Carlo could be shifted in a respect to data because of the mismodelling of underlying event, calorimeter cluster responses, etc. Since the value of hadronic recoil affects the E_T^{miss} distribution this discrepancy should be corrected. It could be done by applying the correction factor HR_{SF} on a hadronic recoil in Monte-Carlo sample as:

$$u_{\parallel}^{cor} = u_{\parallel} \cdot HR_{SF}, \quad (11.9)$$

where u_{\parallel} is a parallel component in the respect to the true boson direction of hadronic recoil.

The procedure of hadronic recoil bias determination uses a parameter scan through the wide range of the possible HR_{SF} values. It is assumed, that the "real" value of the bias is corresponding

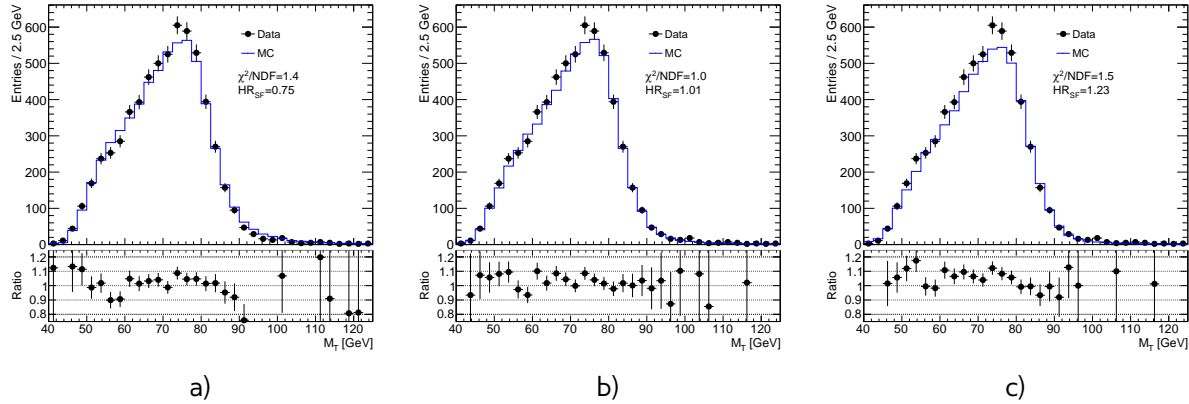


Fig. 11.16: Transverse mass distribution from the $W \rightarrow e\nu$ selection for different hadronic recoil scales: a) $HR_{SF}=0.75$ b) $HR_{SF}=1.0$ c) $HR_{SF}=1.23$. The expected contributions from signals and backgrounds are estimated with Monte Carlo simulation, except for a QCD background, that is not included.

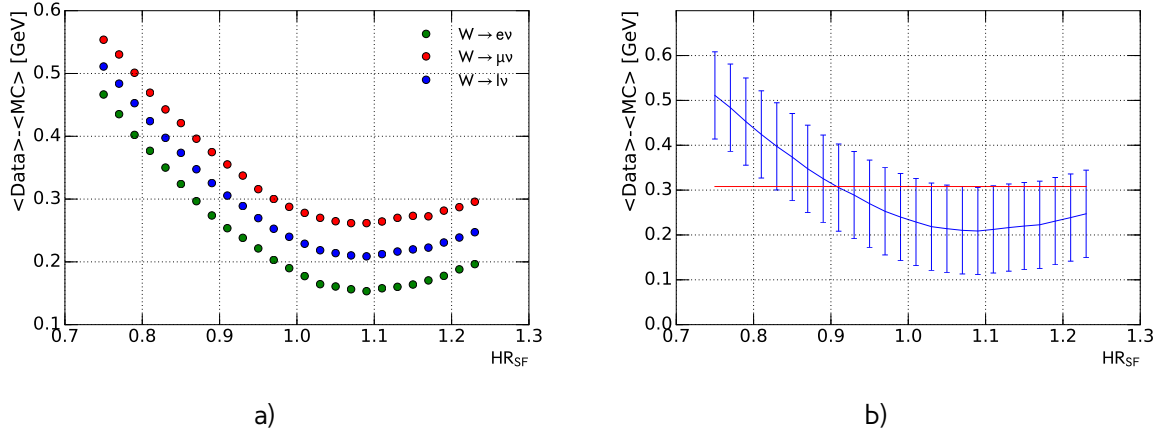


Fig. 11.17: Distribution of a difference in a mean transverse mass $\langle M_T^W \rangle$ between data and MC as a function of the hadronic recoil scale HR_{SF} a) for different W boson channels and b) for combined $W \rightarrow l\nu$ selection. Errors for each point are calculated as a standard error of mean (Eq. 11.11). Below red line is the 68% CL on the best HR_{SF} correction factor. The expected contributions from signals and backgrounds are estimated with Monte Carlo simulation, except for a QCD background, that is not included.

to a best agreement between data and MC and therefore can be obtained through the fit of χ^2 of some distribution as:

$$\chi^2 = \frac{(HR_{SF} - sf_{best})^2}{\sigma_{sf}^2} + \chi_0^2, \quad (11.10)$$

where sf_{best} is the best scale factor, σ_{sf} is a statistical error of this parameter and χ_0^2 is a value of χ^2 in a minimum.

In the following sections methods of hadronic recoil bias determination using W and Z events will be discussed.

11.3.1 Bias determination from M_T^W distribution

Since the W boson transverse momentum cannot be measured in two different ways in order to provide the reference for a hadronic recoil scale, determination of the hadronic recoil bias should use the distributions, that are not sensitive to the true P_T^W spectrum, to exclude the effect of possible P_T^W mismodelling in MC. One of the optimal choices is the M_T^W distribution.

The transverse mass distribution for a different correction parameters HR_{SF} is shown on a Fig. 11.16. The expected contributions from signal and backgrounds are estimated with Monte Carlo simulation, except for a multijet background, because its shape and number of events depends on a hadronic recoil scale and thus needs to be recalculated for each value of HR_{SF} .

One of the possible methods to determine the correction factor is to use a difference in the mean of the transverse mass distributions in data and MC (Fig. 11.17). Statistical error on a correction factor is considered a dominating one and estimated as a standard error of a mean $\sigma(\langle M_T^W \rangle)$, calculated as:

$$\sigma\left(\langle M_T^W \rangle\right) = \frac{\sigma(M_T^W)}{\sqrt{N}}, \quad (11.11)$$

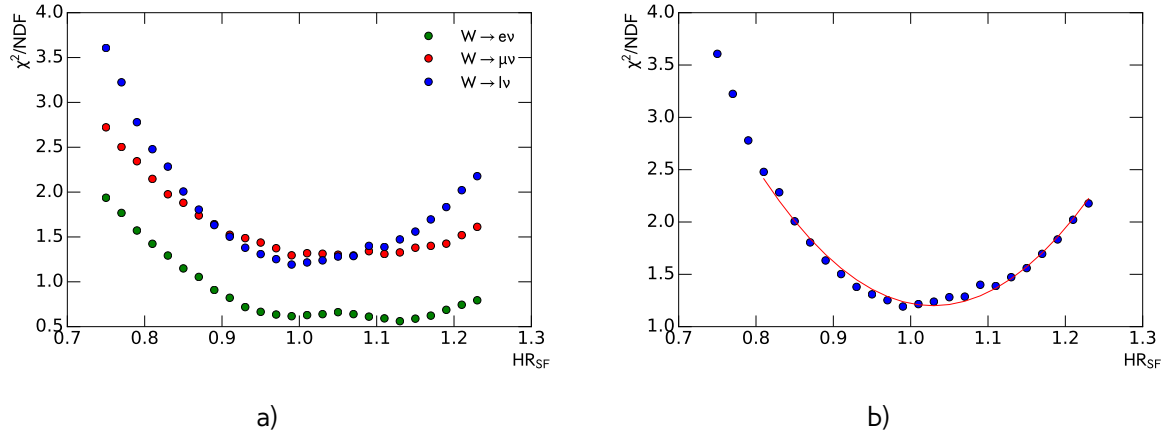


Fig. 11.18: Distribution of χ^2/NDF between data and MC for transverse mass $\langle M_T^W \rangle$ as a function of hadronic recoil scale HR_{SF} a) for different W boson channels. b) for combined $W \rightarrow l\nu$ selection. Fit result is shown by the red line. The expected contributions from signal and backgrounds are estimated with Monte Carlo simulation, except for a QCD background, that is not included.

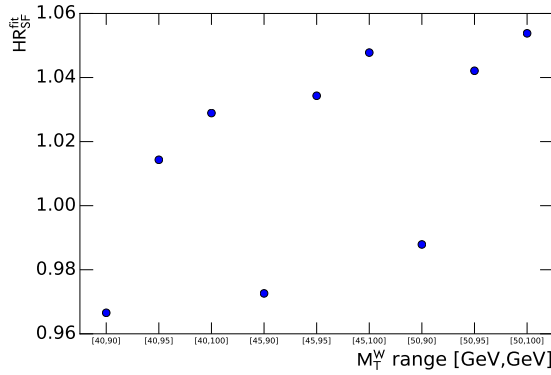


Fig. 11.19: Values of hadronic recoil biases obtained from the fit for events from combined $W \rightarrow l\nu$ selection as a function of fit range. The expected contributions from signals and backgrounds are estimated with Monte Carlo simulation, except for a QCD background, that is not included.

1237 where $\sigma(M_T^W)$ is a standard deviation of M_T^W distribution and N is a total number of events used.
 1238 The minimal difference is obtained at $HR_{SF} = 1.1 \pm 0.2$. The precision of this method is low, and it
 1239 is mainly used as a cross-check for other methods.

1240 Distribution of χ^2 for a scan of possible values of HR_{SF} for different W channels is shown in
 1241 a Fig. 11.18 a). Because of a possible mismodelling of the tail M_T^W distribution, events with $M_T^W >$
 1242 100 GeV are not included in a χ^2 calculation. There is a small peak visible in the χ^2 distribution for
 1243 events from $W \rightarrow e\nu$ selection, that can be assumed to come from the missing QCD background
 1244 contributions. Hadronic recoil bias parameters are determined through the fit of χ^2 distribution in
 1245 combined $W \rightarrow l\nu$ channel using the function from Eq. 11.10. The resulting bias is $HR_{SF} = 1.02$,
 1246 with the statistical error 0.06.

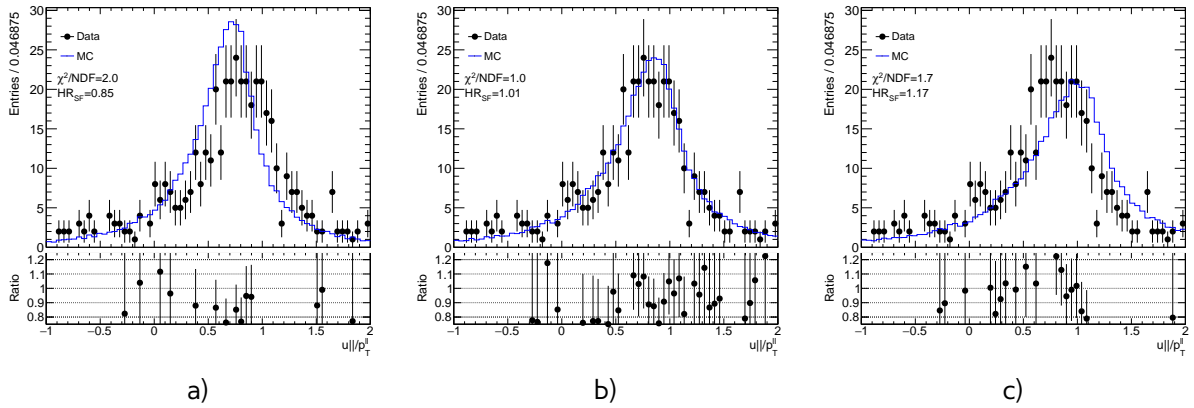


Fig. 11.20: Parallel hadronic recoil component u_{\parallel} from the $Z \rightarrow ee$ selection for different hadronic recoil scales: a) $HR_{SF}=0.75$ b) $HR_{SF}=1.1$ c) $HR_{SF}=1.23$. The expected contribution from signal is estimated with Monte Carlo simulation, other background sources are considered negligible.

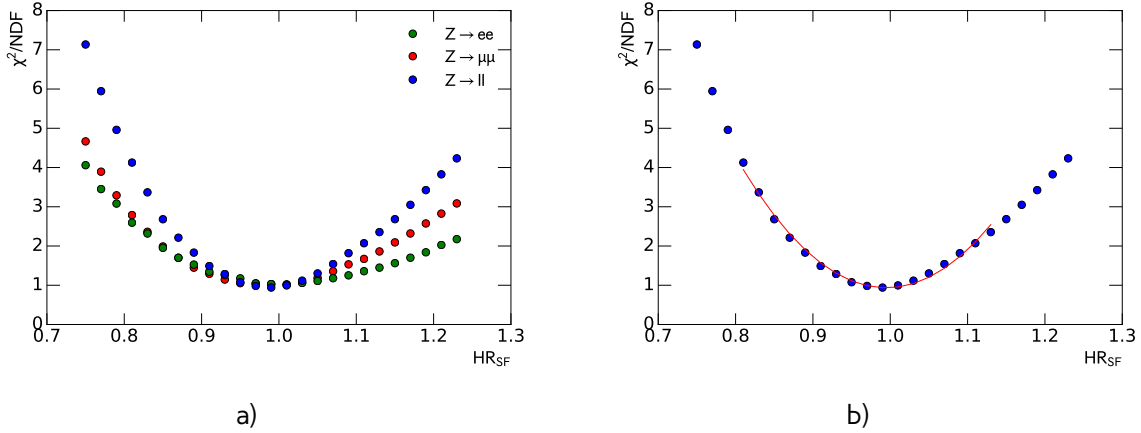


Fig. 11.21: a) Distribution of χ^2 between data and MC for $\frac{u_{\parallel}}{p_T^2}$ distribution as a function of hadronic recoil scale HR_{SF} for a) different Z boson channels. b) for combined $Z \rightarrow ll$ selection. Fit results are shown by a red line. The expected contribution from signal is estimated with Monte Carlo simulation, other background sources are considered negligible.

1247 Additionally, a cut on M_T^W lower value may be used to reduce the multijet background contamination.
 1248 The M_T^W range introduces a source of the systematic uncertainty in the hadronic recoil scale
 1249 determination. It is estimated by repeating the fit for different M_T^W lower and upper values, as shown
 1250 in Fig. 11.19. Fit range systematic error calculated as an RMS of the obtained values and is 0.03. The
 1251 final result for this method is $HR_{SF} = 1.02 \pm 0.07$.

1252 11.3.2 Bias determination using u_{\parallel} distribution

1253 Similarly to the W channel, the scale correction in the Z sample can be determined from the HR_{SF}
 1254 scan of the $\frac{u_{\parallel}}{p_T^2}$ distribution, as shown in Fig. 11.20. All of the backgrounds sources are considered
 1255 negligible in this case. Results of the χ^2 test for data and MC in different channel are shown in Fig.

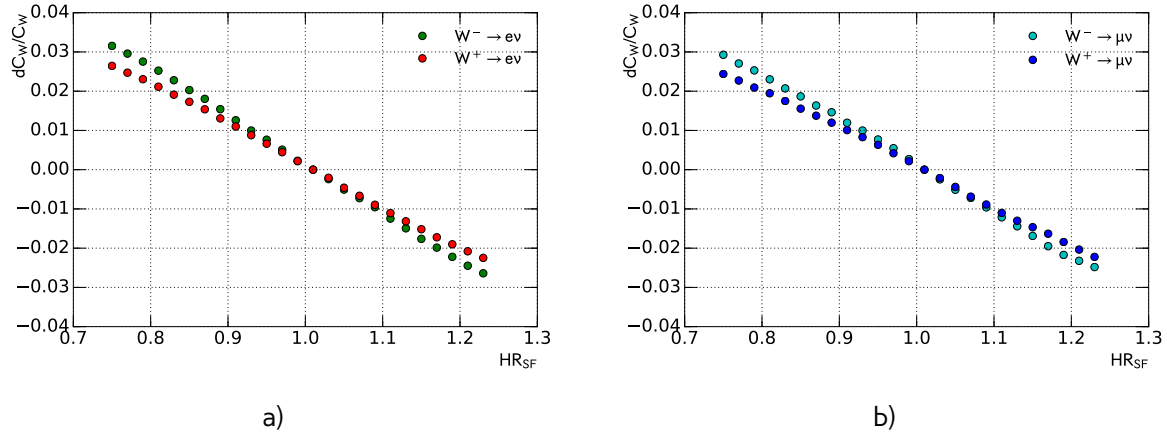


Fig. 11.22: Effect on a C_W for a different $d\sigma$ for a) $W \rightarrow e\nu$ b) $W \rightarrow \mu\nu$ channel

1256 11.21. A fit of the combined $Z \rightarrow ll$ distribution gives the most precise estimation of the hadronic
 1257 recoil bias $HR_{SF} = 1.00 \pm 0.01$. Since there is no choice of the range and dependency on P_T^{bos}
 1258 modeling, there is just one statistical source of uncertainty.

1259 11.3.3 Systematic uncertainty estimation

Table 11.3: Hadronic recoil bias determination results and errors for different methods.

Method	SF	error
Mean M_T^W	1.10	0.2
$M_T^W \chi^2$	1.01	0.07
$u_{\parallel} \chi^2$	1.00	0.014

1260 Results on a hadronic scale factors and its errors are shown in a Table 11.3. The results are con-
 1261 sistent within one sigma. As a final result it was decided to choose HR_{SF} determined from $Z \rightarrow ll$
 1262 selection as the are established with smallest uncertainty/ Scale factors extracted with other meth-
 1263 ods are used as a cross-check.

1264 Effect of the hadronic recoil bias correction for different bias scale factors presented in Fig. 11.22.
 1265 Systematic error, coming from the bias correction is estimated using offset method (see Chap. 14).

1266 11.4 Summary on hadronic recoil systematics

1267 Because of the problems with data vs MC comparison it was decided to use a hadronic recoil al-
 1268 gorithm of E_T^{miss} reconstruction. Because of the differences in operation conditions the calibration
 1269 of hadronic recoil must be determined directly from 2.76 TeV data. The limited statistics of the Z
 1270 sample does not allow to use the standard procedure, used for the M_T^W measurement at 7 TeV, so
 1271 the new methodology was developed.

1272 The hadronic recoil calibration can be divided into two parts: the correction of resolution and the
 1273 bias correction. The hadronic recoil resolution have been corrected using the following methods:

Table 11.4: Hadronic recoil bias systematics for different W boson channels.

Systematic source	$W^+ \rightarrow e^+\nu$	$W^- \rightarrow e^-\nu$	$W^+ \rightarrow \mu^+\nu$	$W^- \rightarrow \mu^-\nu$
Hadronic recoil resolution	-0.2%	-0.11%	-0.16%	-0.12%
Hadronic recoil scale	0.21%	0.20%	0.23%	0.24%

- Event activity correction through the reweighting of $\sum E_T$ distribution. Different methods of the data/MC ratio parametrization have been developed and showed the consistent result. However, this method gives a unphysical difference between electron and muon channels, that cannot be accounted for the data statistics, so it was decided to drop this method.
- Smearing correction of the hadronic recoil. This method uses the Z sample to determine the difference in resolutions of the hadronic recoil components. The overall effect of these correction was estimated by repeating the smearing 25 times and consistent between electron and muon channels

The bias of hadronic recoil was estimated on W and Z events using 3 methods:

- Difference in the mean of the M_T^W distributions in data and MC. This method gives the highest uncertainty and used as a cross-check for other results
- Through the scans of the hadronic recoil scale effect on χ^2 in data vs MC M_T^W distributions. Error on this method is dominated by the statistics
- Through the scans of the hadronic recoil scale effect on χ^2 in data vs MC $\frac{u_{||}}{p_T^H}$ distributions. Despite the small size of the Z boson sample, this distribution has the biggest sensitivity to the hadronic recoil scale. It was decided to use this result and its error as a final result.

The results are agreeing between channels within 1 sigma.

The corresponding error sources for the hadronic recoil calibration have been estimated and summarised in the Tab. 11.4. The overall error on E_T^{miss} is around 0.3 % for all W-boson channels and can be considered a subdominant.

12

Chapter 12

Background estimation

12.1 QCD background estimation	94
12.1.1 Template selection	95
12.1.2 Methodology of the template sample normalization	95
12.1.3 Systematic uncertainty from the multi-jet background estimation	97
12.2 Background-subtracted W and Z candidate events	99

After the event selection described in Chap. 9 the background contribution is around 4% for W-analysis and 0.2% for Z analysis (which with this statistics is negligible). Main backgrounds for W analysis are coming from:

- Processes with τ lepton, misidentified as an electron or muon + missing energy from neutrino
- Z decays with one missing lepton.
- QCD processes. In electron channel these are mostly jets faking electrons, while in the muon channel it consists mainly of a real muons produced in decays of heavy-flavor mesons.

Most of the backgrounds are estimated using MC. They are normalized using highest cross-section order available. The total list of simulated backgrounds and its cross-section is shown in a Table 12.1. The QCD background is estimated using data driven method.

Table 12.1: Background processes with their associated cross sections and uncertainties (if given). The quoted cross sections are used to normalise estimates of expected number of events

Process	$\sigma \cdot BR(\pm unc.)$ [pb]	Order
$W^+ \rightarrow l\nu$	2116(± 41)	NNLO
$W^- \rightarrow l\nu$	1267(± 24)	NNLO
$Z \rightarrow ll$	303(± 6)	NNLO
$Z \rightarrow \tau\tau$	303	LO
$t\bar{t}$	7.41	LO
WW	0.6	LO
ZZ	0.7	LO
WZ	0.2	LO

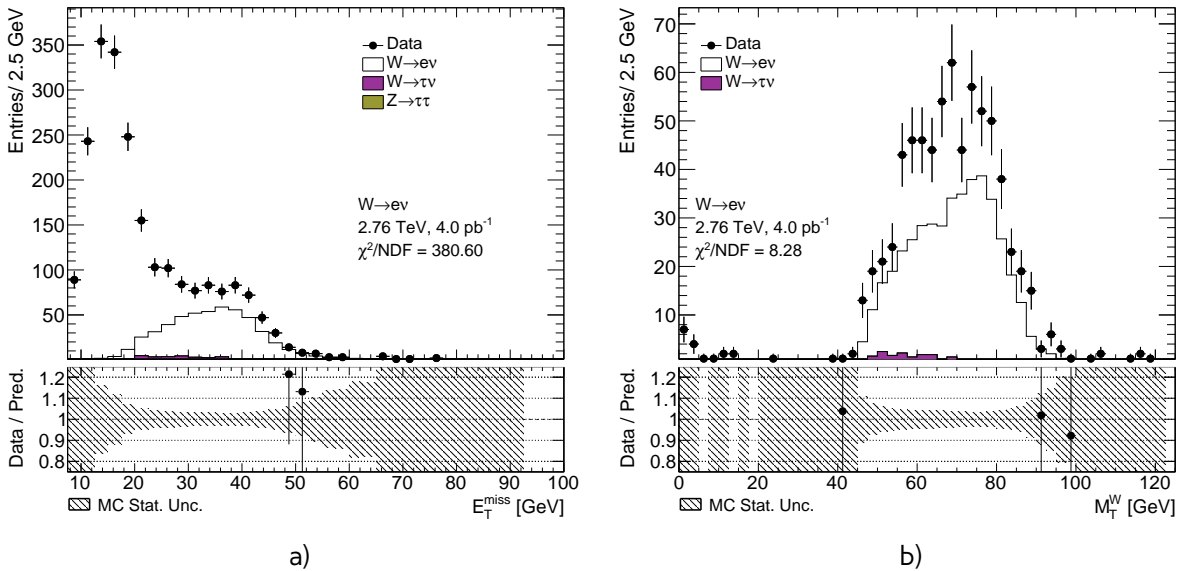


Fig. 12.1: Distribution for a) missing transverse energy E_T^{miss} b)mass transverse M_T^W from the QCD template selection for $W \rightarrow e\nu$ events

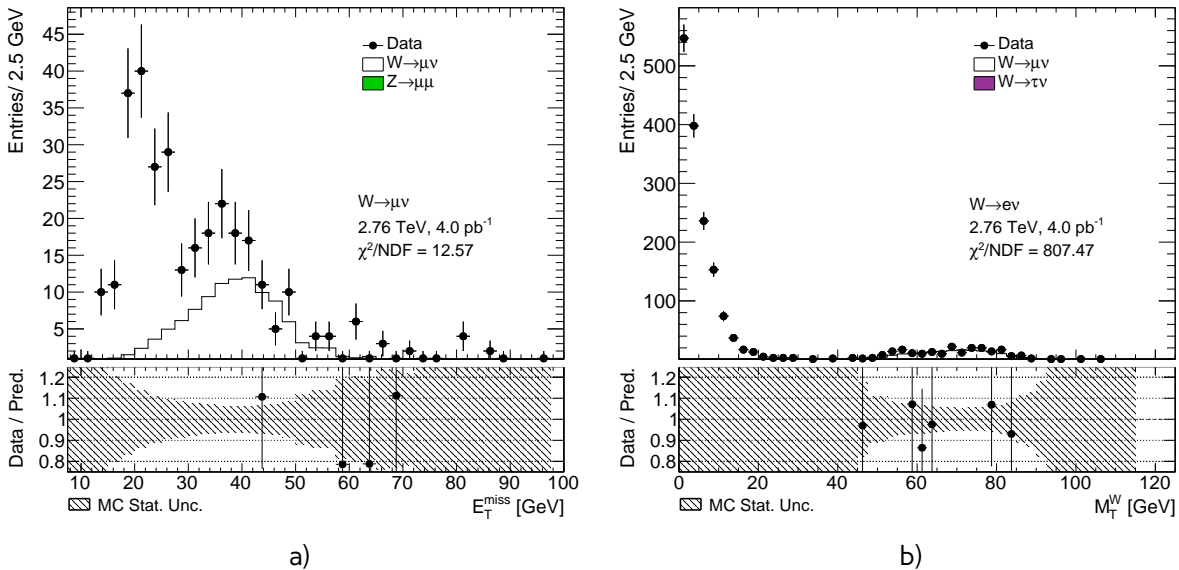


Fig. 12.2: Distribution for a) missing transverse energy E_T^{miss} b)mass transverse M_T^W from the QCD template selection for $W \rightarrow \mu\nu$ events

12.1 QCD background estimation

There is a small probability, that a jet can fake W-boson decay with isolated lepton and E_T^{miss} through the energy mismeasurement in the event. Event selection is suppressing this type of background, but not fully eliminating it. Due to a large jet production cross-section and complex composition, generation of MC events becomes impractical. This is why data driven technique for QCD background estimation have been used. In our case contribution from the QCD background in the Z sample is negligible(Fig. 13.15), so it is estimated just for $W \rightarrow e\nu$ and $W \rightarrow \mu\nu$ processes.

1323 Data driven method allows to have model independent predictions with small statistical uncertainty.
 1324 This method is using *QCD* enriched region, where signal events are suppressed. This is usually done
 1325 by reversing identification or isolation criteria. It is assumed, that shape of the *QCD* background
 1326 stays the same in the signal region. Normalization can be derived in a control region through the
 1327 template fit.

1328 This section describes method of *QCD* background determination, that have been used in 2.76
 1329 TeV data.

1330 12.1.1 Template selection

1331 A study have been performed to determine appropriate template selection. Because of the origin
 1332 of the *QCD* backgrounds, missing transverse energy E_T^{miss} should be smaller in background sample,
 1333 that in a signal region. Releasing E_T^{miss} cut allows to gain a bigger statistics for a *QCD* template.
 1334 Another possibility is to relax the transverse mass M_T^W cut. Most of the multijet background event
 1335 should contribute to the small M_T^W region. The template sample can contain also contributions from
 1336 other backgrounds (mostly coming from $W \rightarrow l\nu$). The best template selection should allow for big
 1337 data statistics and small electroweak contributions at the same time. In order to suppress the signal
 1338 additionally reversed ID or isolation criteria is applied.

1339 In electron channel, the template selection requires an electron candidate to fail medium identifi-
 1340 cation criteria, but to pass loose selection. Control distributions for a different template selection in
 1341 electron channel are shown on a Fig. 12.1. Relaxed E_T^{miss} cut allows to gain bigger template statistics.

1342 In a muon channel template selection is build by inverting isolation criteria ($P_T^{cone,20} > 0.1$). In case of
 1343 $W \rightarrow \mu\nu$ the *QCD* background template the best statistics is achieved by relaxing mass transverse
 1344 M_T^W cut (Fig. 12.2).

1345 In order to avoid double counting, electroweak processes (i.e. signal and backgrounds) are sub-
 1346 tracted from a template. The total number of events in the template can be defined as:

$$N_{template} = N_{data}^{bkg\ enriched} - \sum_j^{MC} N_{MC_j}^{bkg\ enriched}, \quad (12.1)$$

1347 where $N_{data}^{bkg\ enriched}$ and $N_{MC_j}^{bkg\ enriched}$ are numbers of the events in a background enriched sample in data
 1348 and different MC samples. The resulting template statistic is 1349 and 1509 events for $W \rightarrow e\nu$ and
 1350 $W \rightarrow \mu\nu$ respectively.

1348 12.1.2 Methodology of the template sample normalization

The normalization is found through the χ^2 fit of the template and backgrounds to the data. The
 following composite model has been used for estimation:

$$M(x) = \sum_{i=1}^{N-1} f_i F_i(x) + (1 - \sum_{i=1}^{N-1} f_i) \cdot F_{QCD}(x), \quad (12.2)$$

1349 where index i goes over the MC samples, x is a fit variable (E_T^{miss} or M_T^W), $F_i(x)$ and $F_{QCD}(x)$ are
 1350 the probability density functions of MC samples and *QCD* background template respectively. Fit
 1351 parameters f_i are the fractions of MC events within the fit region. In order to eliminate systematics,
 1352 coming from the cross-section uncertainty, the signal fractions are left as free parameters of fit and
 1353 and the background MC fractions are allowed to be varied within 5% uncertainty.

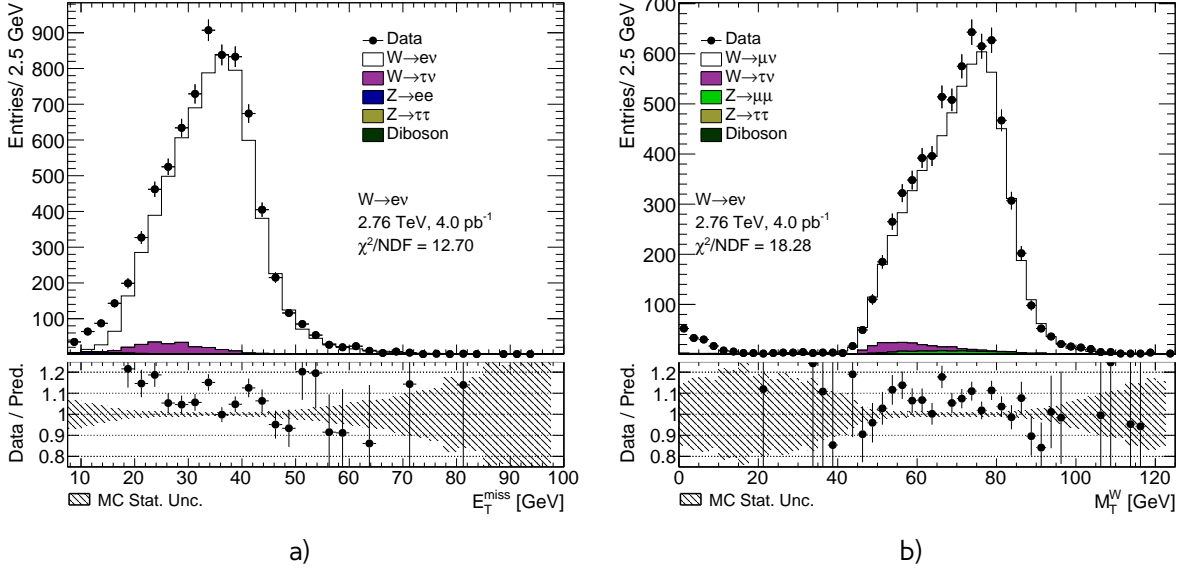


Fig. 12.3: Distributions used for multijet background estimation for a) $W \rightarrow e\nu$ b) $W \rightarrow \mu\nu$

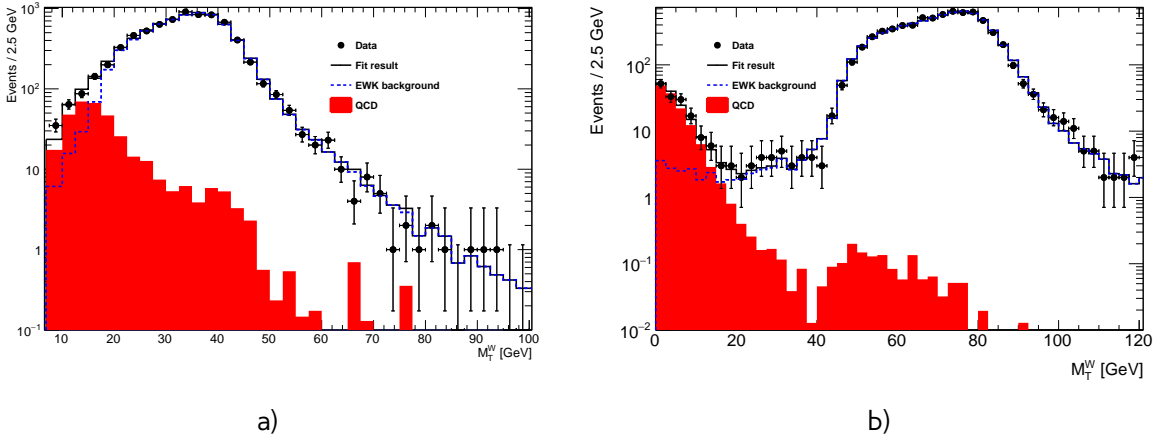


Fig. 12.4: The multijet background estimation for a) $W \rightarrow e\nu$ using reversed ID cut and released E_T^{miss} cut b) $W \rightarrow \mu\nu$ using released M_T^W cut and $bb\bar{b} + cc\bar{c}$ template

Normalisation scale of the QCD events is calculated from the obtained fit parameters as:

$$scale = \frac{(1 - \sum f_i) \cdot N_{Data}^{fit}}{N_{template}}, \quad (12.3)$$

where $\sum f_i$ is a sum of all fractions in the fit, N_{Data}^{fit} is a number of data events in a fit histogram and $N_{template}$ is a number of event in a template. The fit is performed separately for W^+ and W^- . Additionally, fit in total W channel is used as a cross-check of the fit. The results of the fitting procedure are shown on a Fig. 12.4 .

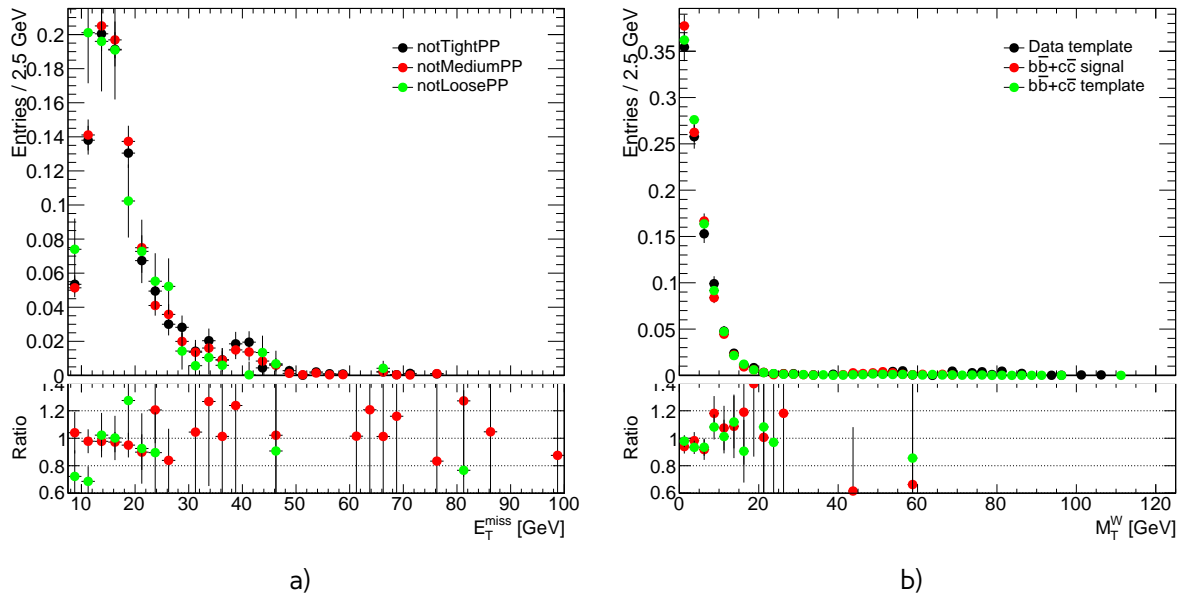


Fig. 12.5: Data and MC comparison for E_T^{miss} calculated by standard ATLAS algorithm for a) $W \rightarrow e\nu$
b) $W \rightarrow \mu\nu$ events

12.1.3 Systematic uncertainty from the multi-jet background estimation

The uncertainty of the multi-jet background estimation can be divided into 3 main components:

$$\delta_{QCD} = \sqrt{\delta_{fit\,unc}^2 + \delta_{MC}^2 + \delta_{fit\,bias}^2 + \delta_{template}^2}, \quad (12.4)$$

where $\delta_{fit\,unc}$ is the uncertainty for a scale from a χ^2 fit. The meaning of other components is explained below

The second component δ_{MC} is coming from a possible mismodelling of MC in a fitted region. It can be estimated by comparison of fit results for W , W^+ and W^- . Number of multijet background events should not depend on a charge of the analysis, so it is expected:

$$N_{QCD}^W = 0.5 \cdot N_{QCD}^{W^+} = N_{QCD}^{W^-} \quad (12.5)$$

Standard deviation of these 3 numbers is taken as systematic uncertainty. Since in $W \rightarrow \mu\nu$ channel the QCD template normalization is derived from the fit in small M_T^W region, where electroweak contributions negligible and data statistics is high, this systematic source is equal to 0.

The third component $\delta_{fit\,bias}$ is coming from an effect of an arbitrary choice of bin size. This error is estimated by repeating the fit for a different binnings. This component is assumed negligible in $W \rightarrow \mu\nu$ case.

The uncertainty $\delta_{template}$ is due to a potential bias in the template as a result of the template choice and a template statistics itself. For estimation of this uncertainty different template selections have been used. For $W \rightarrow e\nu$ channel different reversed isolation criteria have been tried (Fig. 12.5 a)). The overall discrepancies can be considered negligible. For $W \rightarrow \mu\nu$ channel template variations are estimated using fits with $b\bar{b} + c\bar{c}$ MC samples. Fig. 12.5 b) compares data template with template obtained using signal selection with released M_T^W cut and template selection. Results for a different

Table 12.2: Results of QCD background estimation for $W \rightarrow e\nu$ and corresponding error

Charge	N_{QCD}	$\delta N_{fit\,unc}$	δN_{MC}	$\delta N_{fit\,bias}$
W^+	38.3	7.0	7.0	5.0
W^-	21.5	0.7	-9.4	4.0
W	66.1	21.2	4.2	10.
Total	31.0	6.1	8.6	4.7

 Table 12.3: Results of QCD background estimation for $W \rightarrow \mu\nu$ using different templates and it's fit error

Charge	N_{QCD} data template	N_{QCD} $b\bar{b} + c\bar{c}$ template selection	N_{QCD} $b\bar{b} + c\bar{c}$ signal selection
W^+	2.48	0.73	1.34
W^-	2.48	0.73	1.35
W	4.97	1.47	2.70
Total per channel	2.48	0.73	1.35
Fit error	0.60	0.73	0.19

¹³⁷³ template fits are presented in Tab 12.3

¹³⁷⁴ Results of the QCD background uncertainty estimation for $W \rightarrow e\nu$ and $W \rightarrow \mu\nu$ are shown
¹³⁷⁵ in Tab. 12.2 and 12.3 respectively. The overall number of QCD background events is estimated as
¹³⁷⁶ 31.00 ± 13.0 for $W^+ \rightarrow e^+\nu$ and $W^- \rightarrow e^-\nu$ and 1.50 ± 0.9 for $W^+ \rightarrow \mu^+\nu$ and $W^- \rightarrow \mu^-\nu$. The
¹³⁷⁷ overall fraction of the QCD events is lower, than in 13 TeV [?], 8 TeV [?] and 7 TeV [32] data, what is
¹³⁷⁸ in agreement with expectations.

 Table 12.4: Number of observed candidate events for the $W \rightarrow l\nu$ channel, electroweak (EWK) and top, and data-driven QCD background events, and background-subtracted signal events

I	Observed candidates	Background (EWK + top)	Background (Multijet)	Background-subtracted data N_W^{sig}
W boson				
e^+	3914	108.1 ± 5.6	31.00 ± 13.0	$3774.9 \pm 62.6 \pm 5.6 \pm 13.0$
e^-	2209	74.2 ± 3.3	31.00 ± 13.0	$2103.8 \pm 47.0 \pm 3.3 \pm 13.0$
μ^+	4365	150.5 ± 6.6	1.50 ± 0.9	$4213.0 \pm 66.1 \pm 6.6 \pm 0.9$
μ^-	2460	105.6 ± 4.1	1.50 ± 0.9	$2352.9 \pm 49.6 \pm 4.1 \pm 0.9$
Z boson				
e	430	1.2 ± 0.0	-	$428.8 \pm 20.7 \pm 0.0$
μ	646	1.5 ± 0.0	-	$644.5 \pm 25.4 \pm 0.0$

1379 12.2 Background-subtracted W and Z candidate events

1380 Tables 12.4 summarize the number of background events for W and Z selections. Uncertainties on
1381 a number of EWK+top events are coming from a statistics, cross-section uncertainty (if given) and
1382 3% of luminosity determination uncertainty. For multijet background uncertainty is coming from a
1383 method and described in a subsection 12.1.3. For the background-subtracted events the statistical
1384 uncertainty is quoted first, followed by the total systematic uncertainty, derived from the EWK+top
1385 and multijet background ones, considering the sources as uncorrelated.

1386

Chapter 13

Control distributions

1388 Kinematic distributions after all cuts (Section 9) and corrections applied on MC (Section 10), are
 1389 presented in this chapter. Distributions for $W \rightarrow l\nu$ are split in charge and shown on a Figs. 13.1-
 1390 13.12. Distributions for $Z \rightarrow l^+l^-$ analysis are shown on a Fig. 13.13-13.17.

1391 These plots also showing the systematic and statistical uncertainty as a shaded band. The un-
 1392 certainties are including all sources, described in a 14, except for uncertainties coming from shape
 1393 variation due to a PDF reweighting and QCD background and luminosity. All uncorrelated uncertainty
 1394 sources are summed in quadrature. The expected background contributions are estimated using MC
 1395 simulations, apart from QCD background, which is found with a data driven method, as explained in
 1396 a previous chapter.

1397 Good overall agreement between data and MC is observed.

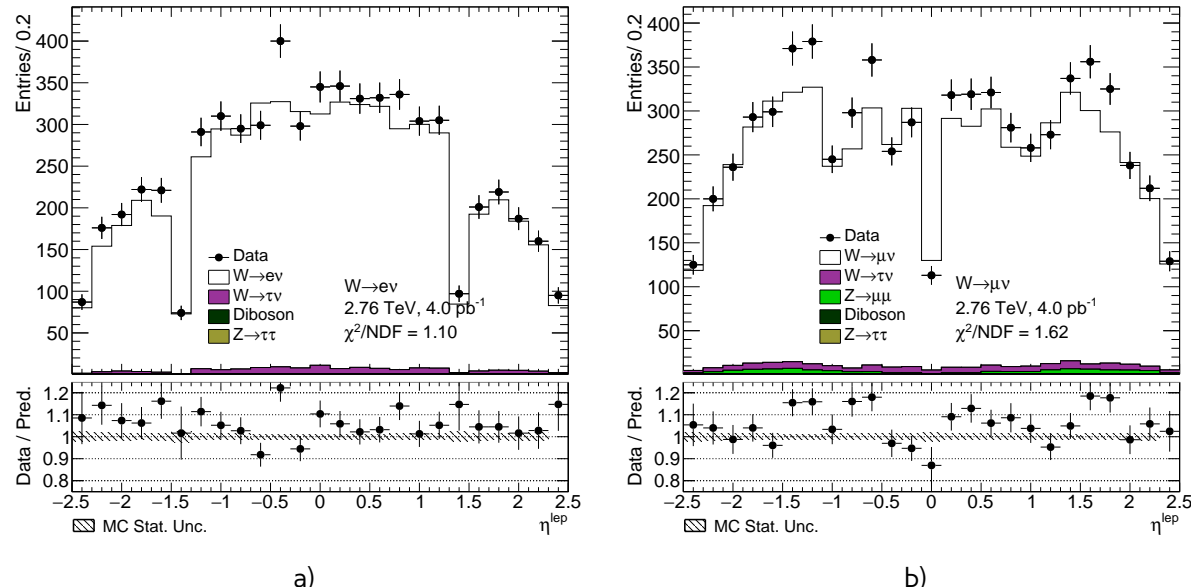


Fig. 13.1: Lepton pseudorapidity distribution from the a) $W \rightarrow ev$ selection and b) the $W \rightarrow \mu\nu$ selection.

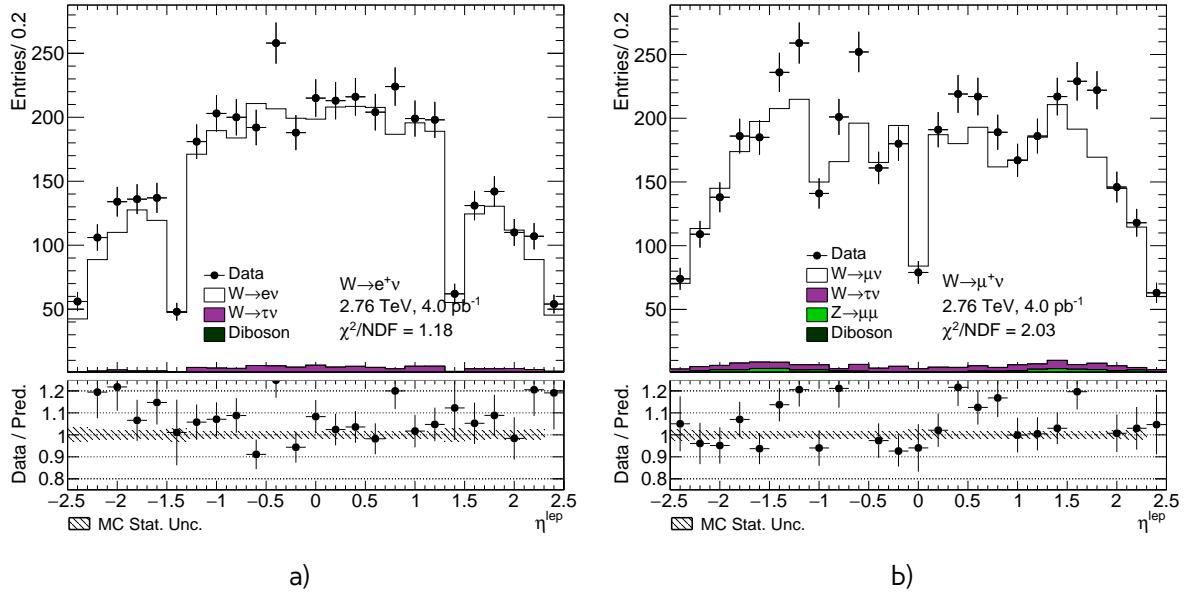


Fig. 13.2: Lepton pseudorapidity distribution from the a) $W^+ \rightarrow e^+\nu$ selection and b) the $W^+ \rightarrow \mu^+\nu$ selection.

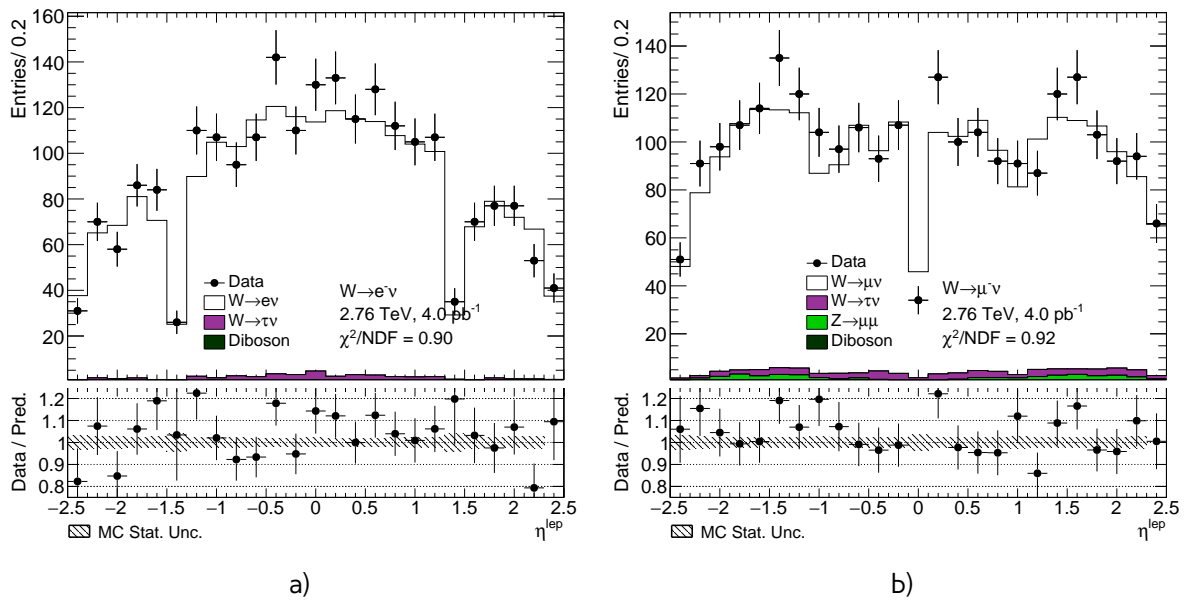


Fig. 13.3: Lepton pseudorapidity distribution from the a) $W^- \rightarrow e^-\nu$ selection and b) the $W^- \rightarrow \mu^-\nu$ selection.

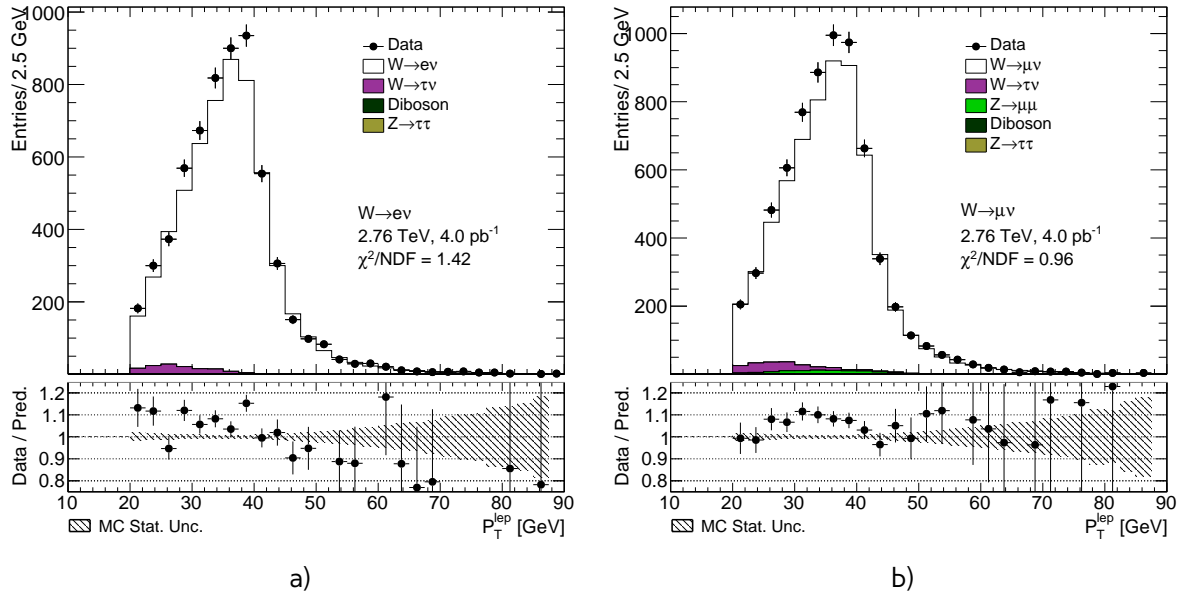


Fig. 13.4: Lepton transverse momentum distribution from the a) $W \rightarrow e\nu$ selection and b) the $W \rightarrow \mu\nu$ selection.

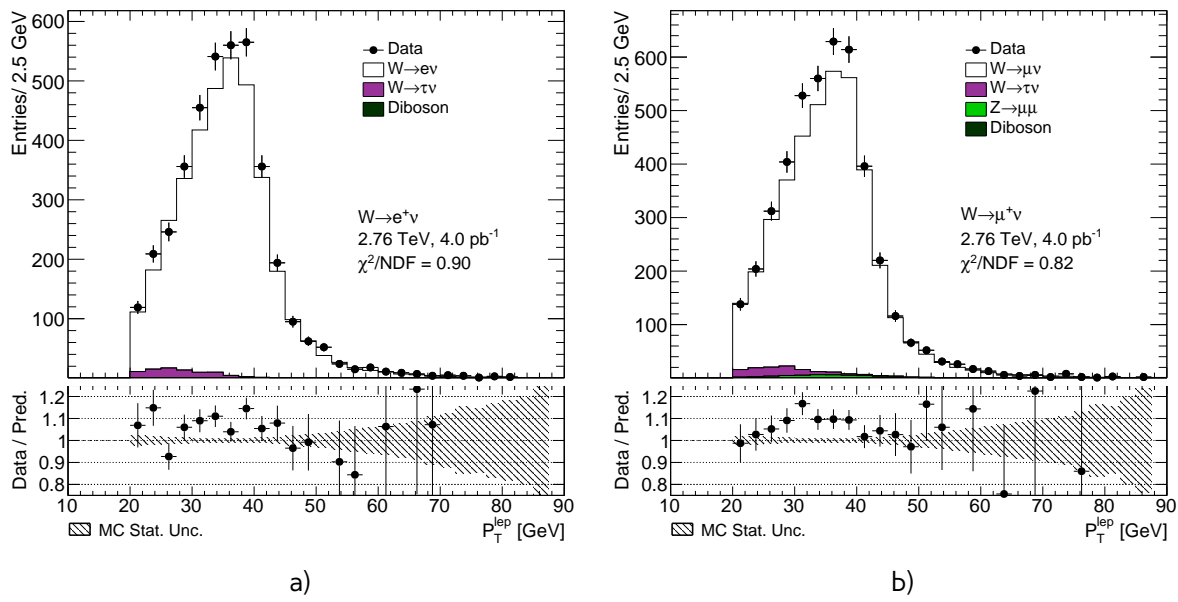


Fig. 13.5: Lepton transverse momentum distribution from the a) $W^+ \rightarrow e^+\nu$ selection and b) the $W^+ \rightarrow \mu^+\nu$ selection.

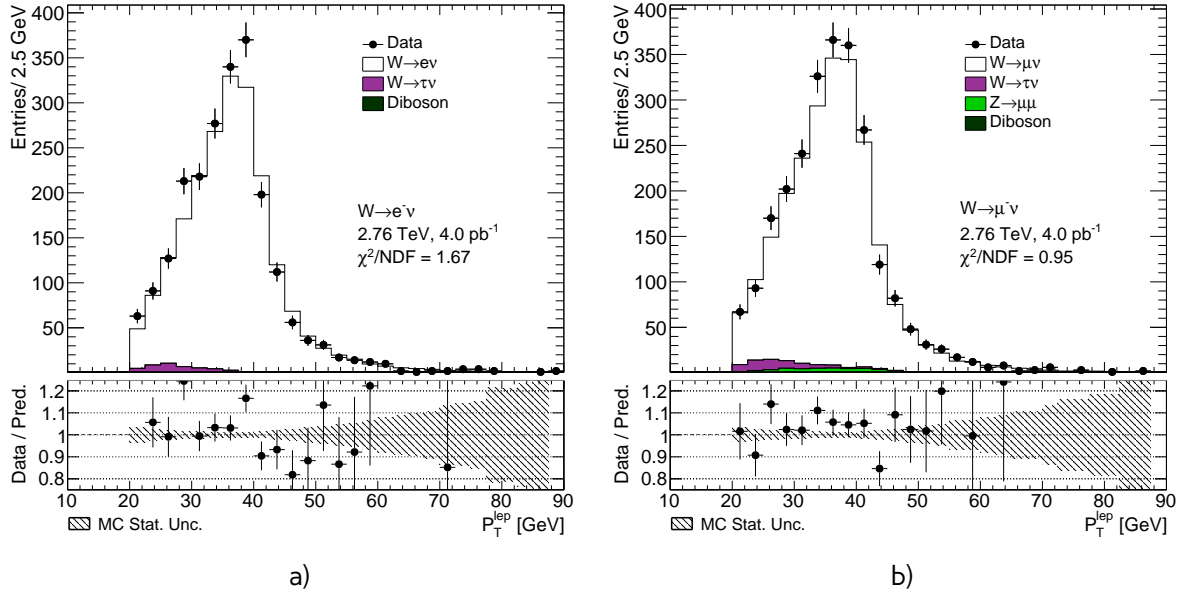


Fig. 13.6: Lepton transverse momentum distribution from the a) $W^- \rightarrow e^-\nu$ selection and b) the $W^- \rightarrow \mu^-\nu$ selection.

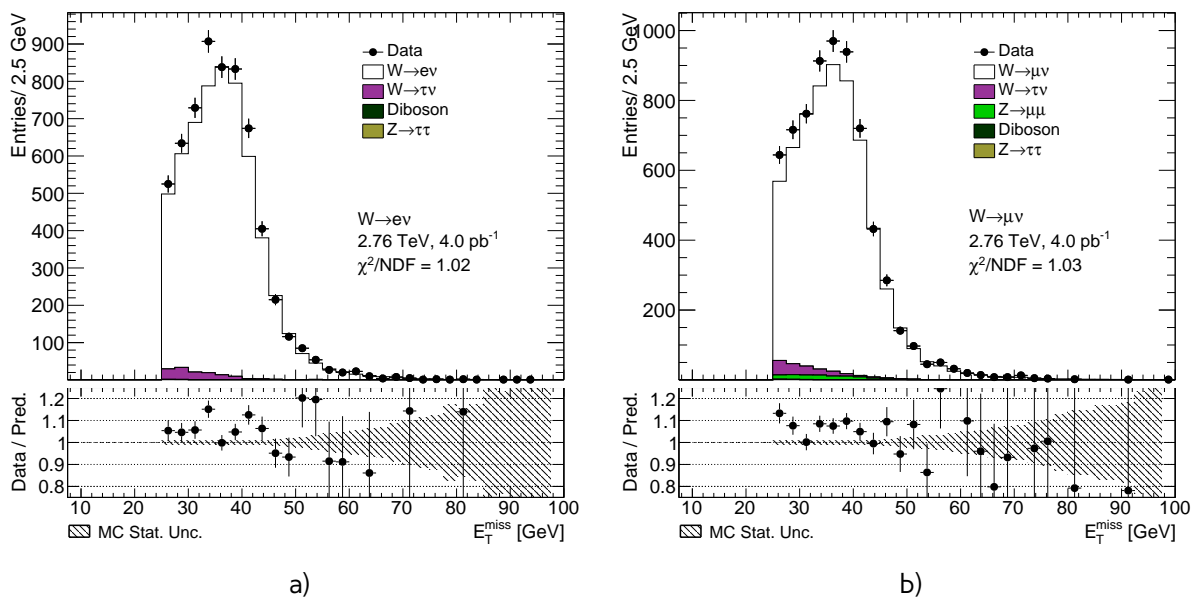


Fig. 13.7: Missing transverse energy distribution from the a) $W \rightarrow e\nu$ selection and b) the $W \rightarrow \mu\nu$ selection.

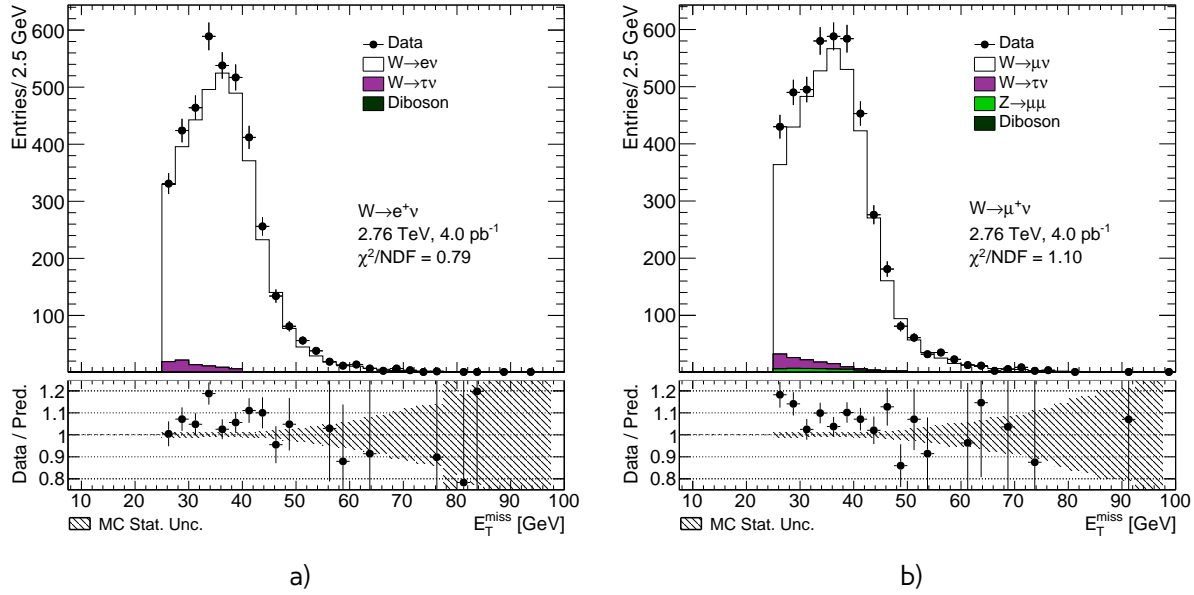


Fig. 13.8: Missing transverse energy distribution from the a) $W^+ \rightarrow e^+\nu$ selection and b) the $W^+ \rightarrow \mu^+\nu$ selection.

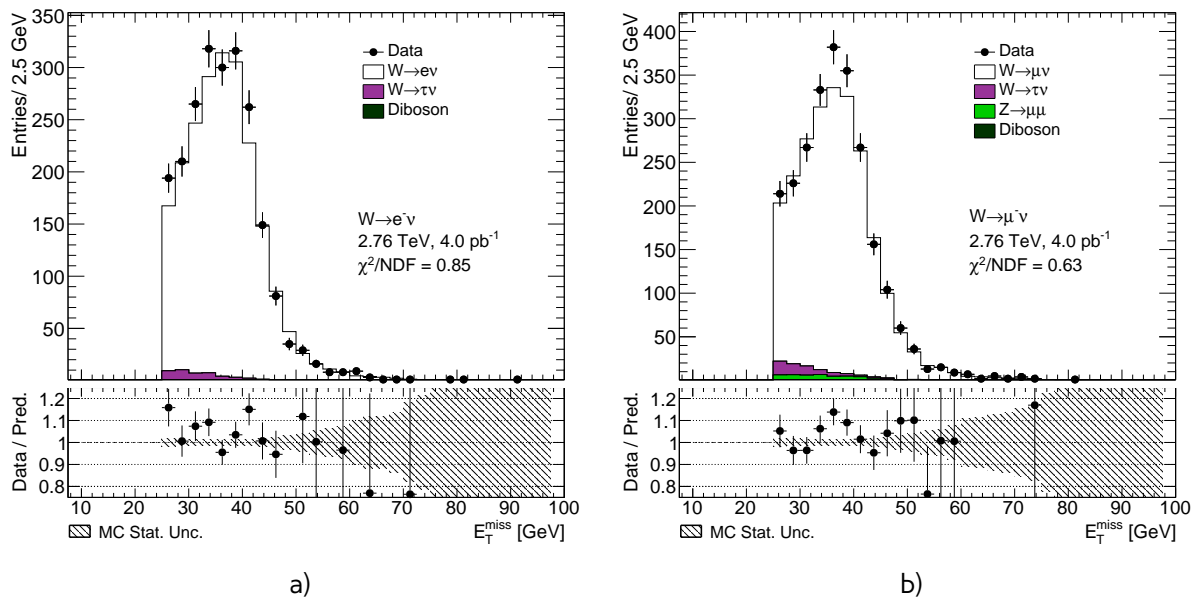


Fig. 13.9: Missing transverse energy distribution from the a) $W^- \rightarrow e^-\nu$ selection and b) the $W^- \rightarrow \mu^-\nu$ selection.

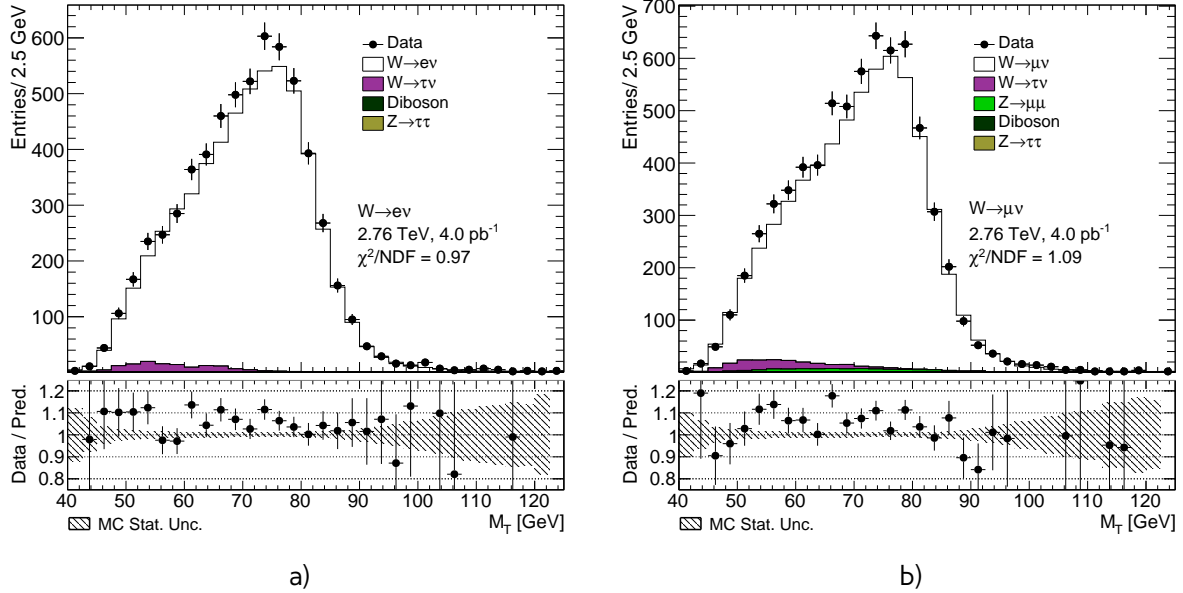


Fig. 13.10: Transverse mass distribution distribution from the a) $W \rightarrow e\nu$ selection and b) the $W \rightarrow \mu\nu$ selection.

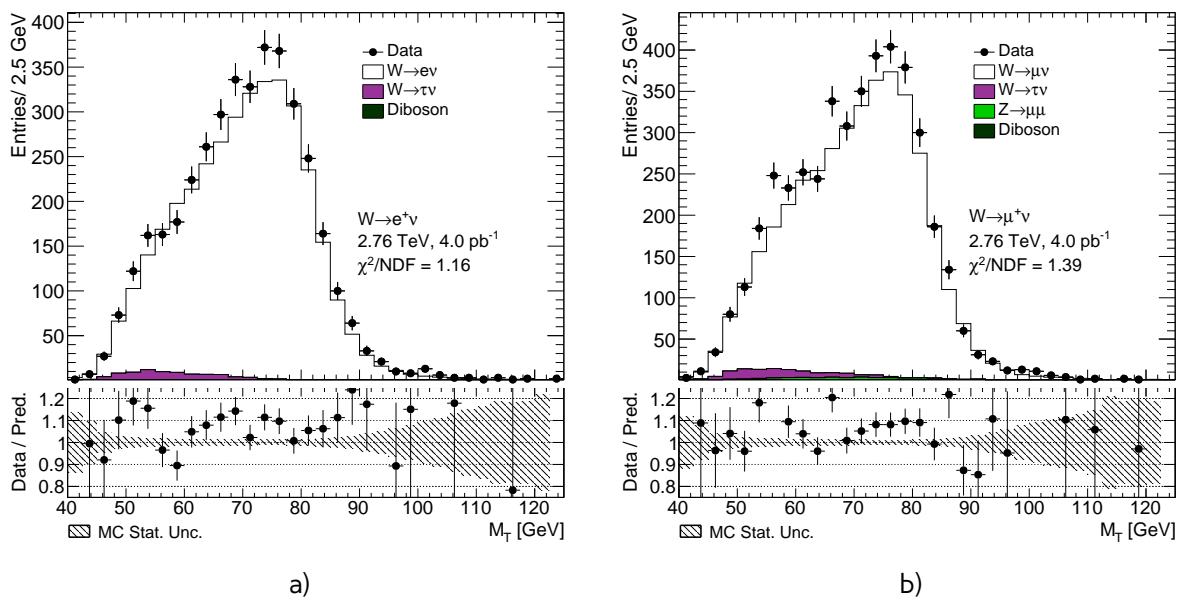


Fig. 13.11: Transverse mass distribution distribution from the a) $W^+ \rightarrow e^+\nu$ selection and b) the $W^+ \rightarrow \mu^+\nu$ selection.

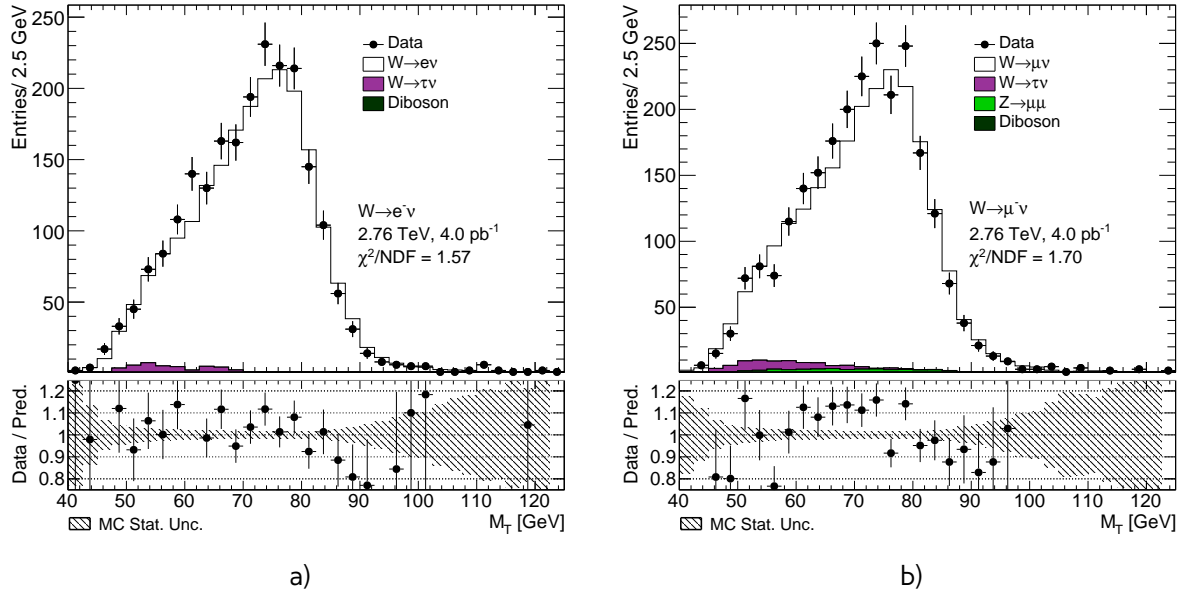


Fig. 13.12: Transverse mass distribution distribution from the a) $W^- \rightarrow e^-\nu$ selection and b) the $W^- \rightarrow \mu^-\nu$ selection.

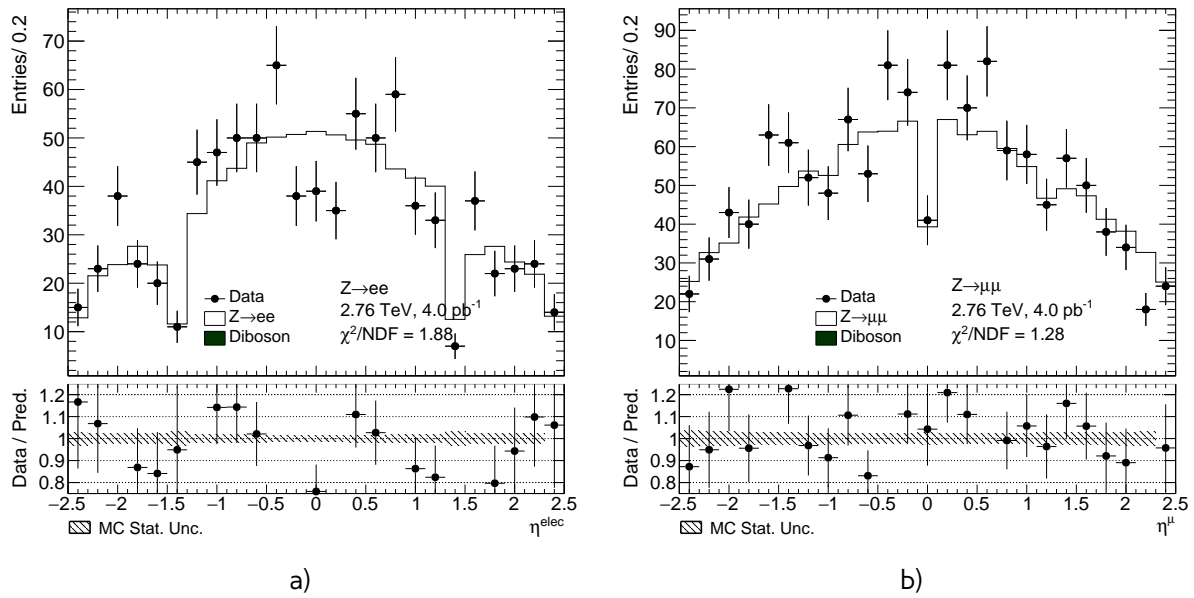


Fig. 13.13: Lepton pseudorapidity distributions from the a) $Z \rightarrow e^+e^-$ b) $Z \rightarrow \mu^+\mu^-$

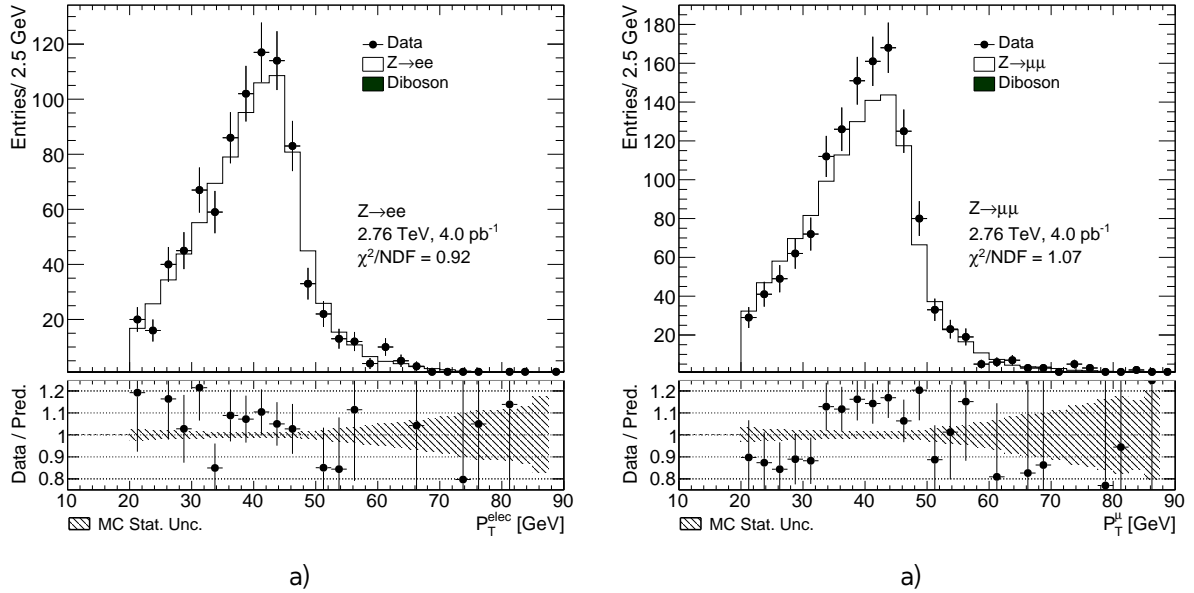


Fig. 13.14: Lepton transverse momentum distributions from the a) $Z \rightarrow e^+e^-$ b) $Z \rightarrow \mu^+\mu^-$

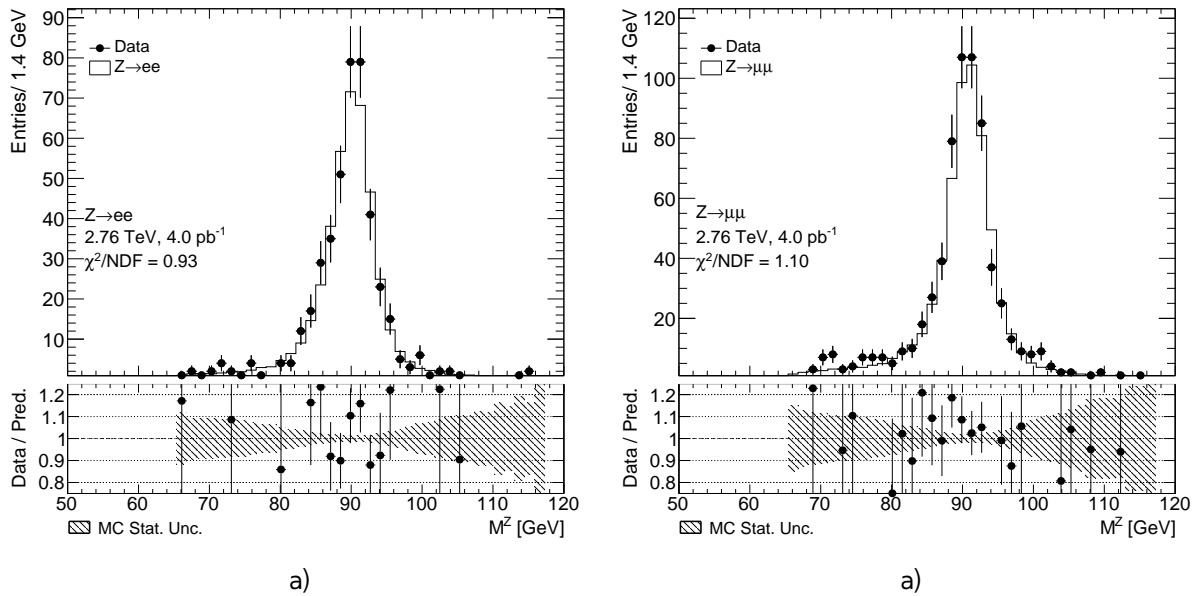


Fig. 13.15: Dilepton mass distribution distributions from the a) $Z \rightarrow e^+e^-$ b) $Z \rightarrow \mu^+\mu^-$

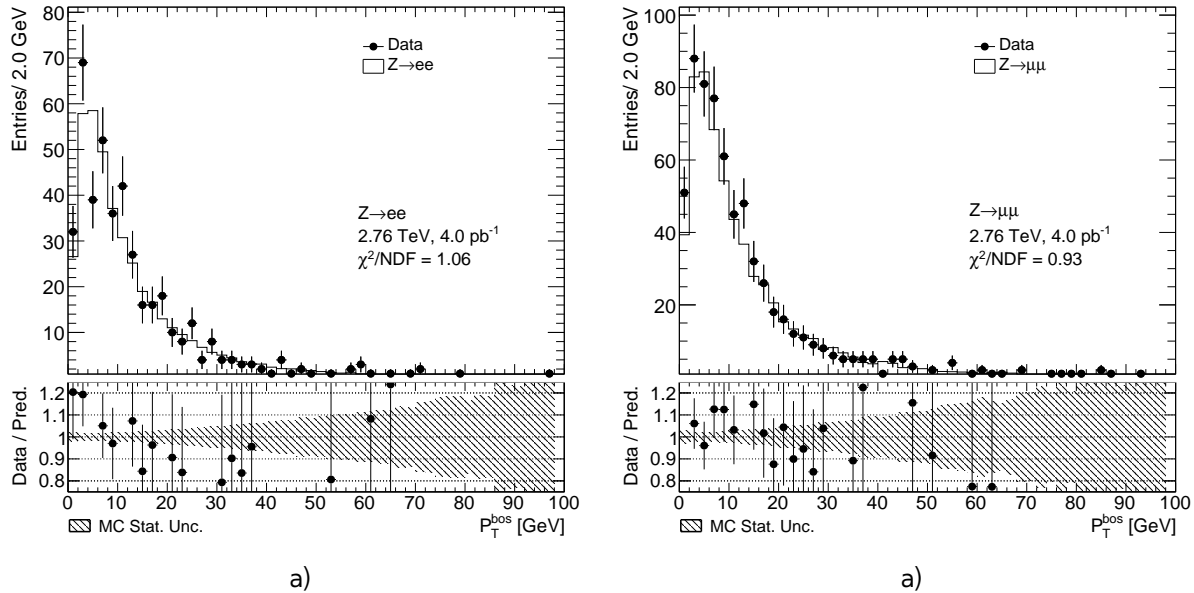


Fig. 13.16: Z boson transverse momentum distributions from the a) $Z \rightarrow e^+e^-$ b) $Z \rightarrow \mu^+\mu^-$

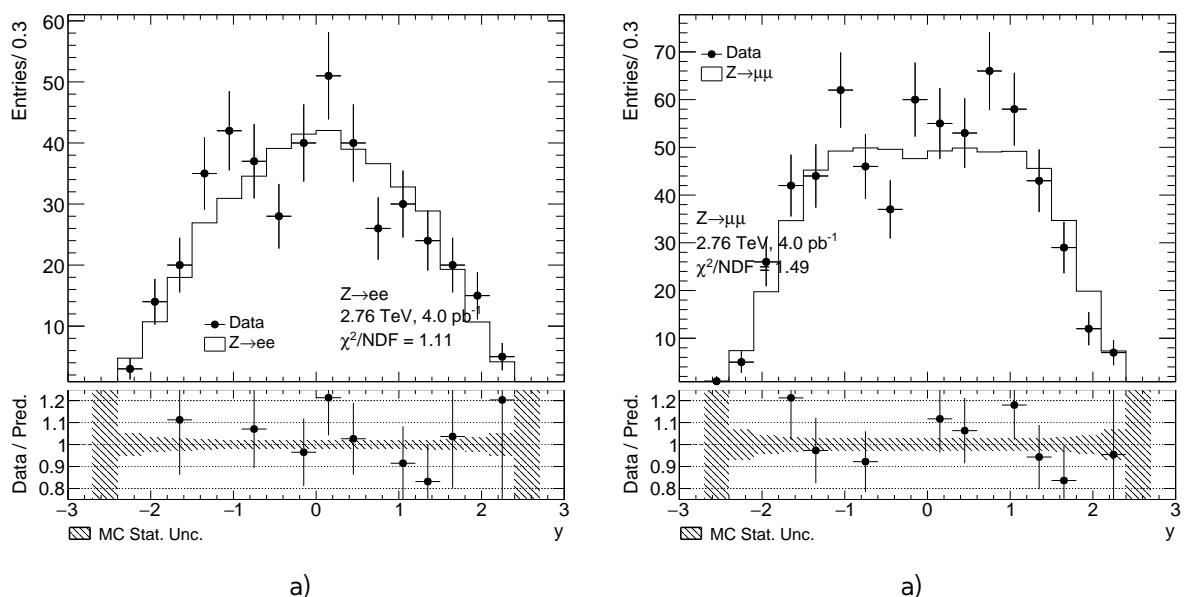


Fig. 13.17: Z boson rapidity distribution from the a) $Z \rightarrow e^+e^-$ b) $Z \rightarrow \mu^+\mu^-$

1398

Chapter 14

Uncertainties in the cross-section measurement

1400

1401	14.1 Methods of uncertainties propagation	111
1402	14.2 Experimental systematic uncertainties	112
1403	14.2.1 Electron energy scale and resolution	112
1404	14.2.2 Muon energy scale and resolution	112
1405	14.2.3 Muon and electron efficiency toy Monte-Carlo	113
1406	14.2.4 Theoretical uncertainty	113
1407	14.3 Theoretical uncertainty on $A_{W/Z}$ and $E_{W/Z}$ factors	115
1408	14.4 Correlation between uncertainties	115
1409	14.4.1 Treatment of partially correlated uncertainties	116

1410

1411

Cross-section measurement relies on theoretical models and corrections, used in Monte-Carlo. Thus, their intrinsic uncertainties should be propagated to a final result. This chapter discusses main methods of uncertainties measurements and sources on $C_{W,Z}$ and $A_{W,Z}$ correction factors.

14.1 Methods of uncertainties propagation

All sources of systematic uncertainties are propagated in these analyses using one of the main methods: Offset, On/Off or Toy Monte-Carlo. The offset method changes a correction by a $\pm 1\sigma$ of it's systematic uncertainty. The contribution of each correction's uncertainty on the observable (e.g. $C_{W,Z}$, $A_{W,Z}$ or a cross-section) is taken as a symmetric approximation:

$$U_i^{\text{offset}} = \frac{\sigma_i^{\text{up}} - \sigma_i^{\text{down}}}{2}, \quad (14.1)$$

where $\sigma_i^{\text{up(down)}}$ - the change in a observable due to the shift of the correction on σ up or down.

For On/Off method the contribution of each correction is estimated with (σ^{on}) and without(σ^{off}) correction applied. A systematic error can be estimated than as:

$$U^{\text{on/off}} = \sigma^{\text{on}} - \sigma^{\text{off}}. \quad (14.2)$$

Another one method used for a uncertainties propagation is a toy MC method, that uses a pseudo experiments with modified input corrections. For a scale factors binned p_T and η uncertainties inside each bin can be divided to a correlated and uncorrelated systematic components and statistical error.

For each pseudo-experiment, a table of new scale factors is filled, where inside each bin a scale factor is randomly varied as:

$$SF_i^{Toy_n} = SF_i + \text{Gauss}(0, \Delta SF_i^{uncorr+stat}) + \sum \Delta SF_i^{corr} \cdot \text{Gauss}(0, 1), \quad (14.3)$$

1419 where $SF_i^{Toy_n}$ is a new scale factor in i-th bin, $\Delta SF_i^{uncorr+stat}$ - is the quadratic sum of uncorrelated
1420 and statistical errors and ΔSF_i^{corr} is a correlated error.

The overall effect on a observable is calculated as a standard deviation of the values in a pseudo-experiments:

$$U_i = \sqrt{\frac{\sum_{Toy_n=1}^N \sigma_i^2}{N} - \left(\frac{\sum_{Toy_n=1}^N \sigma_i}{N} \right)^2} \quad (14.4)$$

1421 The number N of pseudo experiments should be sufficiently large to avoid possible bias in the
1422 uncertainty estimation.

14.2 Experimental systematic uncertainties

1424 Sources of experimental uncertainties, methods of estimation and their effect on a $C_{W,Z}$ are sum-
1425 marized in a Tab. 14.1. Systematical errors coming from a hadron recoil calculation are discussed in
1426 a Sec. 11.

14.2.1 Electron energy scale and resolution

1427 Electron energy scale correction, described in Sec. 10.2 has associated uncertainties coming from [33]:
1428

- 1429 • Statistical component of the scale uncertainty
- 1430 • Uncertainty from the possible bias of the calibration method
- 1431 • Scale uncertainty from the choice of generator
- 1432 • Uncertainty from the presampler energy scale
- 1433 • Imperfect knowledge of the material in front of EM calorimeter.

1434 The uncertainty contribution from each component is estimated using offset method. The total
1435 energy scale uncertainty is the quadratic sum of the components [?].

14.2.2 Muon energy scale and resolution

1437 Systematic uncertainties coming from muon momentum corrections described in Sec. 10.3 can be
1438 divided into 3 major independent categories:

- 1439 • variations of the smearing of MS track
- 1440 • variation of the smearing of ID track
- 1441 • overall scale uncertainty

1442 The uncertainty contribution from each component is estimated using offset method. The total
1443 energy scale uncertainty is the quadratic sum of the components.

1444 **14.2.3 Muon and electron efficiency toy Monte-Carlo**

1445 In case of 2.76 TeV analysis scale factor errors are considered to be enlarged for a statistical and
1446 uncorrelated components, so correlated error is assumed to be negligible. The toy MC experiments
1447 are performed for electron reconstruction, identification and trigger scale factors and muon recon-
1448 struction + identification scale factors. In the current analysis 30 pseudo-experiments are used with
1449 a combined toy MC method.

1450 **14.2.4 Theoretical uncertainty**

1451 The theoretical uncertainty considered to be coming from imperfect knowledge of parton functions
1452 and is calculated as:

- 1453 • Error coming from an arbitrary choice of PDF set is estimated by PDF reweighting [34] of
1454 original MC generated using CT10 PDF set to one of the 4 pdf sets: ATLAS-epWZ12 [35],
1455 abkm09 [36] and NNPDF23 [37]. The error is calculated as a maximum deviation between the
1456 acceptance calculated CT10 and different PDF set.
- Systematic uncertainty within one pdf set is evaluated using CT10 NLO set. This set contains
52 associated error sets, corresponding to a 90% C.L. limits along 26 eigenvectors. The resulting
52 variation are separately added in a quadrature as:

$$\delta_X = \frac{1}{2} \cdot \sqrt{\sum_{i=1}^N (X^+ - X^-)^2} \quad (14.5)$$

Table 14.1: Summary of the different terms contributing to the uncertainty on C factors for all analyses

		$W^+ \rightarrow e\nu$	$W^- \rightarrow e\nu$	$W^+ \rightarrow \mu\nu$	$W^+ \rightarrow \mu\nu$	$Z \rightarrow ee$	$Z \rightarrow \mu\mu$
Value C		0.6801	0.6799	0.7487	0.7520	0.5575	0.8020
Source of uncertainty	Method	$\delta C_W/C_W(\%)$ $W^+ \rightarrow e\nu$	$\delta C_W/C_W(\%)$ $W^- \rightarrow e\nu$	$\delta C_W/C_W(\%)$ $W^+ \rightarrow \mu\nu$	$\delta C_W/C_W(\%)$ $W^+ \rightarrow \mu\nu$	$\delta C_Z/C_Z(\%)$ $Z \rightarrow ee$	$\delta C_Z/C_Z(\%)$ $Z \rightarrow \mu\mu$
Electron reconstruction	Toy MC	0.11	0.09	-	-	0.12	-
Electron identification	Toy MC	0.32	0.30	-	-	0.54	-
Electron trigger efficiency	Toy MC	0.14	0.13	-	-	0.001	-
Muon reco+id	Toy MC	-	-	0.03	0.02	-	0.03
Electron energy scale	Offset	0.44	0.43	-	-	0.34	-
- Statistical error	Offset	0.05	0.04	-	-	0.04	-
- Bias in method	Offset	0.41	0.40	-	-	0.31	-
- Scale uncertainty	Offset	0.0	0.0	-	-	0.0	-
- Low Pt	Offset	0.0	0.0	-	-	0.003	-
- Presampler energy scale	Offset	0.04	0.03	-	-	0.04	-
- Material knowledge	Offset	0.14	0.13	-	-	0.14	-
Electron energy resolution	Offset	0.05	0.03	-	-	0.03	-
Muon energy scale	Offset	-	-	0.05	0.05	-	0.03
Muon energy resolution total	Offset	-	-	0.02	0.01	-	0.02
- Muon ID energy scale	Offset	-	-	0.02	0.01	-	0.01
- Muon MS energy scale	Offset	-	-	0.01	0.00	-	0.01
Hadron recoil scale	Offset	0.15	0.17	0.15	0.19	-	-
Hadron recoil resolution	On/Off					-	-
EWK + $t\bar{t}$ background	Offset	0.15	0.16	0.16	0.17	0.01	0.01
QCD	Offset	0.34	0.62	0.02	0.04	-	-
Theory							
Total		0.0041	0.0040	0.0013	0.0014	0.0036	0.0004
Statistics		1.60	2.13	1.51	2.02	4.82	3.93

Table 14.2: Acceptance values (A) and extrapolation values (E) and their relative uncertainties in percent for W and Z production in electron and muon channels. The various components of the uncertainties are defined in the text. The total uncertainties (δA_{tot} and δE_{tot}) are obtained as the quadratic sum of the three parts.

	A	δA_{err}^{pdf}	δA_{sets}^{pdf}	δA_{hs+ps}	δA_{tot}
W^+	0.20	0.22	0.9	0.9	0.9
W^-	0.62	0.63	0.9	0.9	0.9
Z	0.40	0.53	0.9	0.9	0.9
	E	δE_{err}^{pdf}	δE_{sets}^{pdf}	δE_{hs+ps}	δE_{tot}
W^+	0.04	0.08	0.7	0.7	0.7
W^-	0.04	0.08	1.0	1.0	1.0
Z	0.05	0.04	1.0	1.0	1.0

14.3 Theoretical uncertainty on $A_{W/Z}$ and $E_{W/Z}$ factors

The effect of theoretical uncertainties must be considered for extrapolated cross-sections, through its effect on extrapolation factors $A_{W,Z}$, $E_{W,Z}$ factors. They are estimated taking into account different independent contributions:

- Error coming from an arbitrary choice of PDF set and systematic error within one pdf set is estimated in the same way, as for C_W (see Sec. 14.2.4). These sources are considered to be independent and added in a quadrature.
- The uncertainties arising from the choice of generator and parton showering model δA_{hs+ps} are considered small. They can be calculated as a difference in the acceptances $A_{W,Z}$ for MC samples, generated using same PDF set, but different models for showering and matrix element, namely Powheg + Pythia and Sherpa. The systematic error obtained for W channels is 0.9% for A_W . It is consistent with 13 TeV and 7 TeV measurements.

Because of the lack of simulation samples for $Z \rightarrow ll$ using Sherpa generator a systematic uncertainty for Z is estimated using the fact, that for 13 TeV analysis and 8 TeV systematic errors coming from that source have been the same for A-factors in W^+ , W^- and Z.

The overall theoretical systematic uncertainty on A and E factors are summarised in Tab. 14.2 and factor.

14.4 Correlation between uncertainties

In order to calculate W/Z ratios and combine channels different channels of the analysis it is crucial to take into account correlations between different channels. In this sections the assumptions about correlations between channels will be discussed.

The theoretical uncertainties on A and C factors, except for the uncertainty within 1 pdf set are considered to be fully correlated between all analysis. The uncertainties within 1 pdf set are considered to be partially correlated (see Sec. 14.4.1). The systematic uncertainties from electroweak

1481 background sources are treated as uncorrelated between W and Z channels and 100% correlated for
1482 different W and Z channels.

1483 In addition to electroweak background uncertainty the following systematic sources are considered
1484 to be fully correlated between $W^+ \rightarrow e\nu$, $W^- \rightarrow e\nu$, $W^+ \rightarrow \mu\nu$ and $W^- \rightarrow \mu\nu$:

- 1485 • QCD background
- 1486 • Hadronic recoil scale
- 1487 • Hadronic recoil resolution

1488 In addition to the mentioned systematics, the following uncertainties are considered 100% corre-
1489 lated in electron analyses:

- 1490 • Electron energy scale
- 1491 • Electron resolution

1492 and in muon analyses:

- 1493 • Muon energy scale
- 1494 • Muon resolution
- 1495 • Muon trigger efficiency

1496 The uncertainties, estimated using toy MC method are considered partially correlated and a co-
1497 variances between the analyses are estimated in the following section.

1498 14.4.1 Treatment of partially correlated uncertainties

1499 The following uncertainties are considered to be partially correlated between Z, W^+ and W^- analyses
1500 for an observables o_X and o_Y :

- 1501 • Electron trigger efficiency
- 1502 • Electron resolution efficiency
- 1503 • Electron identification efficiency
- 1504 • Muon reconstruction + identification efficiency
- 1505 • Uncertainties within 1 pdf set

For each source of uncertainty a correlation coefficients between analysis X and Y can be estimated
as:

$$\rho_{XY} = \frac{1}{\sigma(o_X)\sigma(o_Y)} \cdot \frac{1}{N} \sum_{i=1}^N (o_X^i - \bar{o}_X)(o_Y^i - \bar{o}_Y) = \frac{C_{XY}}{\sigma(o_X)\sigma(o_Y)}, \quad (14.6)$$

1506 where \bar{o}_X and \bar{o}_Y are the mean values of o_X and o_Y respectively, $\sigma(o_X)$ and $\sigma(o_Y)$ are the uncer-
1507 tainties and i is the number of experiment. The C_{XY} denotes elements of the covariance matrix.
1508 Resulting correlation matrices for each toy MC systematic source are shown in Fig. 14.1.

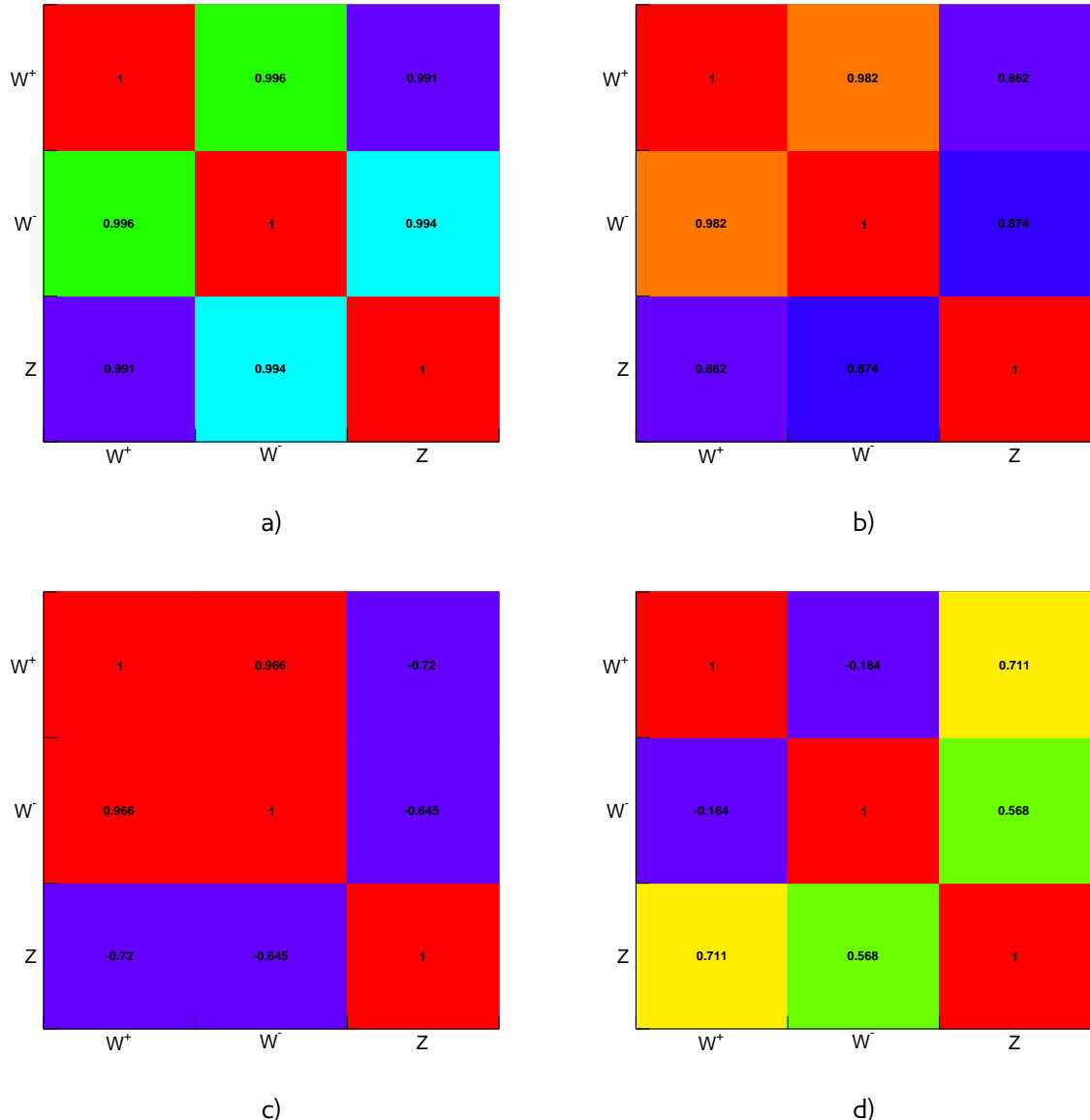


Fig. 14.1: Correlation coefficients among C_Z , C_{W^+} and C_{W^-} for a) electron reconstruction, b) electron identification, c) electron trigger and d) muon trigger scale factor uncertainties.

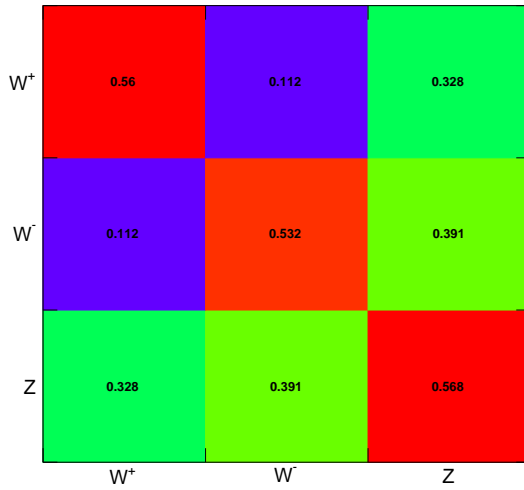


Fig. 14.2: Covariance coefficients among A_Z , A_{W^+} and A_{W^-} for the PDF uncertainty within 1 pdf set

Correlation coefficients for a systematic error within 1 pdf set are considered independent for each eigenvectors. Using the Eq. 14.6 and 14.5 the total correlation matrix C_{XY}^{PDF} can be calculated as:

$$C_{XY}^{PDF} = \frac{1}{4} \sum (X^+ - X^-) \cdot (Y^+ - Y^-). \quad (14.7)$$

1509 The resulting covariance matrix for an A factor is shown in Fig. 14.2.

The covarinace matrix C, using Cholesky decomposition [38] can be re-written as:

$$C = L \cdot L^T, \quad (14.8)$$

1510 where L is a lower triangular matrix, and L^T is a transpose of L. Because the covariance matrix
 1511 has a positive definitive this matrix is always unique. Rows of the matrix L are corresponding to an
 1512 systematic error vectors, that are fully correlated between W^+ , W^- and Z analyses. This allows the
 1513 coherent treatment of the correlated uncertainties.

1514

Chapter 15

Results of the cross-section measurement

1516

1517	15.1 Cross-sections results	119
1518	15.1.1 Lepton universality test	120
1519	15.2 Combined results	121
1520	15.2.1 Cross-sections ratios	121
1521	15.3 Comparation with theoretical predictions	122
1522	15.4 Effect on PDF distributions	122

1527 In this chapter results of the W/Z cross-section measurements will be discussed. In Sec. 15.1 the
 1528 cross-sections measured in each lepton flavors are presented. These results are used to test lepton
 1529 universality in 2.76 TeV data.

1530 Section 15.2 describes a results obtained for combined W and Z cross-sections. Additionally, the
 1531 cross-section ratios are presented. In Sec. 15.3 the combined cross-sections are compared to the
 1532 theoretical NLO predictions for different PDF sets. Finally, the results of cross-section measurement
 1533 are interpreted using PDF profiling.

1534 15.1 Cross-sections results

1535 The cross-sections are calculated as described in Chap. 3. Table ?? reports the number of candidates,
 1536 the estimated background events and $C_{W/Z}$, $A_{W/Z}$ and $E_{W/Z}$ used in a different measurements are
 1537 presented.

1538 The total uncertainty of the measurements in the fiducial region consists of the statistical, sys-
 1539 tematical and luminosity errors. The methods of these uncertainties determination are described in
 1540 Chap. 14. Uncertainty coming from luminosity measurments is labeled lumi. and is considered to be
 1541 correlated for each channel. The statistical uncertainty is labeled stat. and is a dominant one for Z
 1542 measurements and W boson measurements in electron channel. For W boson in electron channel
 1543 the systematic uncertainty is around 1%, that makes it significantly lower, than a statistical uncer-
 1544 tainty. For W boson in a muon channel cross-sections the overall systematical uncertainty is higher
 1545 because of the trigger scale factors, and is around 1.2%, that makes it comparable with the statistical
 1546 uncertainty.

Table 15.1: Results on a fiducial σ^{fid} and total cross-section measurement for W^+ , W^- and Z bosons in electron and muon channels. The cross-sections are shown with their statistical, systematical and luminosity uncertainties (and extrapolation error for total cross-section) quoted in that order

	value \pm stat \pm syst \pm lumi (\pm ext)	value \pm stat \pm syst \pm lumi (\pm ext)
W in electron channel		
	$W^+ \rightarrow e\nu$	$W^- \rightarrow e\nu$
σ_W^{fid} [pb]	$1406.0 \pm 23.3 \pm 8.4 \pm 42.2$	$783.8 \pm 17.5 \pm 4.5 \pm 23.5$
σ_W^{tot} [pb]	$2253.6 \pm 37.3 \pm 13.4 \pm 67.6 \pm 1.0$	$1373.0 \pm 30.7 \pm 7.9 \pm 41.2 \pm 5.9$
σ_W^{13} [pb]	$1293.9 \pm 21.4 \pm 7.7 \pm 38.8 \pm 0.0$	$733.8 \pm 16.4 \pm 4.2 \pm 22.0 \pm 0.0$
W in muon channel		
	$W^+ \rightarrow \mu\nu$	$W^- \rightarrow \mu\nu$
σ_W^{fid} [pb]	$1425.3 \pm 22.4 \pm 2.3 \pm 42.8$	$792.5 \pm 16.7 \pm 1.6 \pm 23.8$
σ_W^{tot} [pb]	$2284.7 \pm 35.8 \pm 3.7 \pm 68.5 \pm 1.0$	$1389.6 \pm 29.3 \pm 2.9 \pm 41.7 \pm 6.2$
σ_W^{13} [pb]	$1312.2 \pm 20.6 \pm 2.1 \pm 39.4 \pm 0.0$	$741.4 \pm 15.6 \pm 1.5 \pm 22.2 \pm 0.0$
Z		
	$Z \rightarrow ee$	$Z \rightarrow \mu\mu$
σ_Z^{fid} [pb]	$194.8 \pm 9.4 \pm 1.3 \pm 5.8$	$203.5 \pm 8.0 \pm 0.1 \pm 6.1$
σ_Z^{tot} [pb]	$310.4 \pm 15.0 \pm 2.0 \pm 9.3 \pm 1.1$	$322.9 \pm 12.7 \pm 0.1 \pm 9.7 \pm 1.0$
σ_Z^{13} [pb]	$176.1 \pm 8.5 \pm 1.1 \pm 5.3 \pm 0.0$	$183.2 \pm 7.2 \pm 0.1 \pm 5.5 \pm 0.0$

15.1.1 Lepton universality test

Because of the lepton universality of the Standard Model, the results, obtained in electron and muon channel are expected to agree with each other. The 2.76 TeV data could be used to test it via fiducial cross-section ratios of e and μ branching fractions:

$$R_W = \frac{\sigma_W^\mu}{\sigma_W^e} = \frac{BR(W \rightarrow \mu\nu)}{BR(W \rightarrow e\nu)} = 1.012 \pm 0.026(\text{sys.}) \pm 0.019(\text{stat.}),$$

where the W cross-sections are calculated in fiducial region following the prescription from Sec. 3.1.3:

$$\sigma_W^{fid}(W \rightarrow e\nu) = 2190.0 \pm 29.1(\text{stat.}) \pm 7.8(\text{sys.}) \pm 65.7(\text{lumi.}) [\text{pb}]$$

$$\sigma_W^{fid}(W \rightarrow \mu\nu) = 2217.0 \pm 27.9(\text{stat.}) \pm 50.6(\text{sys.}) \pm 66.5(\text{lumi.}) [\text{pb}]$$

This result agrees within the uncertainty with the world average of 0.991 ± 0.018 [39].

Similarly, this ratio can be measured in a Z boson decays as:

$$R_Z = \frac{\sigma_Z^\mu}{\sigma_Z^e} = \frac{BR(Z \rightarrow \mu\mu)}{BR(Z \rightarrow ee)} = 1.046 \pm 0.004(\text{sys.}) \pm 0.065(\text{stat.})$$

This ratio value is statistics dominated. The world average for a corresponding value is 1.0009 ± 0.0028 [39]. Comparison of the R_W and R_Z with the respect of the correlated systematic uncertainties with the world average is shown in Fig. 15.1. The obtained values are agreeing withing the systematic uncertainty with the standard model expectations.

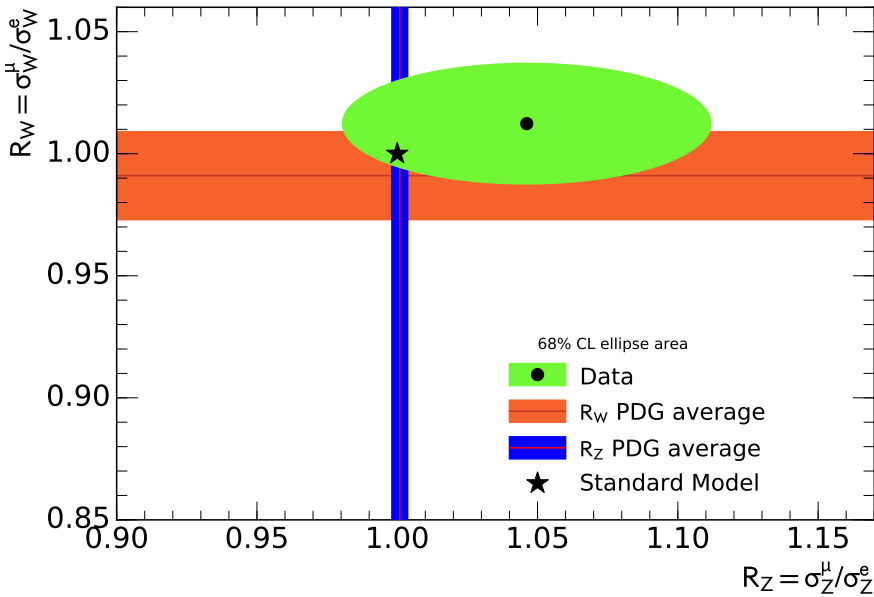


Fig. 15.1: The correlated measurement of the electron-to-muon fiducial cross-section ratios in the W and the Z channels. The vertical (horizontal) band represents the uncertainty of the corresponding Z (W) branching fractions based on the current world average data. The green ellipse illustrates the 68% CL for the correlated measurement of R_W and R_Z .

15.2 Combined results

Since the results between channels are agreeing well, it is possible to perform averaging as described in Sec. 3.3. The combination is done separately for fiducial, full and new 13 TeV cross-sections. Systematic uncertainties for the averaging are taken from Tab. 14.1. The systematic uncertainties calculated using Toy MC are included in the averaging following the prescription from Sec. 14.4. The common luminosity uncertainty is excluded from the combination process. The systematic uncertainties from electroweak background sources are considered uncorrelated between W and Z bosons and 100% correlated for different W and Z channels.

The resulting cross-sections are summarized in Tab. 15.2. The total systematic uncertainty for W cross-sections is below 2%, what is smaller, than a statistical one, while the Z boson cross-sections uncertainties are fully dominated by the statistics. The uncertainties due to the extrapolation to the new 13 TeV common phase-space are also negligible. The luminosity uncertainty 3% is fully correlated between the measurements.

The combination yields a good $\chi^2/NDF=1.0/3$ indicating good agreement between measurements. The combined cross-section is extrapolated to the full fiducial phase-space using $A_{W/Z}$ factors.

15.2.1 Cross-sections ratios

Measurement of the ratios is a powerful tool to test PDF predictions, since it allows to cancell the biggest uncertainty coming from luminosity. The ratios for W/Z cross section have been calculated

Table 15.2: Results on a fiducial σ^{fid} and total cross-section measurement for W^+ , W^- and Z bosons in electron and muon channels. The cross-sections are shown with their statistical, systematical and luminosity uncertainties (and extrapolation error for total cross-section) quoted in that order

	value \pm stat \pm syst \pm lumi (\pm ext)	value \pm stat \pm syst \pm lumi (\pm ext)
$W^{+/-}$		
	$W^+ \rightarrow l\nu$	$W^- \rightarrow l\nu$
σ_W^{fid} [pb]	$1413.3 \pm 16.1 \pm 6.9 \pm 42.4$	$786.7 \pm 12.1 \pm 3.8 \pm 23.6$
σ_W^{tot} [pb]	$2264.8 \pm 25.8 \pm 10.9 \pm 67.9 \pm 6.4$	$1380.1 \pm 21.2 \pm 14.8 \pm 41.4 \pm 3.6$
σ_W^{13} [pb]	$1300.4 \pm 14.8 \pm 6.3 \pm 39.0$	$736.2 \pm 11.3 \pm 3.6 \pm 22.1$
$W \rightarrow l\nu$		
σ_W^{fid} [pb]	$2200.0 \pm 20.1 \pm 10.7 \pm 66.0$	
σ_W^{tot} [pb]	$3644.9 \pm 33.4 \pm 21.1 \pm 109.3 \pm 6.7$	
σ_W^{13} [pb]	$2036.6 \pm 18.6 \pm 9.9 \pm 61.1$	
$Z \rightarrow ll$		
σ_Z^{fid} [pb]	$200.4 \pm 6.1 \pm 0.1 \pm 6.0$	
σ_Z^{tot} [pb]	$319.2 \pm 9.8 \pm 1.7 \pm 9.6 \pm 0.3$	
σ_Z^{13} [pb]	$180.2 \pm 5.5 \pm 0.1 \pm 5.4$	

1581 in a fiducial region following the prescription from Sec. 3.2. The obtained results are:

$$\begin{aligned} 1582 \quad R_{W/Z} &= 10.978 \pm 0.350 \text{ (stat.)} \pm 0.048 \text{ (sys.)} \\ 1583 \quad R_{W^+/Z} &= 7.052 \pm 0.230 \text{ (stat.)} \pm 0.031 \text{ (sys.)} \\ 1584 \quad R_{W^-/Z} &= 3.926 \pm 0.134 \text{ (stat.)} \pm 0.017 \text{ (sys.)} \\ 1585 \quad R_{W^+/W^-} &= 1.796 \pm 0.034 \text{ (stat.)} \pm 0.000 \text{ (sys.)} \end{aligned}$$

1586 15.3 Comparation with theoretical predictions

1587 The theoretical predictions are calculated at NLO using MCFM [40] for a different PDF sets: ABM12nlo
 1588 [42], CT14nlo [43], MMHTnlo [44], ATLAS-epWZnlo, HERAPDF2.0nlo in fiducial region. The MCFM is
 1589 a parton-level Monte-Carlo generator, that gives a predictions at LO and NLO level. It is interfaces
 1590 with APPLGRID [41], that provides a x vs Q^2 grid for MCFM. The comparison of cross-sections for
 1591 a combined channes is shown in Fig. ???. The theoretical predictions are agreeing with experimental
 1592 results within 2σ , however, the difference for the ratios (Fig.???) is higher.

1593 15.4 Effect on PDF distributions

1594 The effect of these cross-sections measurements estimated using PDF profiling method on CT10
 1595 nlo set with uncertainties estimated following prescription in Sec. 3.4. The fit gives $\chi^2/\text{NDF} =$, that
 1596 shows a good agreement with data. The impact is shown in Fig. ??, where results, obtained using
 1597 CT10 PDF set are compared to the profiled results with this measurement included. The impact of

1598 data on experimental uncertainties is not visible for most of the distributions, however it slightly
1599 improves knowledge of valence quarks densities.

1600

Chapter 16

1601

Summary

1602 This thesis presented the measurement of $W \rightarrow l\nu$ and $Z \rightarrow ll$ cross-sections at 2.76 TeV data.
1603 The cross-section have been measured separately in electron and muon channels and results are
1604 in a good agreement between each other. The studies of calibration of hadronic recoil at 2.76 TeV
1605 data have been performed. The background contribution have been estimated using both simulation
1606 and data-driven techniques. Experimental and theoretical uncertainties have been considered in a
1607 final cross-section. Obtained results have been used to test lepton universality and are in a good
1608 agreement with standard model predictions. Cross-section ratios have been estimated. All of the
1609 presented results are in a good agreement with theoretical predictions for different PDF sets.

1610 Bibliography

- 1611 [1] J.J. Goodson. *Search for Supersymmetry in States with Large Missing Transverse Momentum and Three Leptons*
1612 *including a Z-Boson*. PhD thesis, Stony Brook University, May 2012. Presented 17 Apr 2012.
- 1613 [2] James T. Shank. The ATLAS Detector: Status and Results from Cosmic Rays. In *Particles and fields.*
1614 *Proceedings, Meeting of the Division of the American Physical Society, DPF 2009, Detroit, USA, July 26-31,*
1615 *2009*, 2009.
- 1616 [3] ATLAS collaboration. The ATLAS experiment at the CERN Large Hadron Collider. *JINST*, 3, 2008.
- 1617 [4] W Lampl, S Laplace, D Lelas, P Loch, H Ma, S Menke, S Rajagopalan, D Rousseau, S Snyder, and G Unal.
1618 Calorimeter Clustering Algorithms: Description and Performance. Technical Report ATL-LARG-PUB-2008-
1619 002. ATL-COM-LARG-2008-003, CERN, Geneva, Apr 2008.
- 1620 [5] G. Aad et al. Expected Performance of the ATLAS Experiment - Detector, Trigger and Physics. 2009.
- 1621 [6] Th Lagouri et al. A Muon Identification and Combined Reconstruction Procedure for the ATLAS Detector
1622 at the LHC at CERN. *IEEE Trans. Nucl. Sci.*, 51:3030–3033, 2004.
- 1623 [7] S. Hassani, L. Chevalier, E. Lancon, J. F. Laporte, R. Nicolaïdou, and A. Ouraou. A muon identification and
1624 combined reconstruction procedure for the ATLAS detector at the LHC using the (MUONBOY, STACO,
1625 MuTag) reconstruction packages. *Nucl. Instrum. Meth.*, A572:77–79, 2007.
- 1626 [8] ATLAS collaboration. Performance of missing transverse momentum reconstruction in proton-proton
1627 collisions at $\sqrt{s}=7$ tev with ATLAS. *The European Physical Journal C*, 72(1), jan 2012.
- 1628 [9] ATLAS collaboration. Pile-up Suppression in Missing Transverse Momentum Reconstruction in the ATLAS
1629 Experiment in Proton-Proton Collisions at $\sqrt{s} = 8$ TeV. Technical Report ATLAS-CONF-2014-019, CERN,
1630 Geneva, May 2014.
- 1631 [10] Matthias Schott, Giovanni Siragusa, Jakub Cuth, and Tai-hua Lin. Measurement of m_W at 7 TeV: Recon-
1632 struction of the hadronic recoil. Technical Report ATL-COM-PHYS-2014-1435, CERN, Geneva, Nov 2014.
- 1633 [11] T H V Nguyen, N Besson, and M Boonekamp. ETmiss from the reconstruction and calibration of the
1634 hadronic recoil. Technical Report ATL-PHYS-INT-2010-039, CERN, Geneva, Apr 2010.
- 1635 [12] Montecarlogenerators – sherpa – hepforge. [https://sherpa.hepforge.org/trac/wiki/
1636 MonteCarloGenerators](https://sherpa.hepforge.org/trac/wiki/MonteCarloGenerators).
- 1637 [13] S.D. Drell and Tung-Mow Yan. Massive Lepton Pair Production in Hadron-Hadron Collisions at High-
1638 Energies. *Phys.Rev.Lett.*, 25:316–320, 1970.
- 1639 [14] Paolo Nason. A New method for combining NLO QCD with shower Monte Carlo algorithms. *JHEP*, 0411:040,
1640 2004.
- 1641 [15] Simone Alioli, Paolo Nason, Carlo Oleari, and Emanuele Re. NLO vector-boson production matched with
1642 shower in POWHEG. *JHEP*, 0807:060, 2008.
- 1643 [16] Torbjorn Sjostrand, Stephen Mrenna, and Peter Z. Skands. PYTHIA 6.4 Physics and Manual. *JHEP*, 0605:026,
1644 2006.
- 1645 [17] Bo Andersson, G. Gustafson, G. Ingelman, and T. Sjostrand. Parton Fragmentation and String Dynamics.
1646 *Phys.Rept.*, 97:31–145, 1983.
- 1647 [18] G. Corcella, I.G. Knowles, G. Marchesini, S. Moretti, K. Odagiri, P. Richardson, M.H. Seymour, and B.R.
1648 Webber. HERWIG 6.5: an event generator for Hadron Emission Reactions With Interfering Gluons (including
1649 supersymmetric processes). *JHEP*, 01:010, 2001.

Bibliography

- 1650 [19] T. Gleisberg, S. Hoeche, F. Krauss, M. Schoenherr, S. Schumann, F. Siegert, and J. Winter. Event generation
1651 with sherpa 1.1. *JHEP* 0902:007,2009, 2008.
- 1652 [20] Elisabetta Barberio and Zbigniew Was. Photos - a universal monte carlo for qed radiative corrections:
1653 version 2.0. *Computer Physics Communications*, 79(2):291 – 308, 1994.
- 1654 [21] Zbigniew Was. TAUOLA for simulation of tau decay and production: perspectives for precision low energy
1655 and LHC applications. *Nucl.Phys.Proc.Suppl.*, 218:249–255, 2011.
- 1656 [22] S. Agostinelli et al. GEANT4: A Simulation toolkit. *Nucl.Instrum.Meth.*, A506:250–303, 2003.
- 1657 [23] Validation of the frozen showers libraries on forward electrons results. http://atlas-computing.web.cern.ch/atlas-computing/links/PhysValDir/Egamma/electrons/10_02_2017/task1/.
- 1659 [24] Validation of the frozen showers libraries on zee sample with 1 electron in a forward
1660 region. http://atlas-computing.web.cern.ch/atlas-computing/links/PhysValDir/SMZee/01-12-2016/task1_norm/Zee/FWDZee/index.html.
- 1662 [25] Validation of the frozen showers libraries on jets sample. https://atlas-computing.web.cern.ch/atlas-computing/links/PhysValDir/JetEtMiss/jet_17-02-10_task1/JetsETmiss/Jets/AntiKt10LCTopoJets/index.html.
- 1665 [26] Hung-Liang Lai, Marco Guzzi, Joey Huston, Zhao Li, Pavel M. Nadolsky, Jon Pumplin, and C.-P. Yuan. New
1666 parton distributions for collider physics. *Phys. Rev. D*, 82:074024, Oct 2010.
- 1667 [27] Summary of ATLAS Pythia 8 tunes. Technical Report ATL-PHYS-PUB-2012-003, CERN, Geneva, Aug 2012.
- 1668 [28] Jonathan Pumplin, Daniel Robert Stump, Joey Huston, Hung-Liang Lai, Pavel Nadolsky, and Wu-Ki Tung.
1669 New generation of parton distributions with uncertainties from global QCD analysis. *Journal of High Energy
1670 Physics*, 2002(07):012–012, jul 2002.
- 1671 [29] First tuning of HERWIG/JIMMY to ATLAS data. Technical Report ATL-PHYS-PUB-2010-014, CERN, Geneva,
1672 Oct 2010.
- 1673 [30] Aleksandra Dimitrijevska, Nenad Vranjes, Matthias Schott, and Maarten Boonekamp. Measurement of
1674 m_W at 7 TeV: Hadronic recoil corrections. Technical Report ATL-COM-PHYS-2015-344, CERN, Geneva, Apr
1675 2015.
- 1676 [31] Kendall, Maurice, and Alan Stuart. *The advanced theory of statistics*. London: Griffin, 1969.
- 1677 [32] Measurement of the $w \rightarrow \ell\nu$ and $z/y \rightarrow \ell\ell$ production cross sections in proton-proton collisions at $\sqrt{s} = 7\text{TeV}$ with the ATLAS detector. *Journal of High Energy Physics*, 2010(12), dec 2010.
- 1679 [33] ATLAS Collaboration. Electron performance measurements with the atlas detector using the 2010 lhc
1680 proton-proton collision data. *Eur. Phys. J. C72* (2012) 1909, 2011.
- 1681 [34] M. R. Whalley, D. Bourilkov, and R. C. Group. The les houches accord pdfs (lhapdf) and lhaglue, 2005.
- 1682 [35] Determination of the strange-quark density of the proton from ATLAS measurements of
1683 the $W \rightarrow \ell\nu$ and $Z \rightarrow \ell\ell$ cross sections. *Physical Review Letters*, 109(1), jul 2012.
- 1684 [36] S. Alekhin, J. Blümlein, S. Klein, and S. Moch. The 3-, 4-, and 5-flavor nnlo parton from deep-inelastic-
1685 scattering data and at hadron colliders. 2009.
- 1686 [37] Richard D. Ball, Valerio Bertone, Stefano Carrazza, Christopher S. Deans, Luigi Del Debbio, Stefano Forte,
1687 Alberto Guffanti, Nathan P. Hartland, Jose I. Latorre, Juan Rojo, and Maria Ubiali. Parton distributions with
1688 lhc data. 2012.
- 1689 [38] Bradley Dickinson. Estimation of partial correlation matrices using cholesky decomposition. In *1978 IEEE
1690 Conference on Decision and Control including the 17th Symposium on Adaptive Processes*. IEEE, jan 1978.
- 1691 [39] K. A. Olive et al. Review of Particle Physics. *Chin. Phys.*, C40:100001, 2016.

- 1692 [40] John M. Campbell and R.K. Ellis. MCFM for the Tevatron and the LHC. *Nucl.Phys.Proc.Suppl.*, 205-206:10–15,
1693 2010.
- 1694 [41] Tancredi Carli, Dan Clements, Amanda Cooper-Sarkar, Claire Gwenlan, Gavin P. Salam, Frank Siegert, Pavel
1695 Starovoitov, and Mark Sutton. A posteriori inclusion of parton density functions in nlo qcd final-state
1696 calculations at hadron colliders: The applgrid project. 2009.
- 1697 [42] S. Alekhin, J. Bluemlein, and S. Moch. The abm parton distributions tuned to lhc data. 2013.
- 1698 [43] Sayipjamal Dulat, Tie Jiun Hou, Jun Gao, Marco Guzzi, Joey Huston, Pavel Nadolsky, Jon Pumplin, Carl
1699 Schmidt, Daniel Stump, and C. P. Yuan. New parton distribution functions from a global analysis of
1700 quantum chromodynamics. 2015.
- 1701 [44] L. A. Harland-Lang, A. D. Martin, P. Motylinski, and R. S. Thorne. Parton distributions in the lhc era: Mmht
1702 2014 pdfs. 2014.